11. SITE 723[1]

Shipboard Scientific Party[2]

HOLE 723A

Date occupied: 15 September 1987

Date departed: 17 September 1987

Time on hole: 1 day, 16 hr, 30 min

Position: 18°03.079'N, 57°36.561'E

Water depth (sea level; corrected m, echo-sounding): 807.8

Water depth (rig floor; corrected m, echo-sounding): 818.3

Bottom felt (m, drill pipe): 816.2

Penetration (m): 432.3

Number of cores: 46

Total length of cored section (m): 432.3

Total core recovered (m): 298.2

Core recovery (%): 69

Oldest sediment cored:
Depth sub-bottom (m): 432.3
Nature: carbonate/limestone biscuits
Age: late Pliocene (NN18)
Measured velocity (km/s): 5.5

HOLE 723B

Date occupied: 17 September 1987

Date departed: 19 September 1987

Time on hole: 2 days, 10 hr, 45 min

Position: 18°03.079'N, 57°36.561'E

Water depth (sea level; corrected m, echo-sounding): 807.8

Water depth (rig floor; corrected m, echo-sounding): 818.3

Bottom felt (m, drill pipe): 816.7

Penetration (m): 429.0

Number of cores: 44

Total length of cored section (m): 400.1

Total core recovered (m): 295.4

Core recovery (%): 73.8

Oldest sediment cored:
Depth sub-bottom (m): 429.0
Nature: nannofossil clayey silt
Age: late Pliocene
Measured velocity (km/s): 1.7

HOLE 723C

Date occupied: 19 September 1987

Date departed: 19 September 1987

Time on hole: 8 hr, 45 min

Position: 18°03.079'N, 57°36.561'E

Water depth (sea level; corrected m, echo-sounding): 807.8

Water depth (rig floor; corrected m, echo-sounding): 818.3

Bottom felt (m, drill pipe): 815.8

Penetration (m): 76.8

Number of cores: 8

Total length of cored section (m): 76.8

Total core recovered (m): 82.17

Core recovery (%): 107

Oldest sediment cored:
Depth sub-bottom (m): 76.8
Nature: nannofossil clayey silt
Age: Pleistocene
Measured velocity (km/s): 1.6

Principal results: Site 723 corresponds to the central drilling target of a depth transect of sites across the Oman margin and is positioned in the center of the oxygen-minimum zone (OMZ).

Major findings at Site 723 include the identification of:

1. Laminated, opal-rich facies of late Pliocene and early Pleistocene age (the laminations indicate a lack of bioturbation);
2. Dolomite lenses within the hemipelagic sequence;
3. High accumulation rates (on average 175 m/m.y.) with detrital calcite as an important component;
4. High accumulation rates of marine organic carbon, especially in the upper Pliocene and lower Pleistocene;
5. Rapid and complete sulfate depletion by 50 mbsf, followed by an increase of interstitial sulfate from a subsurface source that fuels intense diagenetic reactions in the organic-rich sediments;
6. An increase in chloride near the base of the recovered section;
7. Abundant methane with traces of ethane and propane, which indicate thermogenic generation of hydrocarbons at depth;
8. Distinctive variations of magnetic susceptibility and physical properties which define specific periodicities that can be correlated to the Owen Ridge.

Overall, Site 723 provides a high-resolution sedimentary record of biotic, chemical, and sedimentologic variations associated with organic-rich sediments deposited under the influence of strong seasonal upwelling and generally low oxygen conditions.

BACKGROUND AND OBJECTIVES

Site 723 is located at 18°03.079'N and 57°36.561'E on the continental margin of Oman in water depths of 808 m. The position is near the center of the upper slope basin, where it shows the maximum sediment thickness. The location and depositional setting of Site 723 is shown in Figures 1 and 2; structural aspects of the site are shown in Figure 3.

At this location, the slope basin is about 15 km wide and is bounded on the west by a faulted block and on the east by a basement ridge. Both basement features are thought to be ophiolite complexes. The seismic reflection profiles of the basin sediments show numerous highly reflective layers that both onlap and drape the adjacent basement structures. The sediments are thickest in the center of the basin (>2000 m, based on sono-

[1] Prell, W. L., Niitsuma, N., et al., 1989. *Proc. ODP, Init. Repts.*, 117: College Station, TX (Ocean Drilling Program).

[2] Shipboard Scientific Party is as given in the list of Participants preceding the contents.

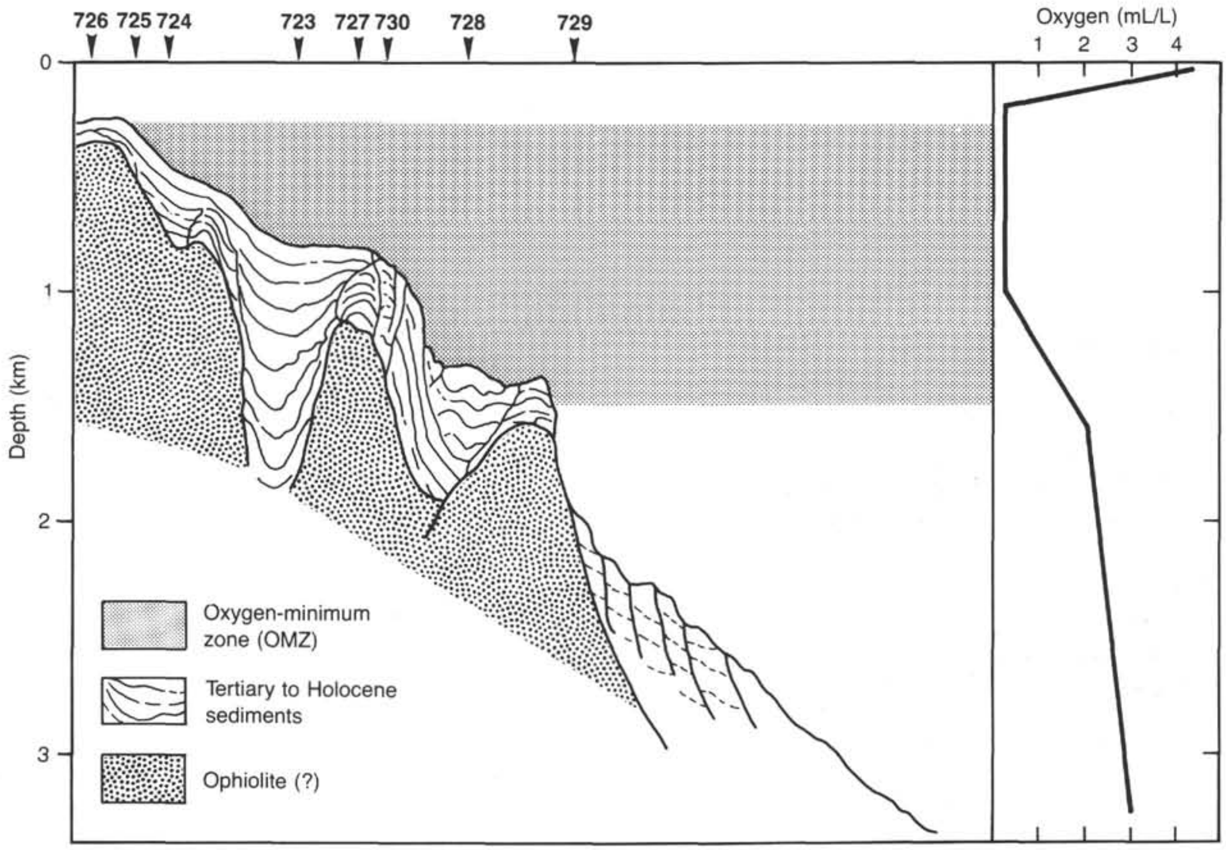

Figure 1. Structure of the Oman margin and the oxygen-minimum zone (OMZ). The schematic cross section of the margin shows the series of basement ophiolite blocks and the sedimentary basins between them. The concentration of oxygen in the water column (RC2704, unpublished data) defines the depth range of the OMZ and where it impinges on the margin.

buoy data; Mountain and Prell, this volume) and thus form a syncline-shaped deposit (Fig. 3). Along the strike of the basin, the surface and subsurface layers dip gently to the southwest and are relatively conformable, although some deformation and slump-related structures are observed (see "Seismic Stratigraphy" section, this chapter).

Site 723 was located within a zone of continuous reflectors (Fig. 3) that is bounded by two areas of irregular reflectors and diffuse seismic returns. The preliminary correlation of seismic reflectors within the basin indicates that the average accumulation rates increase from north to south and are highest near the location of Site 723. The site was selected to provide a high-resolution sedimentary record of the monsoonal upwelling during the Pliocene-Pleistocene.

Specific objectives for drilling at Site 723 were:

1. To obtain a high-resolution record of the sediments associated with the near-continent zone of the monsoonal upwelling system, in order to establish the changes in timing and intensity of the monsoon.
2. To examine the organic-rich sedimentary facies of the margin and establish their relationship to the oxygen-minimum zone (OMZ), and to document variations in the OMZ through time.
3. To document the diagenetic processes associated with the OMZ and the organic-rich sediments.
4. To search for evidence of changes in the structure of the intermediate-water masses of the Arabian Sea during the Pliocene-Pleistocene.

OPERATIONS

JOIDES Resolution departed Site 722 on 13 September 1987 en route for the island of Masirah (Oman) in order to pick up two Omani geologists who participated in the remainder of the leg. The rendezvous point was reached on 14 September at 0815 hours. By 0930 the helicopter had departed, and the ship set course for Site 723. On the approach to Site 723, the gear was streamed at 0700 on 15 September, and by 1145 the location of Site 723 had been chosen (Fig. 4). The first beacon was lowered on a taut wire in 808-m water depths. Erratic beacon signals necessitated deployment of two more beacons. The mud line of Hole 723A was shot at 1645 hours, and the final position of Site 723 was assessed as 18°03.079′N and 57°36.561′E by global positioning system (GPS).

Hole 723A was drilled to 85.1 mbsf using the advanced hydraulic piston corer (APC) mode (Cores 117-723A-1H to -9H) for an average recovery rate of 104%. Gas expansion and strong H_2S odors were noted throughout. An overpull of 80,000 lb during the retrieval of Core 117-723A-9H made the switch to extended core barrel (XCB) drilling necessary at this level. Coring was continued to Core 117-723A-46X (432.3 mbsf total depth [TD]). Recovery in the 347.2-m interval cored by XCB was 60%, so that the gross recovery of Hole 723A was 69%.

The rig was offset 10 m to the south on 16 September 1987, where the mud line of Hole 723B was cored at 0530 (Table 1). Nine APC cores were cored to a depth of 81.6 mbsf, for an average recovery rate of 104%, until a maximum overpull of 70,000 lb was reached. Drilling to 429.0 mbsf TD in the XCB mode re-

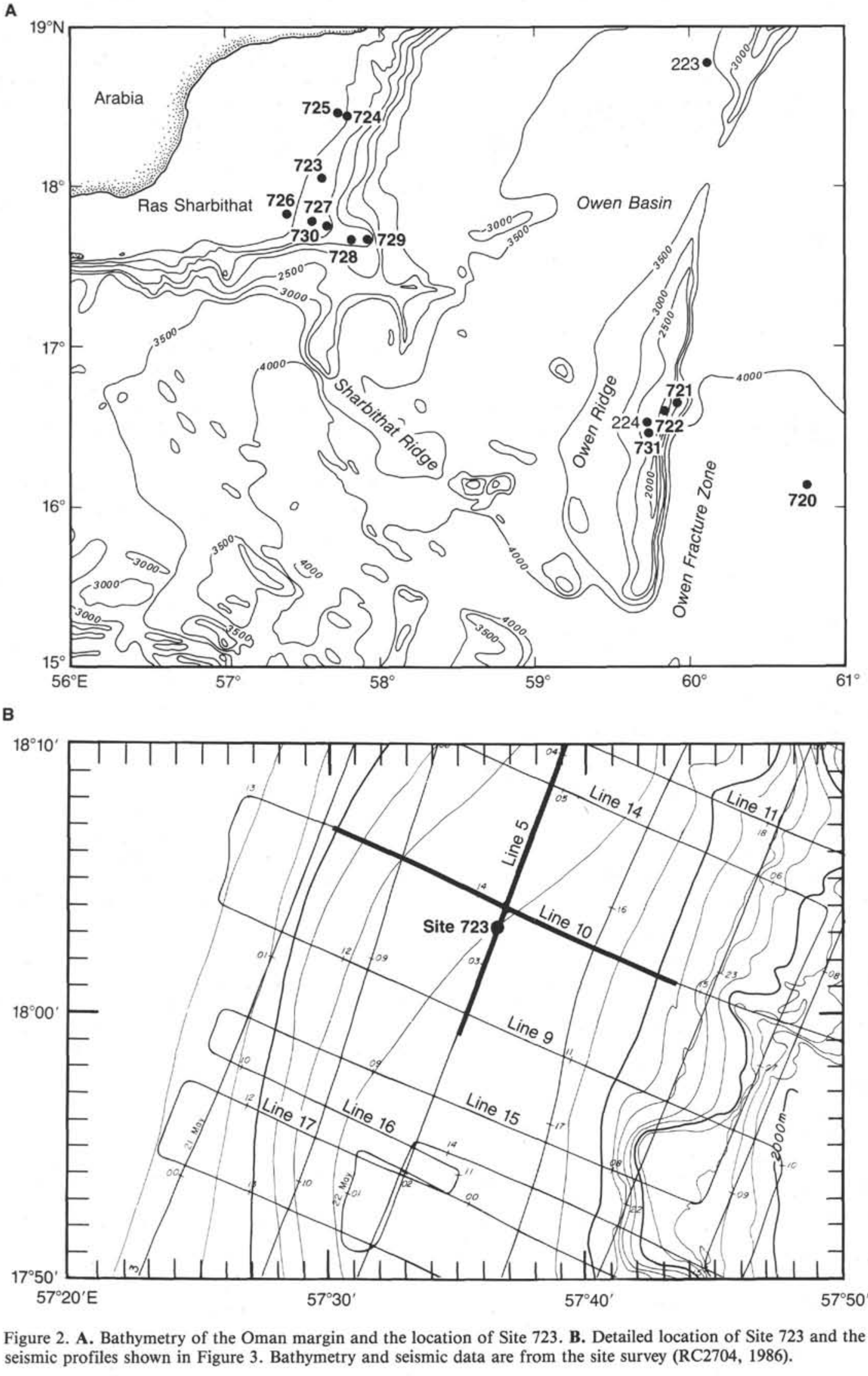

Figure 2. **A.** Bathymetry of the Oman margin and the location of Site 723. **B.** Detailed location of Site 723 and the seismic profiles shown in Figure 3. Bathymetry and seismic data are from the site survey (RC2704, 1986).

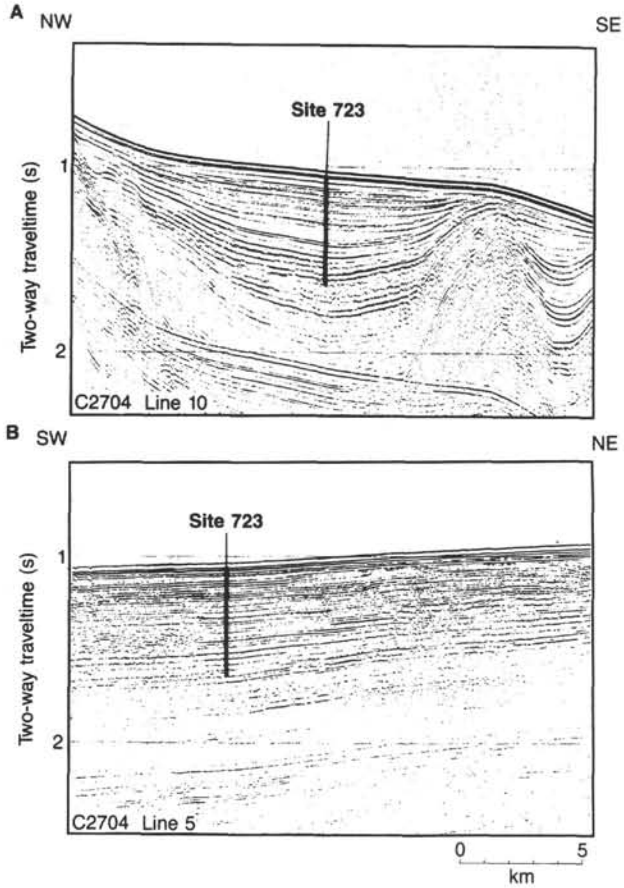

Figure 3. **A.** Single-channel seismic (SCS) reflection profiles showing the structural and depositional setting of Site 723. Line 10 is perpendicular to the trend of the basin and shows the bounding basement blocks and the synclinal-shaped sediment fill. **B.** Line 5 is along the strike of the basin and shows the sediment thickness decreasing to the northeast. Note the diffuse reflection patterns to either side of Site 723.

covered 66% of the cored section. We decided to drill ahead with a center bit in that part of the hole where dolomite stringers and nodules prevented recovery of any sediment (Core 117-723B-30X).

Average recovery for Hole 723B amounted to 73.8%, a value that is higher than the actual recovery of sediments because substantial gas expansion throughout the recovered cores resulted in abundant voids in the liners. Some core was lost through core expansion. Even though most of the gas pressure appeared to be due to high CO_2 pressure, the C_1:C_2 ratio in vacutainer gas samples had decreased to 800 in Core 117-723B-40X. The last sample taken from Core 117-723B-44X had a C_1:C_2 ratio of 1400. We terminated coring after we cut Core 117-723B-44X and noticed no improvement on recovery.

Prior to logging, the lockable flapper valve (LFV) was tested successfully with a dummy core barrel run on the sand line. After a wiper trip to total depth and sweeping with polymer, a go-devil was pumped down to lock the LFV open for the logging and the hole was displaced with polymer mud. The bottom-hole assembly (BHA) was positioned at 90 mbsf for the first logging run with the DIT/BHC/GR/CAL combination tool. The second string used LDT/CNL/NGT combinations, while string 3 employed GST/ACT tools. Except for slight hardware problems upon retrieval of the second run, all logs were of good quality and successfully completed. After completion, the BHA was pulled clear of Hole 723B by 1415 on 19 September 1987.

Hole 723C was spudded by 1430 hours without offsetting the ship, and eight APC cores were shot to a total depth of 76.8 mbsf. Upon retrieval of Core 117-723C-8H, constant overpull of 100,000 lb was needed. Shooting a ninth core, which was planned as the deepest core for the hole, was not attempted. The Pore-Water Sampling Tool (PWST) was deployed after Cores 117-723C-5H, -7H, and -8H. Cores of Hole 723C, a dedicated hole drilled to obtain geochemistry samples, were cut into 50-cm sections and frozen immediately.

The recovery rate for Hole 723C was 107%. The mud line was cleared, the taut-wire beacon was retrieved, and the ship was under way to Site 724 by 0030 on 20 September 1987.

LITHOSTRATIGRAPHY

Introduction

Site 723 is located in 808-m water depth near the center of the upper slope basin, at its maximum sediment thickness. The recovery in APC mode was almost perfect. However, severe gas expansion occurred below Cores 117-723A-4H and 117-723B-5H (about 35 mbsf). The top of Hole 723B obtained the mud line. In the sediments at Site 723, we recognized one sedimentary unit.

Unit I (Depth: 0.0–432.2 mbsf; Age: Holocene to late Pliocene)

Cores 117-723A-1H to -46X, 117-723B-1H to -44X, and 117-723C-1H to -8H.

Sediments recovered at Site 723 are described as a single lithologic unit based on their similarity of composition and primary sedimentary structures (Fig. 5). Three facies are identified. A marly nannofossil ooze with variable terrigenous content is dominant throughout the recovered section. Two minor facies occur intermittently below 240 mbsf in both holes: intervals of finely laminated siliceous and marly ooze, and dolomitic limestone, which in some cases displays fine laminae. The occurrence of these facies is summarized in Table 2; the facies are described below.

Facies I

Facies I consists of foraminifer-bearing marly nannofossil ooze and calcareous clayey silt, mottled olive gray (5Y 4/2, 5Y 4/3) grading to dark olive gray (5Y 3/1, 5Y 2.5/1) below 230 mbsf. Variations in the abundance of foraminifers and silt-sized calcite in smear slides explain most of the variation observed in this facies. Foraminifers are common on the split core face throughout. Shell fragments are most common in the upper half of the hole. Biogenic carbonate content varies between 30% and 50% on smear slides. The terrigenous component varies between 30% and 80%, but it is not specifically related to minor color changes observed at all scales. It is dominated by clay and silt-size detrital calcite. Euhedral dolomite rhombs are observed in trace amounts at all depths.

Facies II

Dolomitic limestone in thin cemented layers contains many components found in Facies I and III. Thin sections from Cores 117-723A-28X and -37X and Cores 117-723B-27X and -23X contain spar cement, clay, abundant foraminifers, traces of organic material, quartz, and siliceous skeletal debris. The thin section from Core 117-723A-45X, a cemented laminated interval, contains alternating layers of diatomaceous skeletal structure and darker clay-rich layers.

The diffraction pattern of a sample from Core 117-723A-45X indicates almost pure dolomite based on the d-spacing of the (211) reflection (see "Inorganic Geochemistry" section, this chapter). Depths where these layers occur are shown in Figure 5.

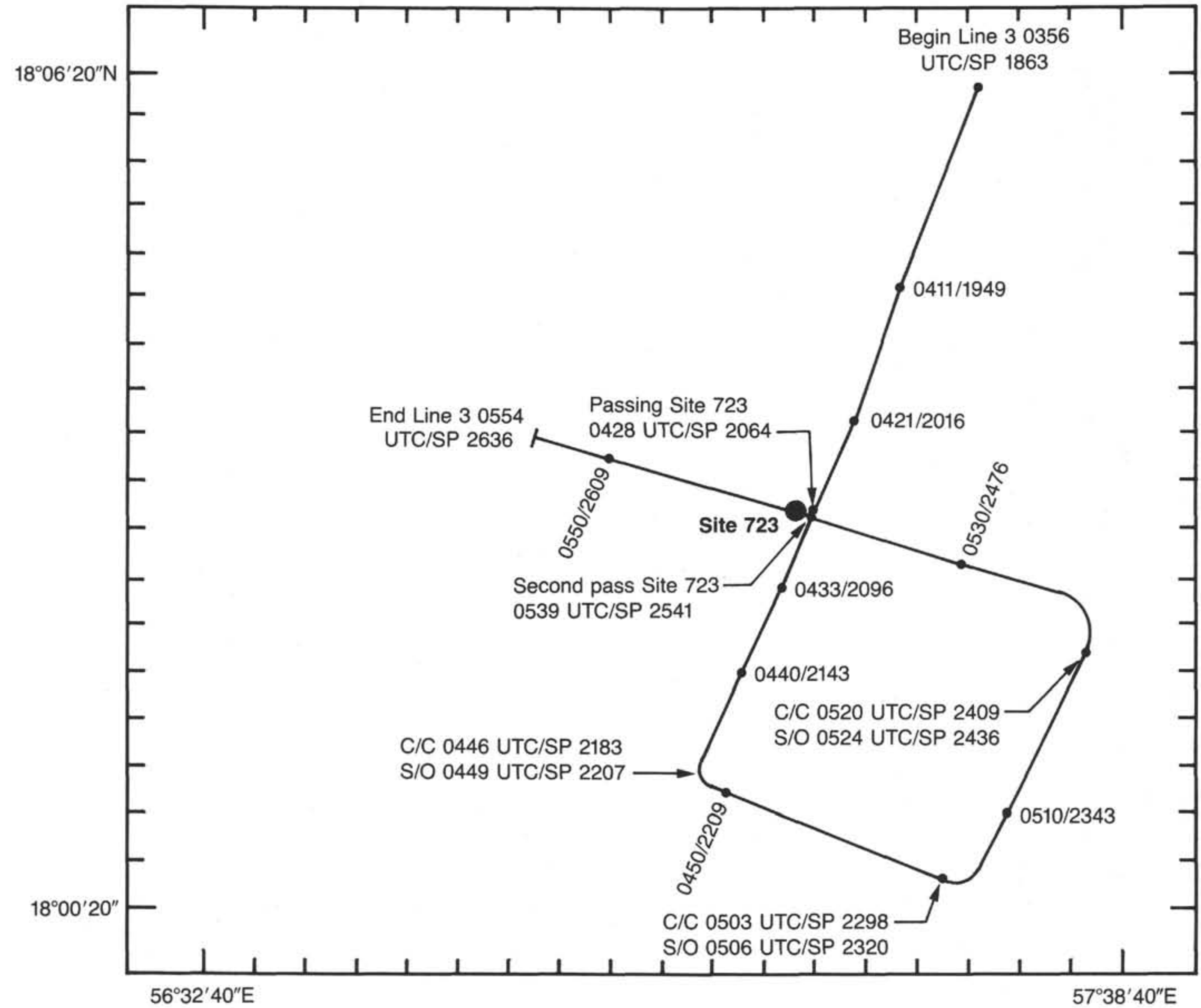

Figure 4. Track of *JOIDES Resolution* on approach to Site 723.

Seven different layers are identified in Hole 723A or 723B, at 245, 262, 318, 336, 377, 403 and 420 mbsf (Table 2). Log data indicate the presence of nine layers (see "Downhole Measurements" section, this chapter), six of which correlate with the recovered intervals. Recovered thickness varies between 5 and 30 cm, and log data suggests a maximum thickness of 1 m for each interval.

Facies III

Light and dark laminae 0.1–1.0 mm thick (Fig. 6) comprise Facies III. Light layers are diatom ooze or diatomite often dominated by a single species. Radiolarians, silicoflagellates, and sponge spicules are present in trace amounts. Light laminae also contain variable amounts of detrital calcite and nannofossils. The dark laminae are composed of marly nannofossil ooze, similar in composition to Facies I, but they often contain traces of organic material which occurs as pellets or clay aggregates.

Laminated intervals are usually less than 10 cm thick, observed in hard drilling biscuits and indistinct in softer sediment. The upper and lower contacts are gradational with Facies I (marly ooze), and individual laminae are often indistinct and variable in thickness within laminated intervals. The longest continuously laminated interval observed is approximately 2 m thick. Although one interval is found in the lower Pleistocene (Core 117-723B-18X; 162 mbsf), the greatest frequency of laminated intervals occurs between 300 and 350 mbsf in the upper Pliocene (Table 2).

Disturbance

Gas expansion began to affect core recovery below 35 mbsf. Initially, the sediment separated into flakes and very small spaces (< 1 cm) which are not evaluated as void space in core descriptions but which do reduce the sediment density measured by GRAPE, magnetic susceptibility, and other whole-core sampling tools. This expansion gradually became localized in larger voids, probably related to increased cohesiveness of the sediment and to a change in core handling. When the voids became noticeable, the gas was released by puncturing the core liner.

Between 35 and 100 mbsf disturbance becomes more pronounced, as observed in physical properties data and in the core descriptions. In the upper cores the sediment appears continuous across these voids; deeper in the holes this stratigraphic con-

Table 1. Coring summary, Site 723.

Core no.	Date (Sept. 1987)	Time (local)	Depth (mbsf)	Cored (m)	Recovered (m)	Recovery (%)
117-723A-						
1H	15	1720	0-7.8	7.8	7.88	101.0
2H	15	1745	7.8-17.5	9.7	9.87	102.0
3H	15	1805	17.5-27.1	9.6	9.86	103.0
4H	15	1825	27.1-36.8	9.7	9.90	102.0
5H	15	1840	36.8-46.4	9.6	9.82	102.0
6H	15	1920	46.4-56.1	9.7	10.20	105.1
7H	15	1940	56.1-65.8	9.7	10.54	108.6
8H	15	2020	65.8-75.4	9.6	10.12	105.4
9H	15	2020	75.4-85.1	9.7	10.11	104.2
10X	15	2130	85.1-94.8	9.7	0	0
11X	15	2230	94.8-104.4	9.6	2.63	27.4
12X	15	2300	104.4-114.1	9.7	0	0
13X	15	2345	114.1-123.8	9.7	6.96	71.7
14X	16	0040	123.8-133.4	9.6	6.83	71.1
15X	16	0125	133.4-143.1	9.7	9.78	101.0
16X	16	0215	143.1-152.8	9.7	0	0
17X	16	0250	152.8-162.4	9.6	3.55	37.0
18X	16	0325	162.4-172.1	9.7	0	0
19X	16	0355	172.1-181.8	9.7	10.50	108.2
20X	16	0425	181.8-191.4	9.6	9.71	101.0
21X	16	0450	191.4-201.1	9.7	9.74	100.0
22X	16	0525	201.1-210.8	9.7	10.08	103.9
23X	16	0555	210.8-220.4	9.6	3.63	37.8
24X	16	0635	220.4-230.1	9.7	10.12	104.3
25X	16	0710	230.1-239.8	9.7	9.57	98.6
26X	16	0755	239.8-249.4	9.6	6.53	68.0
27X	16	0835	249.4-259.1	9.7	8.54	88.0
28X	16	0925	259.1-268.7	9.6	3.84	40.0
29X	16	1000	268.7-278.3	9.6	10.07	104.9
30X	16	1055	278.3-287.9	9.6	7.61	79.3
31X	16	1135	287.9-297.5	9.6	10.18	106.0
32X	16	1215	297.5-307.1	9.6	9.83	102.0
33X	16	1250	307.1-316.7	9.6	10.10	105.2
34X	16	1330	316.7-321.5	4.8	0.48	10.0
35X	16	1355	321.5-326.3	4.8	5.93	123.0
36X	16	1430	326.3-335.8	9.5	11.28	118.7
37X	16	1535	335.8-345.4	9.6	1.57	16.3
38X	16	1610	345.4-355.0	9.6	0	0
39X	16	1655	355.0-364.7	9.7	9.58	98.7
40X	16	1730	364.7-374.3	9.6	9.86	103.0
41X	16	1830	374.3-384.0	9.7	9.15	94.3
42X	16	1930	384.0-393.6	9.6	1.94	20.2
43X	16	2035	393.6-403.3	9.7	0	0
44X	16	2135	403.3-413.0	9.7	0.05	0.5
45X	16	2250	413.0-422.6	9.6	0.28	2.9
46X	16	2345	422.6-432.3	9.7	0	0
				432.3	298.22	
117-723B-						
1H	17	0605	0-4.3	4.3	4.29	99.7
2H	17	0630	4.3-14.0	9.7	9.93	102.0
3H	17	0650	14.0-23.6	9.6	9.97	104.0
4H	17	0715	23.6-33.3	9.7	9.83	101.0
5H	17	0735	33.3-42.9	9.6	10.00	104.1
6H	17	0805	42.9-52.6	9.7	10.36	106.8
7H	17	0840	52.6-62.3	9.7	10.45	107.7
8H	17	0910	62.3-71.9	9.6	10.25	106.8
9H	17	0940	71.9-81.6	9.7	10.21	105.2
10X	17	1055	81.6-91.2	9.6	9.53	99.3
11X	17	1115	91.2-100.7	9.5	9.87	104.0
12X	17	1205	100.7-110.3	9.6	8.83	92.0
13X	17	1245	110.3-119.9	9.6	8.45	88.0
14X	17	1315	119.9-129.6	9.7	9.39	96.8
15X	17	1350	129.6-139.2	9.6	9.29	96.8
16X	17	1420	139.2-148.9	9.7	4.74	48.8
17X	17	1445	148.9-158.6	9.7	9.65	99.5
18X	17	1510	158.6-168.2	9.6	9.72	101.0
19X	17	1540	168.2-177.9	9.7	10.37	106.9
20X	17	1600	177.9-187.6	9.7	10.13	104.4
21X	17	1625	187.6-197.3	9.7	10.03	103.4
22X	17	1650	197.3-206.9	9.6	9.43	98.2
23X	17	1715	206.9-216.5	9.6	9.89	103.0
24X	17	1800	216.5-226.2	9.7	10.59	109.2
25X	17	1830	226.2-235.9	9.7	10.13	104.4

Table 1 (continued).

Core no.	Date (Sept. 1987)	Time (local)	Depth (mbsf)	Cored (m)	Recovered (m)	Recovery (%)
117-723B-						
26X	17	1900	235.9-245.6	9.7	9.39	96.8
27X	17	2000	245.6-247.2	1.6	1.88	117.5
28X	17	2040	247.2-255.0	7.8	0	0
29X	17	2155	255.0-264.7	9.7	0	0
30X	17	2230	264.7-274.4	9.7	0	0
31X	18	0045	293.7-303.3	9.6	9.54	99.4
32X	18	0155	303.3-313.0	9.7	0	0
33X	18	0300	313.0-317.4	4.4	4.17	94.8
34X	18	0345	317.4-322.7	5.3	0	0
35X	18	0430	322.7-332.5	9.8	3.33	34.0
36X	18	0545	332.5-342.2	9.7	1.59	16.4
37X	18	0625	342.2-351.9	9.7	0	0
38X	18	0710	351.9-361.6	9.7	3.31	34.1
39X	18	0755	361.6-371.3	9.7	9.60	98.9
40X	18	0900	371.3-381.0	9.7	5.57	57.4
41X	18	0950	381.0-390.7	9.7	6.71	69.2
42X	18	1140	400.3-409.8	9.5	5.01	52.7
43X	18	1235	409.8-419.4	9.6	0	0
44X	18	1400	419.4-429.0	9.6	0.22	2.3
				400.1	295.65	
117-723C-						
1H	19	1600	0-9.2	9.2	9.20	100.0
2H	19	1615	9.2-18.9	9.7	10.01	103.2
3H	19	1630	18.9-28.5	9.6	9.79	102.0
4H	19	1645	28.5-38.2	9.7	10.00	103.1
5H	19	1700	38.2-47.8	9.6	10.13	105.5
6H	19	1800	47.8-57.5	9.7	10.32	106.4
7H	19	1825	57.5-67.2	9.7	11.62	119.8
8H	19	2015	67.2-76.8	9.6	11.10	115.6
				76.8	82.17	

tinuity is difficult to assess. Voids where soupy sediment or structure suggests missing sediment are noted on the barrel sheets. Lithologic observations thus suggest that except where noted, sediment is continuous within each core. Therefore, where recovery is less than 100%, sediment is missing from the top or bottom of each core (Table 3). Recovery above 250 mbsf averaged 70% in Hole 723A and 85% in Hole 723B; this dropped to 45% and 31% below 250 mbsf (Table 1).

Discussion

The dominance of Facies I throughout the recovered interval suggests that a similar depositional environment has dominated the Pleistocene and late Pliocene. The absence of turbidites, erosional contacts, and massive gravity-flow structures suggests a relatively undisturbed sediment deposition, with varying terrigenous and biogenic sediment components. In contrast to Sites 725 and 726 closer to the shelf break (see "Site 725" and "Site 726" chapters, this volume), little sand-sized terrigenous material was transported to Site 723.

In smear slides nannofossils dominate the biogenic component even though foraminifers are abundant in sieved samples. Siliceous microfossils are present in the surface sample and in the downhole laminated intervals, but are rare in the remainder of the cored sections. The absence of opal below the surface sediment suggests that it is produced in the modern environment, but that the opal dissolves rapidly and is not preserved.

Sediments contain abundant silt-sized detrital calcite, presumably derived from the adjacent carbonate deserts. The flux of terrigenous sediment, primarily of clay and silt size, is greater than at sites on the Owen Ridge. Compared with Owen Ridge Sites 721 and 722, sedimentation rates are three to four times higher. The carbonate content is lower, which indicates dilution

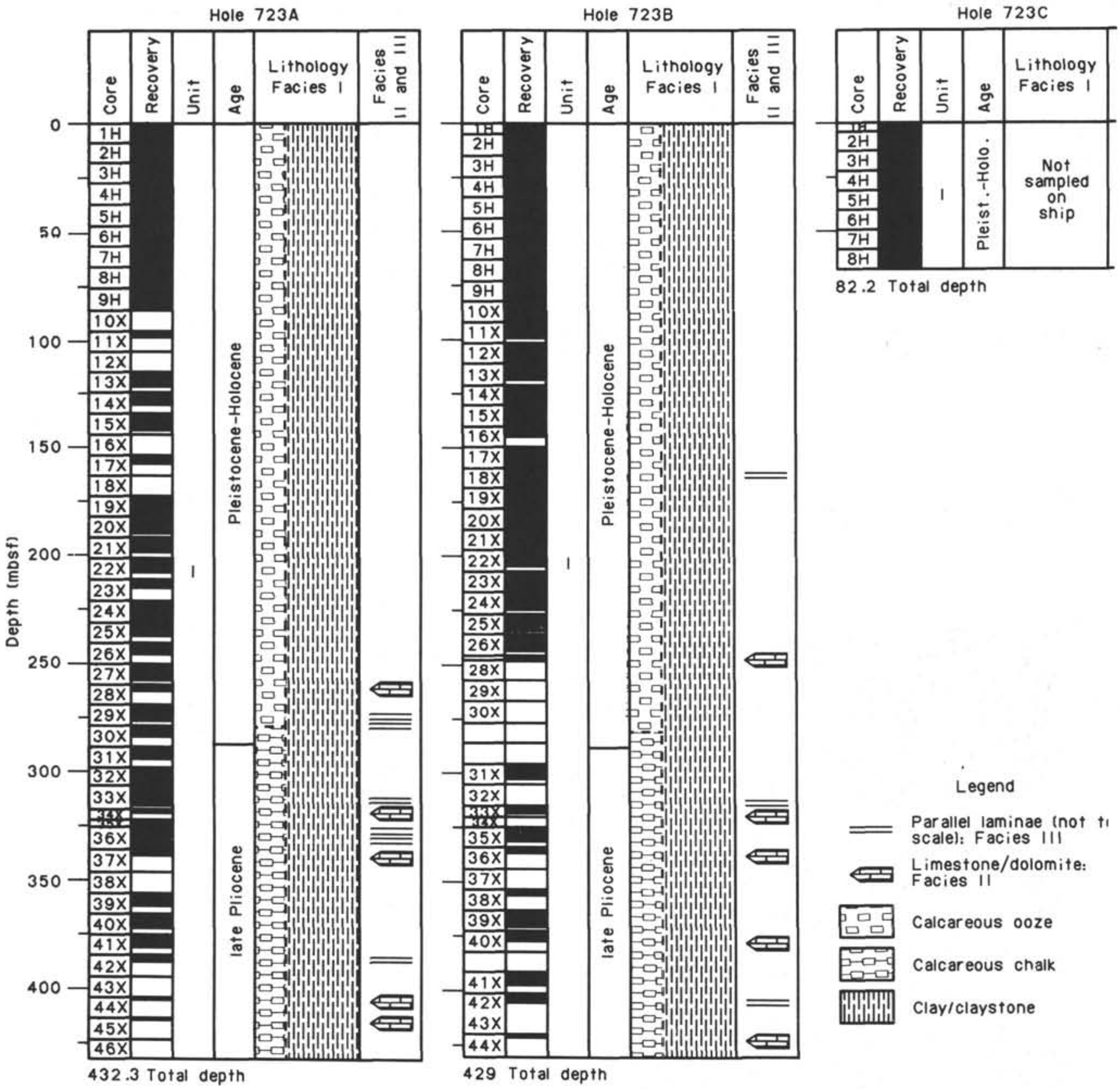

Figure 5. Lithologic summary, Site 723.

by the terrigenous components. The variations in sediment composition on the margin reflect changes in the relative flux of terrigenous and biogenic components. Variable fluxes produce a facies which varies between a marly ooze with 30%–60% carbonate, and infrequent intervals where the carbonate content is <30%.

Variations in biogenic carbonate flux will be difficult to evaluate by analyses which combust both detrital and biogenic calcite; some means of identifying the terrigenous fraction of the carbonate must be employed. These two sources of carbonate partially explain the differences in carbonate stratigraphies between Site 723 and Sites 721 and 722 on the Owen Ridge. Figure 7 shows the carbonate and organic carbon record for Hole 723A sampled at 75-cm intervals (see also Table 4). These data show cyclicity at several scales, but the average value does not change significantly downhole (mean = 56.1% $CaCO_3$, SD = 8.04%, min = 29.4%, max = 71.6%).

The episodic, rather than the continuous, occurrence of laminated intervals suggests that in the late Pliocene through early Pleistocene conditions existed for short intervals of time which allowed the formation and preservation of laminated sediments. If the light layers represent annual upwelling seasons, then these conditions most often existed for tens to hundreds of years at a time. Typical sedimentation rates during intervals in Core 117-723B-32X are 80 and 130 cm/k.y. (assuming annual varves). Within the intervals the laminae are variable in thickness and lateral extent and the contact with Facies I is gradational. Conditions necessary for varve formation and preservation appear transient.

Facies II (dolomite layers) and Facies III are found adjacent, and in some cases the dolomite layers are laminated. Dolomite stringers were also found on Leg 112 in the organic-rich sediments of the Peru upwelling system (Suess, von Huene, et al., 1988). Organic-rich sediment is one prerequisite for the forma-

Table 2. Occurrence of dolomitic limestone (Facies II) and laminated intervals (Facies III).

Facies	Hole 723A core	Hole 723B core	Depth (mbsf)	Age
Facies II:				
Dolomitic		27	245	early Pleistocene
limestone	29		262	early Pleistocene
	34	33	318	late Pliocene
	37	36	336	late Pliocene
		40	377	late Pliocene
	44		403	late Pliocene
	45	44	420	late Pliocene
Facies III:				
Laminated		18	162	Pleistocene
diatomaceous ooze	29		273	early Pleistocene
and marly nanno-	30		278	early Pleistocene
fossil ooze	33		312	late Pliocene
		33	315	late Pliocene
	35		323	late Pliocene
	36		330	late Pliocene
	37	36	338	late Pliocene
	42		386	late Pliocene
	44	42	405	late Pliocene
		44	420	late Pliocene

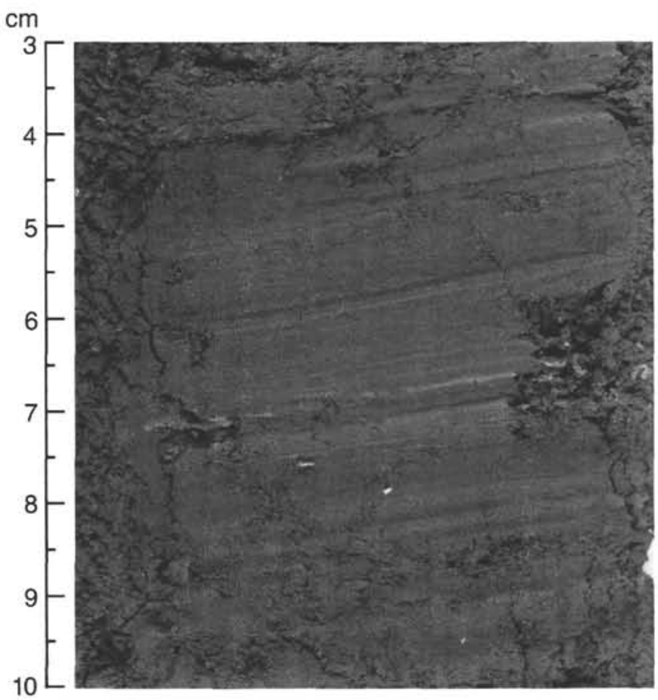

Figure 6. Laminated diatomite and marly nannofossil ooze (117-723A-29X-7, 3-10 cm).

tion of these layers, and their presence in the upper Pliocene and lower Pleistocene and absence in the upper Pleistocene is consistent with higher contents of organic material in this interval, which coincides approximately with the time when laminae were formed. The youngest dolomite is formed approximately 20 m above the limit of the intensely laminated zone.

Another necessary condition for the formation and preservation of laminae is the absence of bioturbation at the seafloor. On the face of split cores we see a decrease in burrow mottling and benthic shell fragments deeper in the section. A third indi-

Table 3. Site 723 core recovery adjusted for voids within sections.

Core no.	Length (m)	Recovered (m)	Percent (%)
117-723A-			
1H	7.8	7.81	100.1
2H	9.7	9.81	101.1
3H	9.6	9.81	102.2
4H	9.7	9.83	101.3
5H	9.6	9.83	102.0
6H	9.7	9.63	99.3
7H	9.7	11.02	113.6
8H	9.6	10.05	104.7
9H	9.7	9.95	102.6
10X	9.7	0	0
11X	9.6	2.60	27.1
12X	9.7	0	0
13X	9.7	6.18	63.7
14X	9.6	5.61	58.4
15X	9.7	7.66	79.0
16X	9.7	0	0
17X	9.6	3.32	34.6
18X	9.7	0	0
19X	9.7	9.21	94.9
20X	9.6	7.37	76.8
21X	9.7	6.13	63.2
22X	9.7	7.69	79.3
23X	9.6	2.74	28.5
24X	9.7	8.71	89.8
25X	9.7	5.07	52.3
26X	9.6	4.55	47.4
27X	9.7	6.93	71.4
28X	9.6	2.65	27.6
29X	9.6	7.79	81.1
30X	9.6	4.62	92.5
31X	9.6	6.5	67.7
32X	9.6	9.15	95.3
33X	9.6	8.17	85.1
34X	4.8	0.47	9.8
35X	4.8	4.44	92.5
36X	9.5	9.43	99.3
37X	9.6	1.58	16.5
38X	9.6	0	0
39X	9.7	6.13	63.2
40X	9.6	6.58	68.5
41X	9.7	5.82	60.0
42X	9.6	1.62	16.9
43X	9.7	0	0
44X	9.7	0.03	0.3
45X	9.6	0.28	2.9
46X	9.7	0	0
117-723B-			
1H	4.3	4.29	99.7
2H	9.7	9.93	102.0
3H	9.6	9.97	104.0
4H	9.7	9.83	101.0
5H	9.6	10.00	104.1
6H	9.7	10.36	106.8
7H	9.7	10.32	106.4
8H	9.6	9.72	101.3
9H	9.7	9.40	96.9
10X	9.6	7.89	82.2
11X	9.5	7.73	81.4
12X	9.6	8.73	90.9
13X	9.6	6.83	71.1
14X	9.7	8.24	84.9
15X	9.6	8.75	91.1
16X	9.7	4.05	41.8
17X	9.7	8.85	91.2
18X	9.6	8.61	89.7
19X	9.7	9.43	97.2
20X	9.7	8.15	84.0
21X	9.7	8.07	83.2
22X	9.6	7.25	75.5
23X	9.6	8.01	83.4
24X	9.7	8.55	88.1
25X	9.7	7.73	79.7
26X	9.7	7.61	78.5

Table 3 (continued).

Core no.	Length (m)	Recovered (m)	Percent (%)
117-723B-			
27X	1.6	1.68	105.0
28X	7.8	0	0
29X	9.7	0	0
30X	9.7	0	0
31X	9.6	6.91	72.0
32X	9.7	0	0
33X	4.4	3.45	78.4
34X	5.3	0	0
35X	9.8	2.61	26.7
36X	9.7	1.48	15.3
37X	9.7	0	0
38X	9.7	2.18	22.5
39X	9.7	7.10	73.2
40X	9.7	3.47	35.8
41X	9.7	5.33	54.9
42X	9.5	3.43	36.1
43X	9.6	0	0
44X	9.6	0.22	2.3

Note: This table was produced by subtracting all voids > 1 cm from the original recovered length noted in the core recovery log.

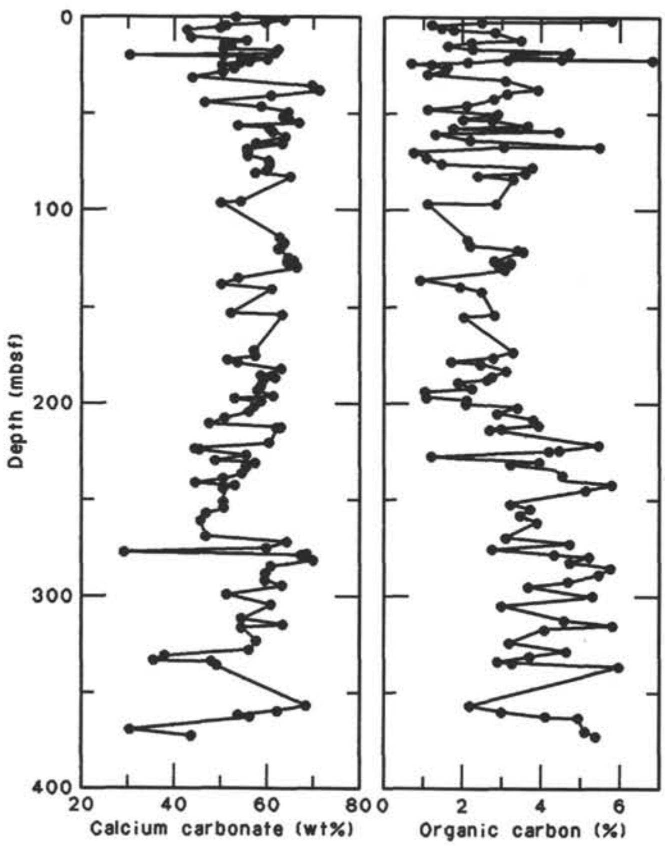

Figure 7. Downhole plot of calcium carbonate and organic carbon.

cator of decreased benthic activity may be the observed increase in organic carbon. Sediment accumulated faster than organic matter could be remineralized by benthic organisms. Cores below 230 mbsf (Core 117-723A-25X) are darker (dark olive gray 5Y 3/1, 5Y 2.5/1) than those above (olive 5Y 4/3, 5Y 4/2). This general change is also observed in the mean organic carbon content (Fig. 7 and Table 4). Lithologic observations thus suggest

Table 4. Calcium carbonate and organic carbon data for Hole 723A.

Core, section, interval (cm)	Depth (mbsf)	Total carbon (%)	Inorganic carbon (%)	Organic carbon (%)	$CaCO_3$ (wt%)
117-723A-					
1H-1, 43–44	0.43	12.25	6.45	5.80	53.7
1H-1, 113–114	1.13		7.22		60.1
1H-2, 43–44	1.93	10.18	7.67	2.51	63.9
1H-2, 110–114	2.60		7.52		62.6
1H-3, 43–44	3.43	8.42	7.17	1.25	59.7
1H-3, 113–114	4.13		6.64		55.3
1H-4, 43–44	4.93	7.68	6.19	1.49	51.6
1H-4, 110–114	5.60		6.14		51.2
1H-4, 144–145	5.94	7.82	6.02	1.80	50.2
1H-5, 113–114	7.13	8.03	5.17	2.86	43.1
2H-1, 113–114	8.93		6.89		57.4
2H-2, 113–114	10.43		5.20		43.3
2H-3, 43–44	11.23	8.84	5.28	3.56	44.0
2H-3, 113–114	11.93		6.51		54.2
2H-4, 43–44	12.73	8.95	6.70	2.25	55.8
2H-4, 113–114	13.43		6.37		53.1
2H-5, 43–44	14.23	7.82	6.14	1.68	51.2
2H-5, 113–114	14.93		5.85		48.7
2H-6, 43–44	15.73	8.59	6.32	2.27	52.7
2H-6, 113–114	16.43		7.30		60.8
2H-7, 43–44	17.23	10.91	6.14	4.77	51.2
3H-1, 43–44	17.93	11.12	7.53	3.59	62.7
3H-1, 113–114	18.63		7.46		62.1
3H-2, 43–44	19.43	10.84	7.46	3.38	62.1
3H-2, 113–114	20.13		6.48		54.0
3H-2, 127–128	20.27	10.70	6.12	4.58	51.0
3H-2, 138–139	20.38	10.52	3.69	6.83	30.7
3H-3, 43–44	20.93	9.76	6.56	3.20	54.6
3H-3, 113–114	21.63		8.31		69.2
3H-4, 43–44	22.43	9.41	7.23	2.18	60.2
3H-4, 113–114	23.13		6.79		56.6
3H-4, 144–145	23.44	7.48	6.77	0.71	56.4
3H-5, 43–44	23.93	7.81	6.58	1.23	54.8
3H-5, 113–114	24.63		5.88		49.0
3H-6, 43–44	25.43	7.76	6.10	1.66	50.8
3H-6, 113–114	26.13		5.53		46.1
3H-7, 43–44	26.93	8.01	6.41	1.60	53.4
4H-1, 43–44	27.53		6.51		54.2
4H-2, 43–44	29.03	7.23	6.11	1.12	50.9
4H-3, 43–44	30.53		6.04		50.3
4H-4, 43–44	32.03	8.49	5.33	3.16	44.4
4H-5, 43–44	33.53		6.42		53.5
4H-6, 43–44	35.03		4.57		38.1
4H-7, 43–44	36.53	12.40	8.42	3.98	70.1
5H-1, 33–34	37.13		7.24		60.3
5H-2, 43–44	38.73	11.78	8.59	3.19	71.6
5H-3, 43–44	40.23		7.10		59.1
5H-4, 43–44	41.73	10.18	7.33	2.85	61.1
5H-5, 46–47	43.26		6.68		55.6
5H-6, 43–44	44.73	7.78	5.62	2.16	46.8
5H-7, 43–44	46.23		6.34		52.8
6H-1, 43–44	46.83	8.17	7.05	1.12	58.7
6H-2, 43–44	48.33		6.99		58.2
6H-3, 43–44	49.83	10.76	7.81	2.95	65.1
6H-4, 43–44	51.33		7.77		64.7
6H-4, 144–145	52.34	9.71	7.67	2.04	63.9
6H-5, 43–44	52.83	10.58	7.79	2.79	64.9
6H-6, 43–44	54.33		7.42		61.8
6H-7, 43–44	55.83	11.80	8.08	3.72	67.3
7H-1, 38–39	56.48		7.53		62.7
7H-2, 43–44	56.94	8.30	6.48	1.82	54.0
7H-2, 149–150	58.00	11.76	7.26	4.50	60.5
7H-4, 43–44	59.94	8.69	7.37	1.32	61.4
7H-5, 43–44	61.44		7.60		63.3
7H-6, 43–44	62.94	9.94	7.72	2.22	64.3
7H-7, 43–44	64.44		7.73		64.4
7H-8, 43–44	65.94	12.46	6.95	5.51	57.9
7H, CC, 16–17	66.58		8.07		67.2
8H-1, 43–44	66.23	10.77	7.65	3.12	63.7
8H-2, 43–44	67.73		7.57		63.1
8H-3, 43–44	69.23	7.47	6.71	0.76	55.9
8H-4, 43–44	70.73		6.94		57.8
8H-4, 149–150	71.79	7.84	6.75	1.09	56.2
8H-5, 43–44	72.23	7.80	6.73	1.07	56.1
8H-6, 43–44	73.73		6.66		55.5
8H-7, 43–44	75.23	8.75	7.27	1.48	60.6

Table 4 (continued).

Core, section, interval (cm)	Depth (mbsf)	Total carbon (%)	Inorganic carbon (%)	Organic carbon (%)	$CaCO_3$ (wt%)
117-723A-					
9H-1, 46–47	75.86		7.19		59.9
9H-2, 43–44	77.33	11.14	7.29	3.85	60.7
9H-3, 43–44	78.83		7.29		60.7
9H-4, 43–44	80.33	10.91	7.23	3.68	60.2
9H-4, 144–145	81.34	9.36	6.94	2.42	57.8
9H-5, 39–40	81.79		7.18		59.8
9H-6, 43–44	83.33	11.23	7.86	3.37	65.5
9H-7, 43–44	84.83		7.22		60.1
11X-1, 107–108	95.87	9.46	6.55	2.91	54.6
11X-1, 149–150	96.29	7.14	6.05	1.09	50.4
11X-2, 46–47	96.76		5.31		44.2
13X-1, 43–44	114.53	9.75	7.56	2.19	63.0
13X-2, 43–44	116.03		7.48		62.3
13X-3, 43–44	117.53	9.94	7.70	2.24	64.1
13X-4, 46–47	119.06		7.45		62.1
13X-4, 119–120	119.79	11.09	7.60	3.49	63.3
13X-5, 43–44	120.53	11.14	7.53	3.61	62.7
14X-1, 43–44	124.23		8.02		66.8
14X-2, 43–44	125.73	10.72	7.84	2.88	65.3
14X-2, 149–150	126.79	11.25	7.97	3.28	66.4
14X-3, 70–71	127.50	10.76	7.79	2.97	64.9
14X-4, 43–44	128.73		7.54		62.8
14X-5, 20–21	130.00	11.14	8.01	3.13	66.7
15X-1, 40–41	133.80		6.52		54.3
15X-2, 43–44	135.33	7.41	6.49	0.92	54.1
15X-3, 70–71	137.10		6.39		53.2
15X-4, 43–44	138.33	7.99	6.04	1.95	50.3
15X-5, 70–71	140.10		7.06		58.8
15X-6, 0–1	140.90	9.85	7.34	2.51	61.1
15X-7, 20–21	142.60		7.05		58.7
17X-1, 43–44	153.23	9.16	6.30	2.86	52.5
17X-2, 0–1	154.30	9.68	7.62	2.06	63.5
17X-2, 43–44	154.73		7.52		62.6
19X-1, 42–43	172.52	10.22	6.87	3.35	57.2
19X-2, 30–31	173.90		6.78		56.5
19X-3, 42–43	175.52	9.72	6.92	2.80	57.6
19X-4, 42–43	177.02		6.49		54.1
19X-4, 64–65	177.24	7.97	6.21	1.76	51.7
19X-5, 42–43	178.52	8.94	6.47	2.47	53.9
19X-6, 30–31	179.90		6.47		53.9
19X-7, 42–43	181.52		6.85		57.1
20X-1, 40–41	182.20	10.77	7.60	3.17	63.3
20X-2, 40–41	183.70		7.20		60.0
20X-3, 40–41	185.20	9.82	7.04	2.78	58.6
20X-4, 30–31	186.60	10.08	7.43	2.65	61.9
20X-4, 40–41	186.70		7.45		62.1
20X-5, 40–41	188.20	9.05	7.12	1.93	59.3
20X-6, 50–51	189.80		6.68		55.6
20X-7, 40–41	191.20	9.32	7.06	2.26	58.8
21X-1, 27–28	191.67		6.72		56.0
21X-2, 27–28	193.17	8.02	6.98	1.04	58.1
21X-3, 27–28	194.67		7.04		58.6
21X-4, 33–34	196.23	8.46	7.37	1.09	61.4
21X-5, 0–1	197.40	8.50	6.38	2.12	53.2
21X-5, 27–28	197.67		6.34		52.8
21X-6, 45–46	199.35	9.17	7.06	2.11	58.8
21X, CC, 27–28	200.77		6.78		56.5
22X-1, 29–30	201.39	10.36	6.89	3.47	57.4
22X-2, 29–30	202.89		6.90		57.5
22X-3, 29–30	204.39	9.66	6.74	2.92	56.1
22X-4, 29–30	205.89		6.55		54.6
22X-5, 29–30	207.39	10.00	6.14	3.86	51.2
22X-6, 29–30	208.89		6.01		50.1
22X-7, 29–30	210.39	9.75	5.74	4.01	47.8
23X-1, 67–68	211.47		7.17		59.7
23X-2, 0–1	212.30	10.62	7.58	3.04	63.1
23X-2, 31–32	212.61	10.18	7.47	2.71	62.2
23X-3, 30–31	214.10		7.45		62.1
24X-1, 48–49	220.88	12.76	7.27	5.49	60.6
24X-2, 31–32	222.21		7.48		62.3
24X-3, 0–1	223.40	9.85	5.34	4.51	44.5
24X-3, 45–46	223.85	9.74	5.47	4.27	45.6
24X-4, 21–22	225.11		6.82		56.8
24X-5, 44–45	226.84	7.90	6.68	1.22	55.6
24X-6, 47–48	228.37		6.12		51.0
24X-7, 27–28	229.67	9.90	5.89	4.01	49.1

Table 4 (continued).

Core, section, interval (cm)	Depth (mbsf)	Total carbon (%)	Inorganic carbon (%)	Organic carbon (%)	$CaCO_3$ (wt%)
117-723A-					
24X, CC, 44–45	230.27		7.23		60.2
25X-1, 72–73	230.82	10.19	6.90	3.29	57.5
25X-2, 72–73	232.32		6.82		56.8
25X-3, 19–20	233.29	11.07	6.68	4.39	55.6
25X-4, 43–44	235.03		6.64		55.3
25X-5, 43–44	236.53	11.18	6.58	4.60	54.8
25X-6, 43–44	238.03		6.22		51.8
25X-7, 20–21	239.30	10.70	6.07	4.63	50.6
26X-1, 24–25	240.04		5.81		48.4
26X-2, 24–25	241.54	11.20	5.35	5.85	44.6
26X-3, 0–1	242.80	11.99	6.39	5.60	53.2
26X-3, 24–25	243.04		5.83		48.6
26X-4, 24–25	244.54	11.28	6.09	5.19	50.7
26X-5, 24–25	246.04		6.51		54.2
27X-1, 43–44	249.83		6.21		51.7
27X-2, 43–44	251.33	9.30	6.09	3.21	50.7
27X-3, 43–44	252.83		6.12		51.0
27X-4, 43–44	254.33	9.95	6.11	3.84	50.9
27X-5, 43–44	255.83		6.33		52.7
27X-6, 43–44	257.33	9.15	5.63	3.52	46.9
28X-1, 48–49	259.58		6.37		53.1
28X-2, 48–49	261.08	9.43	5.47	3.96	45.6
28X-3, 21–22	262.31		4.97		41.4
29X-1, 43–44	269.13	8.79	5.63	3.16	46.9
29X-2, 43–44	270.63		5.45		45.4
29X-3, 43–44	272.13	12.54	7.75	4.79	64.6
29X-4, 43–44	273.63		5.85		48.7
29X-5, 43–44	275.13	9.98	7.18	2.80	59.8
29X-6, 43–44	276.63		5.65		47.1
29X-6, 119–120	277.39	7.92	3.53	4.39	29.4
30X-1, 0–1	278.30	13.18	8.28	4.90	69.0
30X-1, 62–63	278.92	13.38	8.12	5.26	67.6
30X-2, 24–25	280.04		8.77		73.1
30X-3, 43–44	281.73	13.20	8.40	4.80	70.0
30X-4, 49–50	283.29		6.46		53.8
30X-5, 47–48	284.77	13.09	7.31	5.78	60.9
30X, CC, 40–41	285.71		7.00		58.3
31X-1, 57–58	288.47	12.69	7.17	5.52	59.7
31X-2, 144–145	290.84		8.21		68.4
31X-3, 112–113	292.02	11.90	7.15	4.75	59.6
31X-4, 116–117	293.56		7.75		64.6
31X-5, 92–93	294.82	11.35	7.60	3.75	63.3
31X-6, 90–91	296.30		7.48		62.3
31X-8, 20–21	297.53	9.13	6.76	2.37	56.3
32X-1, 43–44	297.93		6.53		54.4
32X-2, 43–44	299.43	11.51	6.17	5.34	51.4
32X-3, 43–44	300.93		6.44		53.7
32X-4, 43–44	302.43		8.07		67.2
32X-5, 43–44	303.93		7.28		60.6
32X-5, 119–120	304.69	10.36	7.30	3.06	60.8
32X-6, 43–44	305.43		7.39		61.6
33X-1, 40–41	307.50		6.55		54.6
33X-2, 40–41	309.00		5.60		46.7
33X-3, 31–32	310.41		5.72		47.7
33X-4, 40–41	312.00	11.21	6.55	4.66	54.6
33X-5, 40–41	313.50		5.72		47.7
33X-6, 40–41	315.00	13.47	7.63	5.84	63.6
33X-7, 40–41	316.50		5.12		42.7
34X-1, 1–2	316.71	10.69	6.56	4.13	54.6
35X-1, 43–44	321.93		7.32		61.0
35X-2, 45–46	323.45	10.21	6.94	3.27	57.8
35X-3, 45–46	324.95		6.60		55.0
35X-4, 30–31	326.30		6.45		53.7
36X-2, 36–37	327.95	11.42	6.73	4.69	56.1
36X-3, 52–53	329.61		6.08		50.7
36X-4, 43–44	331.02	8.35	4.58	3.77	38.2
36X-5, 35–36	332.44		8.45		70.4
36X-6, 0–1	333.59	7.20	4.29	2.91	35.7
36X-6, 35–36	333.94	9.09	5.77	3.32	48.1
36X-7, 35–36	335.44		7.88		65.6
37X-1, 29–31	336.09	11.88	5.89	5.99	49.1
39X-1, 43–44	355.43		8.76		73.0
39X-2, 46–47	356.96	10.47	8.24	2.23	68.6
39X-3, 46–47	358.46		7.65		63.7
39X-4, 46–47	359.96	10.52	7.47	3.05	62.2
39X-5, 46–47	361.46		6.64		55.3

Table 4 (continued).

Core, section, interval (cm)	Depth (mbsf)	Total carbon (%)	Inorganic carbon (%)	Organic carbon (%)	$CaCO_3$ (wt%)
117-723A-					
39X-5, 119–120	362.19	10.66	6.49	4.17	54.1
39X-6, 46–47	362.96	11.76	6.75	5.01	56.2
40X-2, 83–84	367.03		8.81		73.4
40X-4, 43–44	369.63	8.85	3.68	5.17	30.7
40X-5, 44–45	371.14		7.26		60.5
40X-6, 45–46	372.65	10.71	5.26	5.45	43.8
40X-7, 28–29	373.98		5.88		49.0
40X, CC, 24–25	374.33	5.09			
41X-2, 1–10	375.81		8.35		69.6
41X-3, 44–45	377.74		7.41		61.7
41X-4, 59–60	379.39		3.55		29.6
41X-5, 45–46	380.75		3.91		32.6
41X-6, 45–46	382.25		6.31		52.6
41X, CC, 43–44	382.86		7.72		64.3
42X-1, 43–44	384.43		3.61		30.1

reduced bioturbation and greater organic content in sediments below 230 mbsf.

Silica is preserved in the laminated intervals, but siliceous microfossils only occur in minor abundance adjacent to laminae. High silica flux, rapid burial, and lack of bioturbation appear necessary for the formation of visible laminae at this site. The stratigraphic occurrence of laminae implies that the critical combination of these conditions was met episodically rather than continuously.

The mechanisms which enhance the preservation of silica and organic carbon may also explain the occurrence of laminae in the lower Pleistocene and upper Pliocene. More frequent anoxic conditions would reduce bioturbation, and the thickness of the sediment mixed layer in which silica dissolves would be small. This mechanism is not specifically limited to changes in local productivity and may imply changes in the general circulation and oceanography of the northwest Indian Ocean.

The intensity of the oxygen-minimum zone (OMZ) is controlled, among other things, by the flux of organic matter into the OMZ, the oxygen concentration of the north Indian Ocean deep water, by the lateral advection and diffusion (or lack thereof) of water masses which have a different oxygen content, and by the physical processes which control the stratification of the water column. Tracers of higher productivity, such as isotopic composition and faunal assemblages, may be used to differentiate local from regional productivity changes.

The Owen Ridge sites should record the same productivity signal caused by upwelling, but because they are situated in a different depositional environment, we may be able to distinguish local from regional effects. Thus, the organic-rich laminated facies produced on the Arabian margin reveal past environmental conditions that are strikingly different than modern conditions.

BIOSTRATIGRAPHY

Introduction

Site 723 was drilled on the margin of the western Arabian Sea in order to evaluate the history of the upwelling system in the monsoonal circulation system through time. Nutrient-rich waters injected into the euphotic zone appear to have enhanced blooming of distinctive opportunistic species of the various faunal and floral groups. As a consequence, determination of biostratigraphic zonations is difficult because age-diagnostic species are often lacking or show only scattered occurrences (Figs. 8 and 9). Radiolarians and planktonic foraminifers cannot be

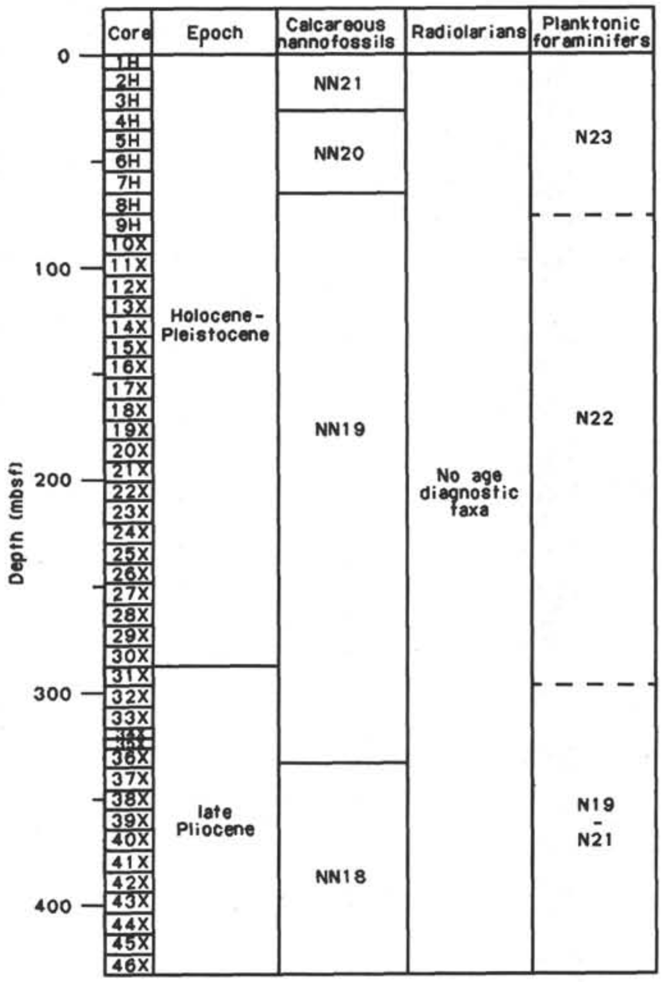

Figure 8. Correlation of planktonic microfossil zones in Hole 723A.

used for stratigraphic purposes at this site. Fortunately, age control is provided by the nannoflora.

The Pliocene/Pleistocene boundary was recognized between Samples 117-723A-30X-5, 89–90 cm, and 117-723A-30X, CC (285.19–287.90 mbsf), and Samples 117-723B-30X, CC, and 117-723B-31X, CC (274.4–303.3 mbsf). A schematic correlation of nannofossil zones at Site 723 is depicted in Figure 10, and a plot of datum levels vs. depth below the seafloor is presented in Figure 11. For a detailed listing of these data points, see Table 5.

Calcareous nannofossils are abundant and well preserved throughout the entire section, whereas planktonic foraminifers are abundant only in the upper part of the sequence (Samples 117-723A-1H, CC, through 117-723A-31X, CC; 7.8–297.5 mbsf), and are sparse downhole. Although radiolarians show a highly scattered pattern, they are most abundant near the Pliocene-Pleistocene boundary. Benthic foraminifers are abundant, well preserved, and highly diverse throughout the sequence studied.

Planktonic Foraminifers

The sequence recovered at Site 723 contains upper Pliocene to Pleistocene foraminifer-bearing marly nannofossil oozes. Only the planktonic foraminifers in Hole 723A core-catcher samples were studied. Assemblages are highly diverse in the upper part of the section, and the preservation state of the calcareous tests is good (Samples 117-723A-1H, CC, to 117-723A-31X,

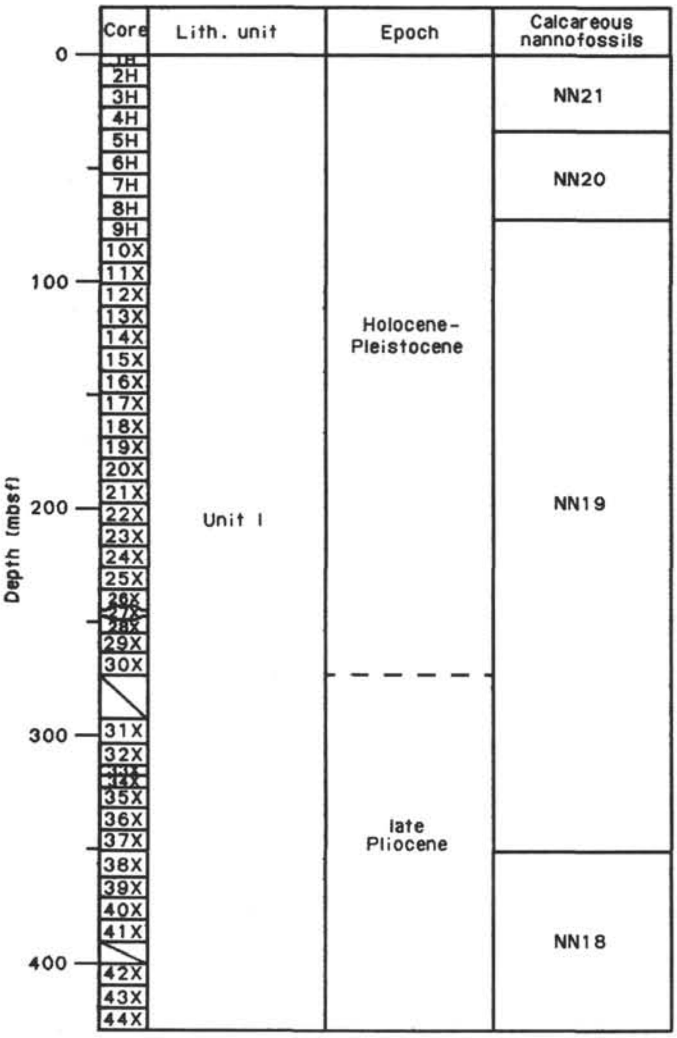

Figure 9. Correlation of planktonic microfossil zones in Hole 723B.

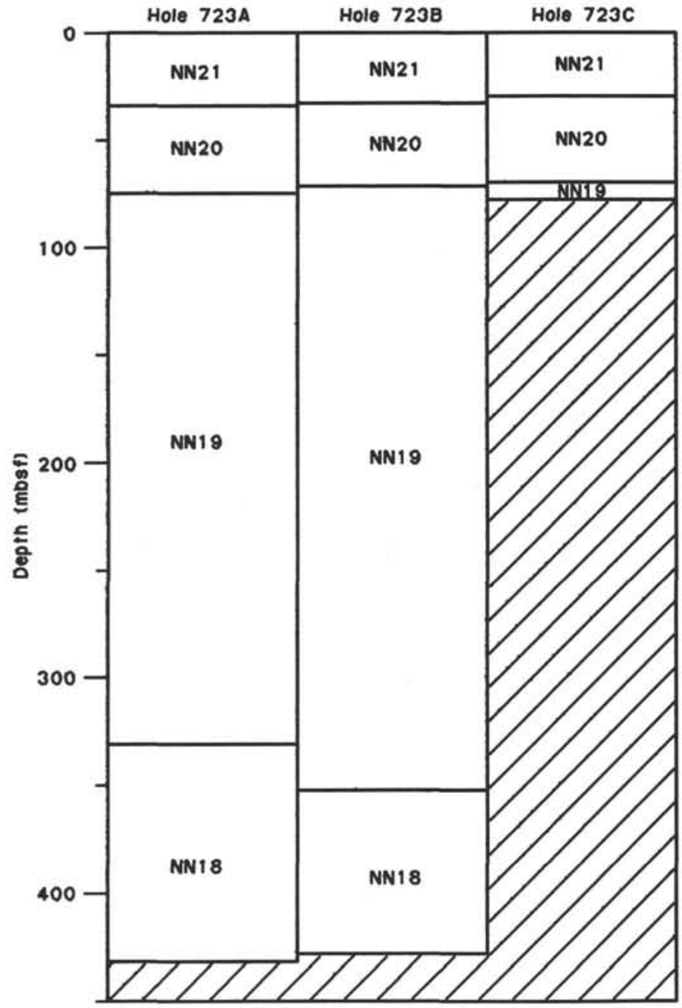

Figure 10. Correlation of nannofossil zones in Holes 723A, 723B, and 723C.

CC; 7.8–297.5 mbsf). Below this level the planktonic foraminifers are sparse and moderately well preserved.

The top part of the Pleistocene sequence is referred to Zone N23 (Samples 117-723A-1H, CC, to 117-723A-8H, CC; 7.8–75.4 mbsf) as indicated by the presence of *Globigerinella calida calida*. Downhole Zone N22, marked by *Globorotalia truncatulinoides*, could be recognized and persists through Sample 117-723A-27X, CC (259.1 mbsf). The Pleistocene/Pliocene boundary could not be determined by using the evolution of this species from *Globorotalia tosaensis* because both species disappear rapidly below this level. Also, the sparse occurrences of other species do not allow accurate positioning of this boundary. A well-developed late Pliocene fauna is present in Sample 117-723A-39X, CC (364.7 mbsf), with abundant *Globorotalia acostaensis*, common *Globigerinoides obliquus*, and rare *Globorotalia limbata*, and can be assigned to Zones N19–N21. Pliocene Zones N19–N21 could not be subdivided because the zonal markers are missing. The remainder of the hole belongs to Zones N19–N21 as well.

The foraminiferal fauna in Hole 723A is characterized by high relative frequencies of *Globigerina bulloides*, *Neogloboquadrina dutertrei*, *Globorotalia menardii*, and *Globigerinita glutinata*. This indicates upwelling conditions throughout the Pleistocene and late Pliocene in this area. Shore-based counts of relative frequencies of key species will unravel the upwelling intensity through time as a response to changes in the monsoonal system.

Benthic Foraminifers

Benthic foraminiferal fauna were studied at Site 723 in the core-catcher samples of Hole 723A. Benthic foraminifers are abundant and well preserved throughout most of the cored sequence, although benthic foraminifers are absent below 393.6 mbsf. The diversity of the fauna is high and most species are present in all of the samples we studied.

The total number of benthic foraminiferal specimens per 10-cm^3 sediment is very high in the upper 230 m (Samples 117-723A-1H, CC, through -24X, CC; 7.8–230.1 mbsf), where it ranges from 4,000 to 13,000 specimens with an average of about 7,000. The average is slightly higher in the upper part. In the samples below 280 mbsf, the average is significantly lower (about 1,500).

The benthic foraminiferal fauna of Site 723 is dominated by *Bolivina pygmaea*, *B. ordinaria*, *Uvigerina auberiana*, and *U. peregrina*. Other species with high relative abundances are *Cassidulina carinata*, *Epistominella exigua*, and *Hyalinea baltica*. Species with lower relative abundance are *Florilus* spp. and *Plectofrondicularia* spp.

The only significant change in the benthic foraminiferal assemblage occurs at about 180 mbsf (Sample 117-723A-19X, CC).

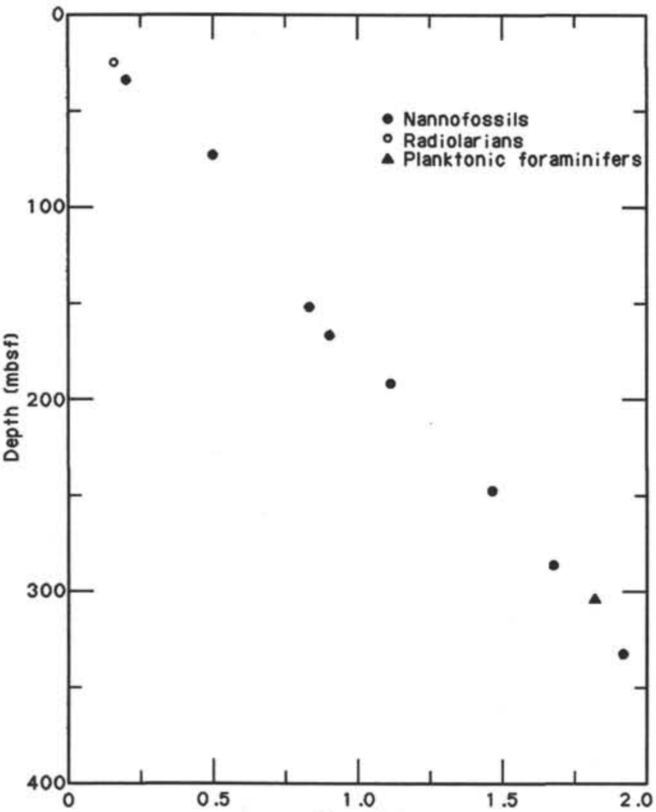

Figure 11. Age-depth plot for Hole 723A. For a detailed listing of datum levels, see Table 5.

Table 5. Chronologic listing of faunal events for Hole 723A.

Event	Core, section, interval (cm)	Depth (mbsf)	Age (Ma)	Source of age
T *Helicosphaera inversa*	117-723A-3H-5, 120–121	24.70	[a]0.15	4
	117-723A-3H, CC	27.10		
B *Emiliania huxleyi*	117-723A-4H-5, 120–121	34.30	0.19	3
	117-723A-4H, CC	36.80		
T *Pseudoemiliania lacunosa*	117-723A-8H-5, 120–121	73.00	0.49	3
	117-723A-8H, CC	75.40		
T *Reticulofenestra* sp. A	117-723A-16X, CC	152.80	0.82	3
	117-723A-17X-1, 90–91	153.70		
B *Gephyrocapsa parallela*	117-723A-17X, CC	162.40	[a]0.89	4
	117-723A-18X, CC	172.10		
T [b]*Gephyrocapsa* "large"	117-723A-20X, CC	191.40	[a]1.10	4
	117-723A-21X-1, 134–135	192.74		
T *Helicosphaera sellii*	117-723A-25X-1, 117–118	231.27	[c]—	—
	117-723A-25X-3, 5–6	233.15		
T *Calcidiscus macintyrei*	117-723A-26X-5, 7–8	245.87	1.45	6
	117-723A-26X, CC	249.40		
B *Gephyrocapsa caribbeanica*	117-723A-30X-5, 89–90	285.19	[d]1.66	4, 8
	117-723A-30X, CC	287.90		
T *Globigerinoides extremus*	117-723A-32X-4, 65–67	302.65	[e]1.80	6
	117-723A-32X, CC	307.10		
T *Discoaster brouweri*	117-723A-36X-3, 127–128	330.36	1.9	6
	117-723A-36X-5, 144–145	333.53		

Note: T = morphotypic top of range and B = bottom of range. Sources of ages are: 3 = oxygen isotope data for Site 723 (N. Niitsuma, unpubl. data); 4 = Takayama and Sato, 1987; 6 = Berggren et al., 1985; and 8 = Sato et al., in press.
[a] North Atlantic data.
[b] Long axis greater than 6μm.
[c] North Atlantic age consistent with Italian-type section.
[d] No good published age; event appears to be diachronous.
[e] *G. obliquus extremus* in Berggren et al., 1985.

At this level *Bulimina truncana*, *Epistominella exigua*, and *Plectofrondicularia* sp. *A* have their last occurrences at this site.

Calcareous Nannofossils

Three holes drilled at Site 723 (Fig. 10) provided a largely overlapping and complete composite section down to the upper Pliocene. Calcareous nannofossils are abundant and well preserved throughout, but species diversity is comparatively low.

Sediments down to 34.30 mbsf in Hole 723A (Samples 117-723A-1H, CC, through 117-723A-4H-5, 120-121 cm), sediments down to 33.3 mbsf in Hole 723B (Samples 117-723B-1H, CC, through 117-723B-4H, CC), and sediments down to 28.5 mbsf in Hole 723C (Samples 117-723C-1H, CC, through 117-723C-3H, CC) are assigned to Zone NN21 because they contain *Emiliania huxleyi*. Datum 1 occurs between Samples 177-723A-3H-5, 120–121 cm, and 117-723A-3H, CC, and in Core 117-723B-4H (23.6-33.3 mbsf) within this zone. Datum 2 is the NN21/NN20 boundary. Since most of the specimens of *E. huxleyi* are too small to identify under the light microscope, this boundary is hard to detect precisely. Datum 3 defines the bottom of Zone NN20.

Sediments from 34.4 to 73.0 mbsf in Hole 723A (Samples 117-723A-4H-5, 120–121 cm, to 117-723A-8H-5, 120–121 cm), sediments from 33.3 to 71.9 mbsf in Hole 723B (Samples 117-723B-4H, CC, to 117-723B-8H, CC), and sediments from 28.5 to 67.2 mbsf in Hole 723C (Samples 117-723C-3H, CC, to 117-723C-7H, CC) belong to Zone NN20. The underlying sediments down to 330.36 mbsf in Hole 723A (Samples 117-723A-8H, CC, through 117-723A-36X-3, 127–128 cm), to 342.2 mbsf in Hole 723B (Samples 117-723B-9H, CC, through 117-723B-36X, CC), and to 76.8 mbsf in Hole 723C (Sample 117-723C-8H, CC) all belong to Zone NN19. The top of *Discoaster brouweri* marks the lower boundary of this zone.

The Pleistocene/Pliocene boundary occurs between Samples 117-723A-30X-5, 89–90 cm, and 117-723A-30X, CC, in Hole 723A (285.19–287.90 mbsf) and between Samples 117-723B-27X, CC, and 117-723B-31X, CC, in Hole 723B (247.2–303.0 mbsf). Underlying sediments contain *Discoaster brouweri* but not *D. pentaradiatus* and are assigned, therefore, to Zone NN18 (Pliocene), which persists to the termination of Holes 723A and 723B.

Throughout Holes 723A and Hole 723B there are traces of reworked nannofossils from the Paleogene and Neogene. *Cyclicargolithus floridanus*, *Sphenolithus abies*, *S. moriformis*, *Discoaster saipanensis*, *D. barbadiensis*, *D. deflandrei*, *D. druggii*, *Reticulofenestra pseudoumbilica*, *Dictyococcites bisectus*, and *D. dictyodus* were encountered.

Samples 117-723A-27X, CC, through 117-723A-38X, CC (259.1–355.0 mbsf), and Sample 117-723B-33X, CC (317.4 mbsf), contain numerous specimens of *Coccolithus pelagicus*. One thin lamina (about 1 mm; Sample 117-723A-35X-3, 46 cm) consists of a bloom of *C. pelagicus* with a few specimens of *Discoaster brouweri*. *Coccolithus pelagicus* is known to be a cold-water species.

Many species of *Helicosphaera* are found more commonly in hemipelagic sediments; they are usually very rare or absent in pelagic sediments. The possibility exists that this genus is restricted to, or prefers, areas of upwelling (Perch-Nielsen, 1984). *Helicosphaera* species are especially numerous in Samples 117-723A-32X, CC (307.1 mbsf), 117-723A-33X, CC (316.7 mbsf), 117-723A-35X, CC (326.3 mbsf), and 117-723A-39X, CC (364.7 mbsf).

A single specimen of *Braarudosphaera bigelowi* was recovered from Sample 117-723B-35X, CC (332.5 mbsf). This is a typical shallow-water species (Martini, 1967; Takayama, 1972).

Radiolarians

We examined all core-catcher samples from Hole 723A for radiolarians; we did not study samples from Holes 723B and 723C. Radiolarian abundances vary from barren to common, with peak abundances ("common") in Samples 117-723A-5H, CC (46.4 mbsf), 117-723A-33X, CC, through 117-723A-37X, CC (316.7-345.4 mbsf), 117-723A-41X, CC (384.0 mbsf), and 117-723A-42X, CC (393.6 mbsf). The core-catcher samples from the following cores contained "few" radiolarians: 117-723A-15X (143.1 mbsf), 117-723A-22X (210.8 mbsf), 117-723A-24X (230.1 mbsf), 117-723A-29X (278.3 mbsf), 117-723A-32X (307.1 mbsf), and 117-723A-40X (374.3 mbsf).

In general, diatom abundances are in concert with radiolarian abundances. Considerable detrital material was found in all processed samples. Low radiolarian abundances could, therefore, reflect low-standing crops or masking by detritus or a combination of both conditions.

All the usual tropical Pleistocene and upper Pliocene zonal markers are absent. All elements of the *Lamprocyrtis heteroporos* to *Lamprocyrtis nigriniae* lineage are present, but their sporadic occurrences in this material provide unreliable datum levels.

The criteria described by Johnson and Nigrini (1982) for a modern Arabian Upwelling Assemblage were tested on the uppermost sample containing common radiolarians (i.e., Sample 117-732A-5H, CC). This assemblage is dependent upon the presence of their Recurrent Group D′ (*Collosphaera* cf. *huxleyi*, *Lamprocyclas maritalis ventricosa*, and *Lamprocyrtis nigriniae*) and the absence of a majority of the species belonging to their tropical Recurrent Group A′. Sample 117-723A-5H, CC, does contain the Arabian Upwelling Assemblage. In addition, two species (*Lithostrobus* cf. *hexagonalis* and *Acrosphaera murrayana*) associated with the Peru Current upwelling (Nigrini, 1968), but not included in Johnson and Nigrini's (1982) study, are consistently present in Hole 723A.

Paleoenvironmental Implications

Upwelling conditions are clearly indicated by the planktonic foraminifers, with well-known tropical upwelling species like *Globigerina bulloides* and *Neogloboquadrina dutertrei* dominating the fauna throughout the section. Also, numerous specimens of *Coccolithus pelagicus* (nannoflora) in Samples 117-723A-32X, CC, through 117-723A-39X, CC (316.7–364.7 mbsf) indicate relatively cold water. *Helicosphaera*, a genus thought to prefer upwelling areas, is abundant in some of these same cores as well. Counts of relative abundances are required to record upwelling intensity through time.

The presence of the hyaline benthic foraminifer, *Hyalinea baltica*, throughout the sequence is interesting since it is considered to be a species indicative of cool-water masses. If the relative abundance of *H. baltica* is dependent upon the temperature of the water mass, then Site 723 must have been located within this cool-water mass during at least the late Pliocene and Pleistocene.

PALEOMAGNETISM

Introduction

Site 723 is located at 18°03.079′N, 57°36.561′E, in water depths of about 800 m on the Oman margin. Holes 723A, 723B, and 723C were cored to depths of 432.3 mbsf, 400.1 mbsf, and 76.8 mbsf, respectively. The lithology consisted predominantly of marly nannofossil ooze and calcareous clayey silt.

Magnetic Measurements

We measured the archive halves of Cores 117-723A-1H through 117-723A-9H and Cores 117-723B-1H through 117-723B-9H using the whole-core, pass-through cryogenic magnetometer, after alternating-field (AF) demagnetization at 5 mT. On the basis of these results, the sediments appeared to be less severely affected by the coring-induced remanence seen at Sites 720–722 on the Owen Ridge. Moreover, the inclination values after AF demagnetization at 5 mT generally accorded with the expected geocentric axial dipole values for the site latitude. The failure to acquire a significant coring remanence appears to be an intrinsic property of the Oman margin sediments, because we only succeeded in demagnetizing the APC barrels to an acceptable level after Hole 723B had been cored.

Figure 12 shows the combined results of measurements of discrete samples on the Molspin Minispin magnetometer after AF demagnetization at 5 or 10 mT. Figure 13 shows the remainder of the same data set after removing points with circular standard deviation (CSD) values >40°. The intensities are weak, generally <1 mA/m (arithmetic mean = 0.6 mA/m). A marked drop in intensity below about 100 mbsf is accompanied by a rise in the CSD and an obvious increase in the scatter of the inclinations. The transition from higher to low intensities does not correspond to an obvious lithostratigraphic change.

The results of stepwise AF demagnetization (Figs. 14–17) show that sample behavior during demagnetization tends to become more erratic with increasing depth, which coincides with a reduction in the median destructive field of the natural remanent magnetization (NRM) from ~15–20 mT to <10 mT. According to the nannofossil stratigraphy (see "Biostratigraphy" section, this chapter), the Chron C1/C1r (Brunhes/Matuyama Chronozone) boundary should occur between 100 and 150 mbsf. However, with the exception of a few reversed samples over this interval, it is not clearly reflected in the inclination plot (Fig. 13).

Also, although most of the interval between 100 and 400 mbsf corresponds to Chron C1r (Matuyama Chronozone), there is an absence of reversely magnetized samples (an exception is the interval between about 200 and 250 mbsf, with consistent reversed inclinations corresponding to a zone of higher intensities). The histogram of the distribution of inclinations within 10° classes (Fig. 18) illustrates this normal magnetization bias. On the basis of the above, we concluded that the sediments at Site 723 are relatively poor geomagnetic field recorders and that little reliable magnetostratigraphic information can be obtained from the data set.

The only other feature of interest in the inclination record is the zone of shallow inclinations with two reversed specimens at about 80 mbsf. The interval above 100 mbsf in Figure 13 consists entirely of specimens from Hole 723A. This zone of shallow inclinations was also evident in the archive-half cryogenic results from Core 117-723A-9H. However, it was not evident in the archive-half cryogenic data from the same sub-bottom depth interval in Hole 723B, despite the fact that a comparison of the susceptibility records for Holes 723A and 723B suggests insignificant offset between the two holes. At present, we are unable to determine whether its origin is sedimentologic, geomagnetic, or a coring artifact.

A question arises regarding the reason for the drastic reduction in NRM intensity below 100 mbsf at this site. Figure 19 shows plots of NRM intensity, magnetic susceptibility, and the Königsberger ratio (Q = NRM/susceptibility). The susceptibility values are from the results of whole-core measurements. The NRM decrease is accompanied by a decrease in Q-ratio, which suggests a coarsening of the magnetic grain-size distribution. Several causes are possible: (1) a reduction in the flux (biogenic or detrital) of fine-grained magnetic material to the sediments; (2) destruction of fine magnetic grains by reduction diagenesis (Canfield and Berner, 1987); and/or (3) randomization of fine magnetic grains by gas expansion, which began to be evident below 70 mbsf at this site (in which case the NRM decrease would not necessarily reflect a reduction in the concentration of fine-grained magnetic material).

At present we are unable to decide which of the above factors is the most likely. The third cause can be tested by measurements of anhysteretic remanence across the interval. The second factor is well-documented in marine sediments with high concentrations of organic matter and active sulfate reduction (such

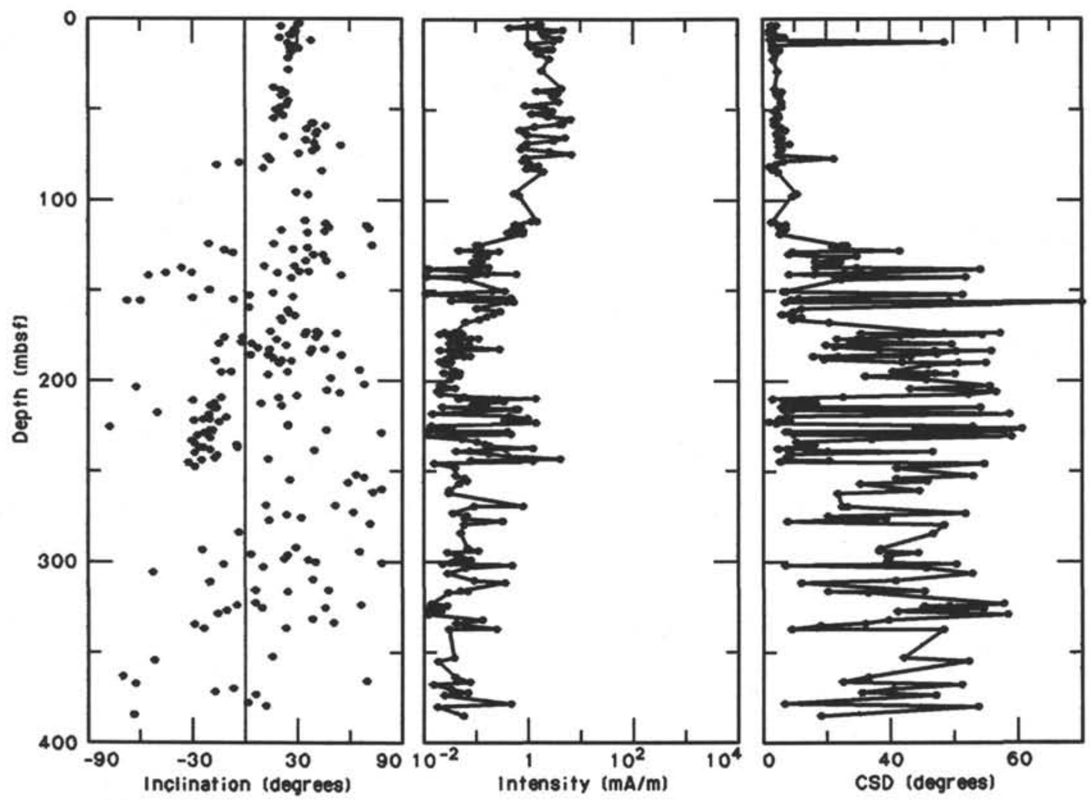

Figure 12. Inclination, natural-remanent-magnetization (NRM) intensity after 5- or 10-mT alternating field (AF) demagnetization, and circular standard deviation (CSD) for the combined discrete sample data from Holes 723A and 723B.

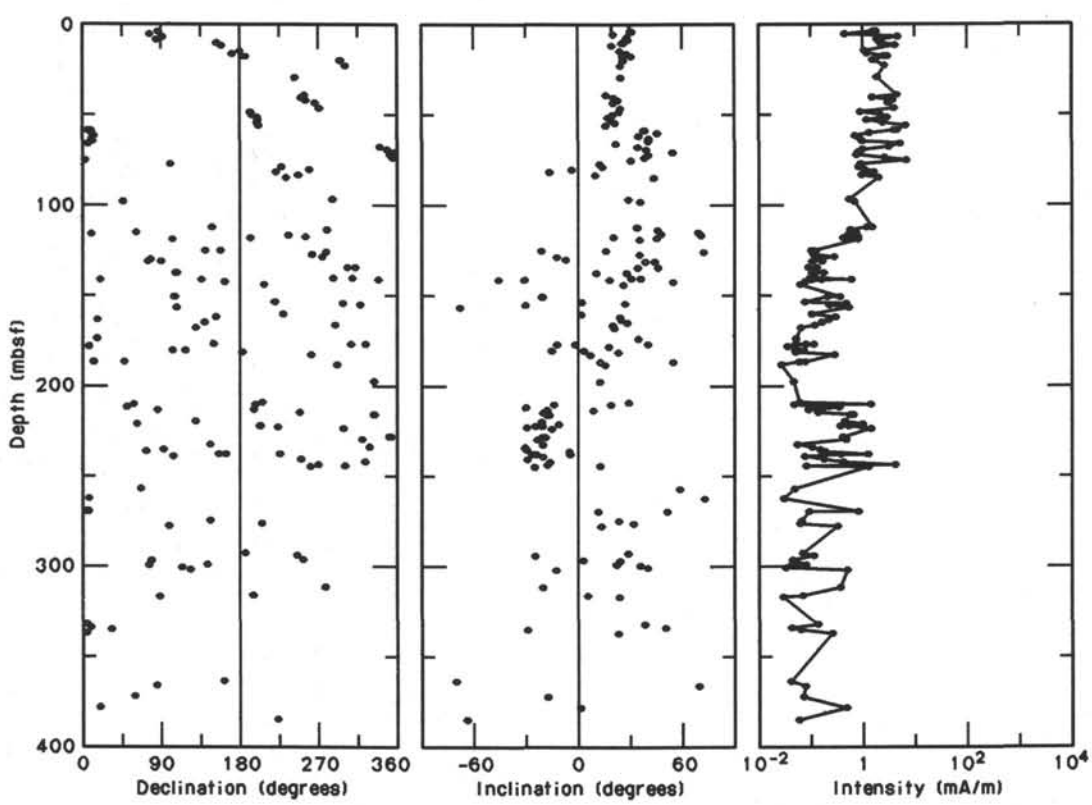

Figure 13. Declination, inclination, and NRM intensity after 5- or 10-mT AF demagnetization for the data set shown in Figure 12 after the removal of specimens with CSD values >40.

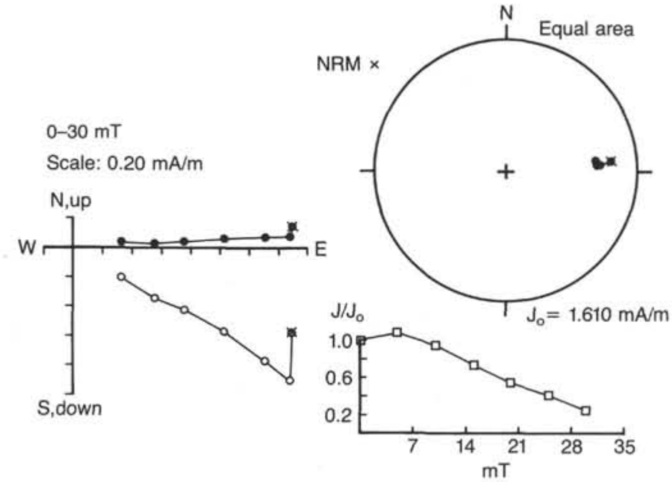

Figure 14. Results of stepwise AF demagnetization of Sample 117-723A-1H-2, 115 cm, from Hole 723A.

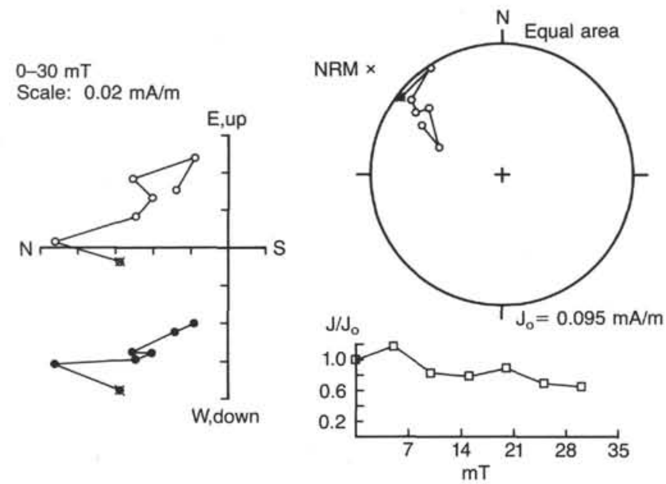

Figure 17. Results of stepwise AF demagnetization of Sample 117-723B-19X-6, 66 cm, from Hole 723B.

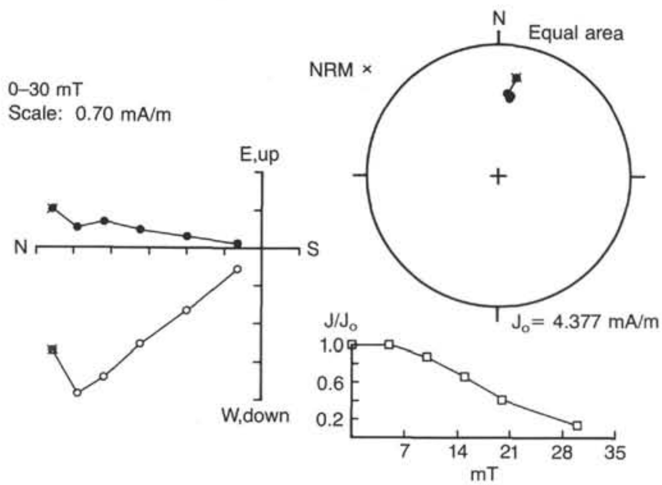

Figure 15. Results of stepwise AF demagnetization of Sample 117-723A-7H-2, 120 cm, from Hole 723A.

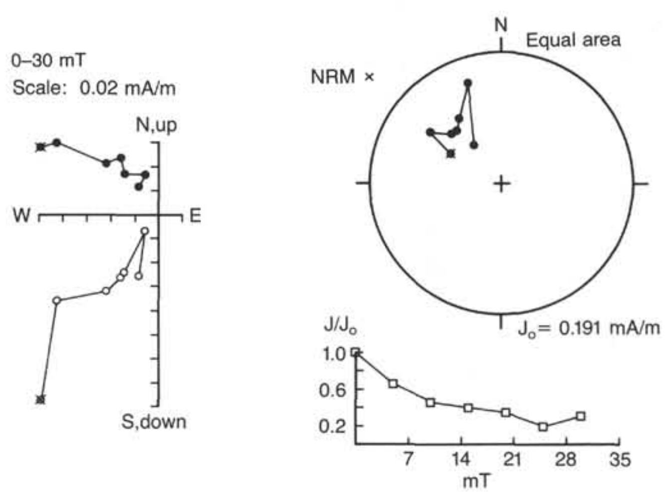

Figure 16. Results of stepwise AF demagnetization of Sample 117-723A-15X-1, 45 cm, from Hole 723A.

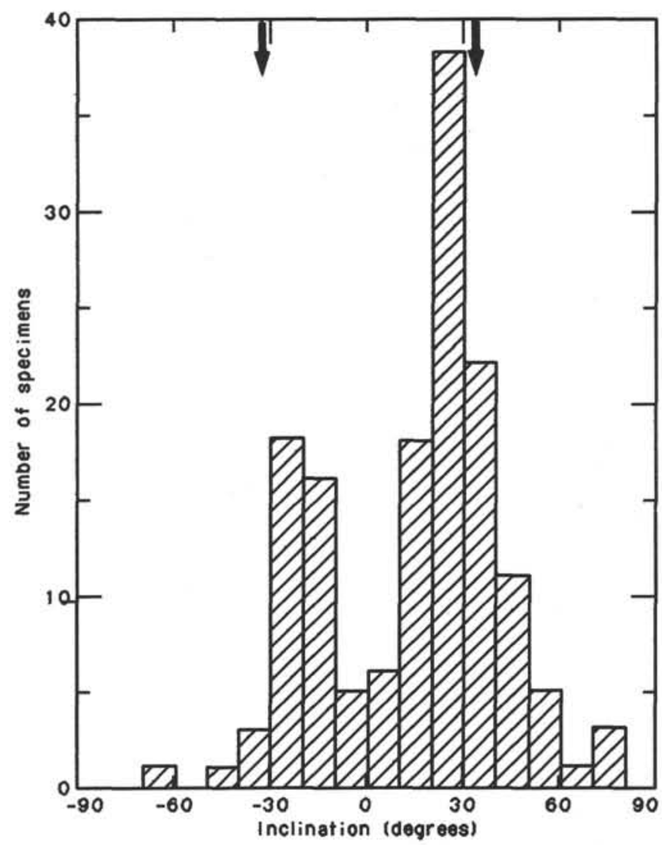

Figure 18. Inclination values grouped into 10° classes for discrete specimens from Holes 723A and 723B. Arrows show the expected geocentric axial dipole inclination values for the site latitude.

as the sediments at Site 723). However, it is interesting that the results of the pore-water geochemistry (see "Inorganic Geochemistry" section, this chapter) show that sulfate declines to low levels well above the zone of NRM decrease. In previous studies of the relationship between sulfate reduction, magnetite dissolution, and pyritization, the three phenomena have tended to occur concurrently (e.g., Canfield and Berner, 1987).

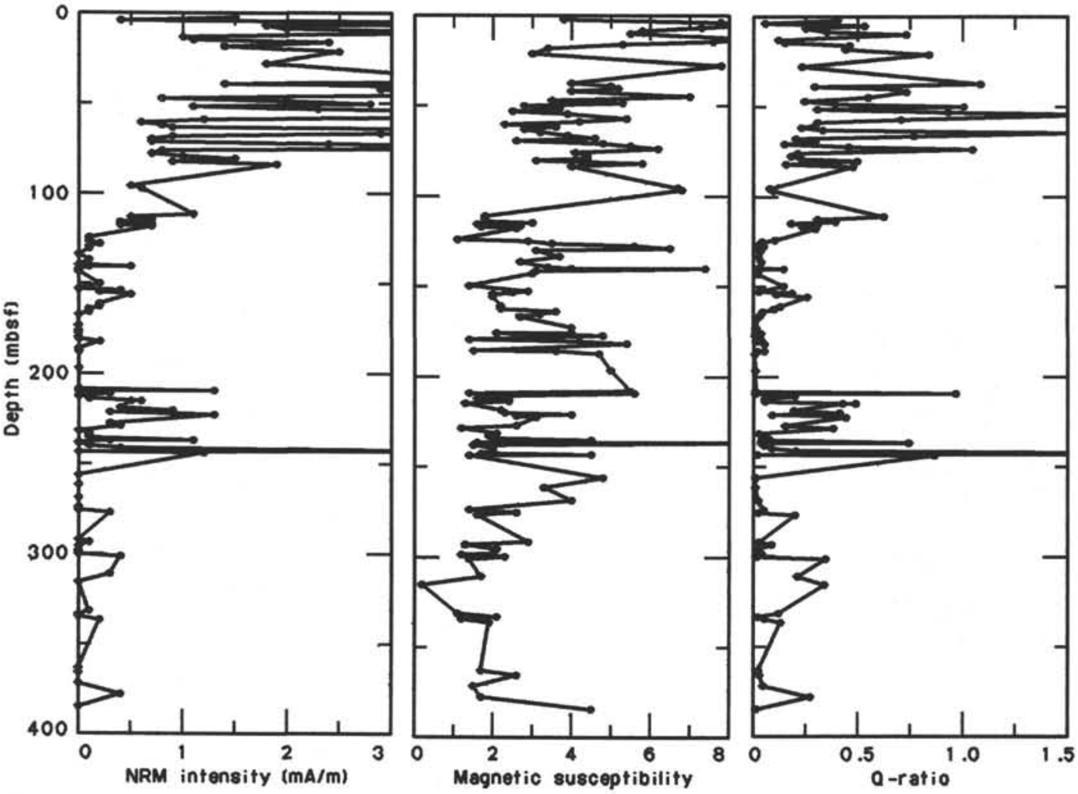

Figure 19. NRM intensity, magnetic susceptibility, and Q-ratio (NRM/susceptibility) for combined discrete samples from Holes 723A and 723B.

Core Orientation

Table 6 shows a comparison of multishot core orientation estimates with estimates obtained by averaging within-core declination values. As at previous sites, there is a notable discrepancy between the two estimates.

Magnetic Susceptibility

The volume magnetic susceptibility of Holes 723A and 723B was measured on a Bartington Magnetic Susceptibility Meter and MS1 sensor. The cores were measured at 5-cm intervals using the low-frequency (0.47 kHz) and high-sensitivity (0.1) settings. We cored Hole 723A with the APC to Core 117-723A-9H (85.1 mbsf) and drilled in the XCB mode from Core 117-723A-10X to -46X (432.3 mbsf). We cored Hole 723B with the APC to Core 117-723B-9H (81.6 mbsf) and with the XCB from Core 117-723B-10X to -44X (429.0 mbsf, core interval 400.1 m). Hole 723C was dedicated to pore-water analyses, so susceptibility was not measured. All cores were measured at 10-cm intervals because of the high accumulation rates expected at this site.

Table 6. Comparison of estimates of core orientation obtained from the multishot with estimates from mean within-core declination data.

Core	Multishot orientation (degrees)	Measured mean declination (degrees)	Corrected mean core declination (degrees)
117-723A-6H	224	199 (N)	335
117-723A-7H	233	10 (N)	137
117-723A-8H	25	354 (N)	329
117-723A-9H	346	239 (N)	253

The susceptibility records from both holes were generally well defined down to Cores 117-723A-6H and 117-723B-6H (~55 mbsf). Below this depth, however, gas expansion tended to disturb the record. To accommodate the shifting of sediment that occurred in these cores during core-splitting procedures, half-round sections rather than whole-round sections were measured below Cores 117-723A-27X and 117-723B-13X. The susceptibility data from half-round sections were multiplied by 2 during data processing so that they would be roughly comparable with the data obtained from whole-round sections. Ultimately, this proved to be a rather fruitless effort since gas expansion also had the effect of decreasing the volume of sediment measured by the susceptibility sensor.

For both holes, the susceptibility record below ~100 mbsf was generally too disturbed and discontinuous to be interpreted reliably, so only the uppermost 100 meters are presented in this report (Figs. 20 and 21). Above 100 mbsf, however, some correlations are possible between Holes 723A and 723B from the Oman margin with Holes 722 and 721 from the Owen Ridge. Detailed interhole correlations based on these data and lithologic marker layers are presented in the "Interhole Correlation" section of this chapter.

The uppermost ~100 meters of the Site 723 holes are roughly correlative with the uppermost ~25 meters of the holes in Sites 722 and 721 (Fig. 22). Despite the differing depositional regimes of the Owen Ridge site (722B) and the Oman margin site (Holes 723A and 723B), the major features of the susceptibility records are generally correlative. The degree of correlation is remarkable considering the fourfold difference in accumulation rates and the broadly different depositional settings. Susceptibility values for Site 723 ranged from ~25 to 100 X 10^{-6} volume SI units, which is somewhat lower than the range observed for the Owen Ridge sites. The lower values at Site 723 may reflect dilution by nonmagnetic terrigenous and/or biogenic components.

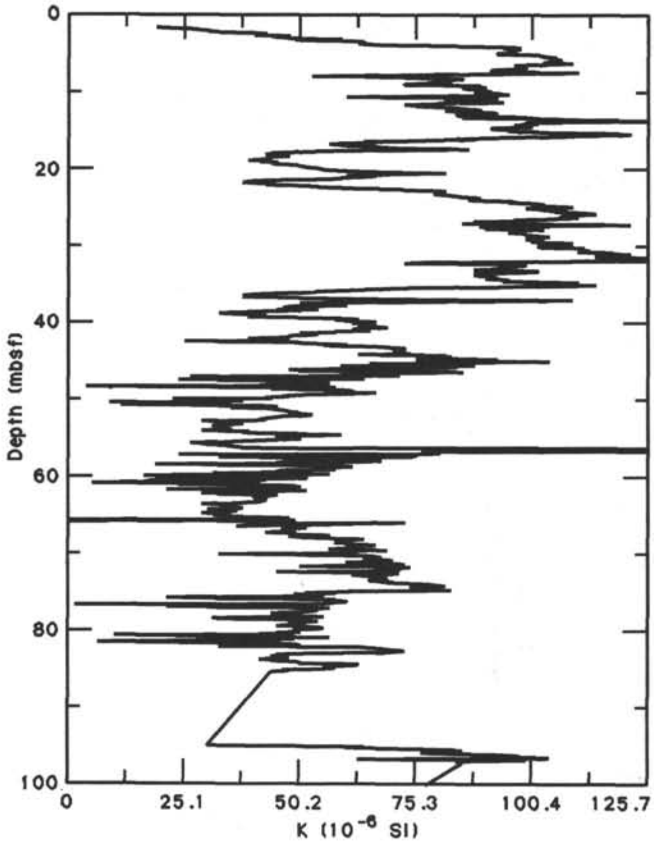

Figure 20. Whole-core magnetic susceptibility for 0 to 100 mbsf, Hole 723A.

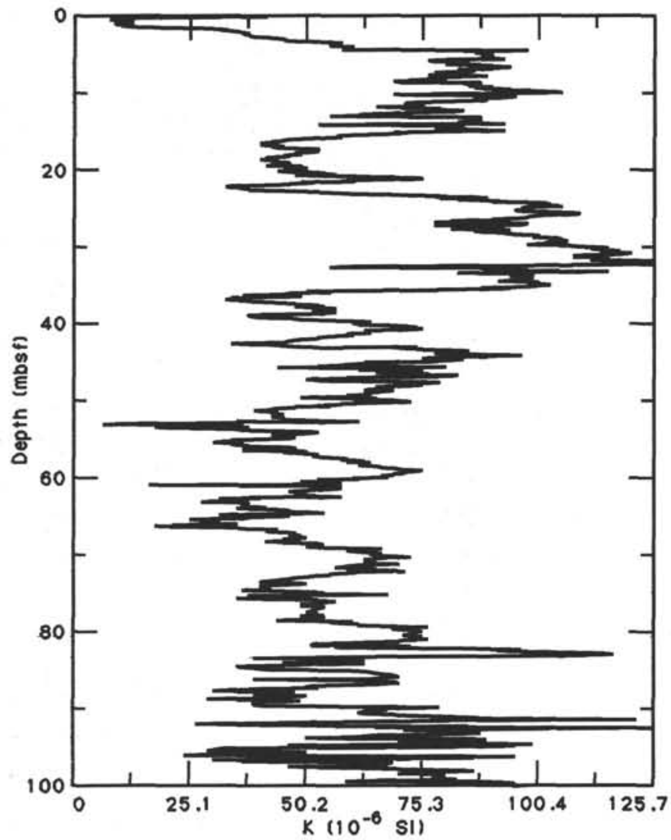

Figure 21. Whole-core magnetic susceptibility for 0 to 100 mbsf, Hole 723B.

It is interesting to consider the differences in susceptibility accumulation between the Owen Ridge and Oman margin sites. Since the susceptibility measurements are volumetrically based, the unit of measurement in SI units is dimensionless. Therefore, to calculate susceptibility accumulation, the data should be multiplied by the applicable sedimentation rates. The susceptibility accumulation rates presented here are calculated for the first major sub-bottom increase in susceptibility for Sites 720, 721, 722, and 723, which is roughly coincident with isotopic Stage 2 at ~18 k.y. For Holes 723A and 723B, this level occurs at ~5 mbsf. These data were compiled from the respective Leg 117 site reports and are shown in Table 7.

These preliminary results suggest that the Indus Fan Site 720 and the Owen Ridge Sites 721 and 722 have very similar susceptibility accumulation rates during this time, whereas the Oman margin Site 723 has nearly twice this rate for the same interval. These preliminary findings may suggest a local and possibly eolian supply of terrigenous ferrimagnetic particles, as was indicated from the X-ray diffraction data of Site 722 (see "Paleomagnetism" section, "Site 722" chapter, this volume). At present, however, the high susceptibility accumulation rate at Site 723 may be either the consequence of local sediment ponding of terrigenous sediments or increased proximity to an eolian source.

ACCUMULATION RATES

Sedimentation rates for Site 723 are based on biostratigraphic datum levels identified in Hole 723A (Table 5). Rates are determined between six datums which are assigned ages based on oxygen isotope stratigraphy (Niitsuma, unpubl. data) or from Berggren et al. (1985; Table 8 and Figs. 23 and 24). Sediments accumulated at Site 723 faster than at any other site cored during Leg 117, with rates ranging from 129 to 240 m/m.y. and a mean of 175 m/m.y. for the last 1.9 m.y. These values are typical of hemipelagic sedimentation and are about five times faster than pelagic accumulation on the Owen Ridge (see "Accumulation Rates" sections, "Site 721," "Site 722," and "Site 731" chapters, this volume).

The mass accumulation of calcium carbonate, organic carbon, and noncarbonate sediment components are calculated from average values between the datum levels (Table 8 and Fig. 24). Total accumulation averages 20 g/cm^2/k.y., with more than one half of this value attributed to calcium carbonate. Since significant detrital calcite was recognized in smear slides (see "Lithostratigraphy" section, this chapter), the accumulation of calcium carbonate has both detrital and pelagic components.

A general decrease in organic carbon accumulation is observed from the late Pliocene to the Holocene at Site 723. The maximum organic carbon accumulation near the Pliocene-Pleistocene boundary (~900 mg C/cm^2/k.y.; Table 8) is more than twice late Pleistocene levels and corresponds to a time when laminae and opaline microfossils were preserved at Site 723. These high values are 20–30 times the accumulation of organic carbon at the Owen Ridge sites.

PHYSICAL PROPERTIES

Introduction

The measurement of physical properties at Site 723 was severely hampered by the abundance of gas and the accompanying sediment expansion and disturbance. Discrete samples were taken from the least disturbed intervals for measurement of index properties (wet-bulk density, porosity, water content, and grain density). Vane shear strength measurements were limited to the APC cores. Compressional-wave velocity measurements

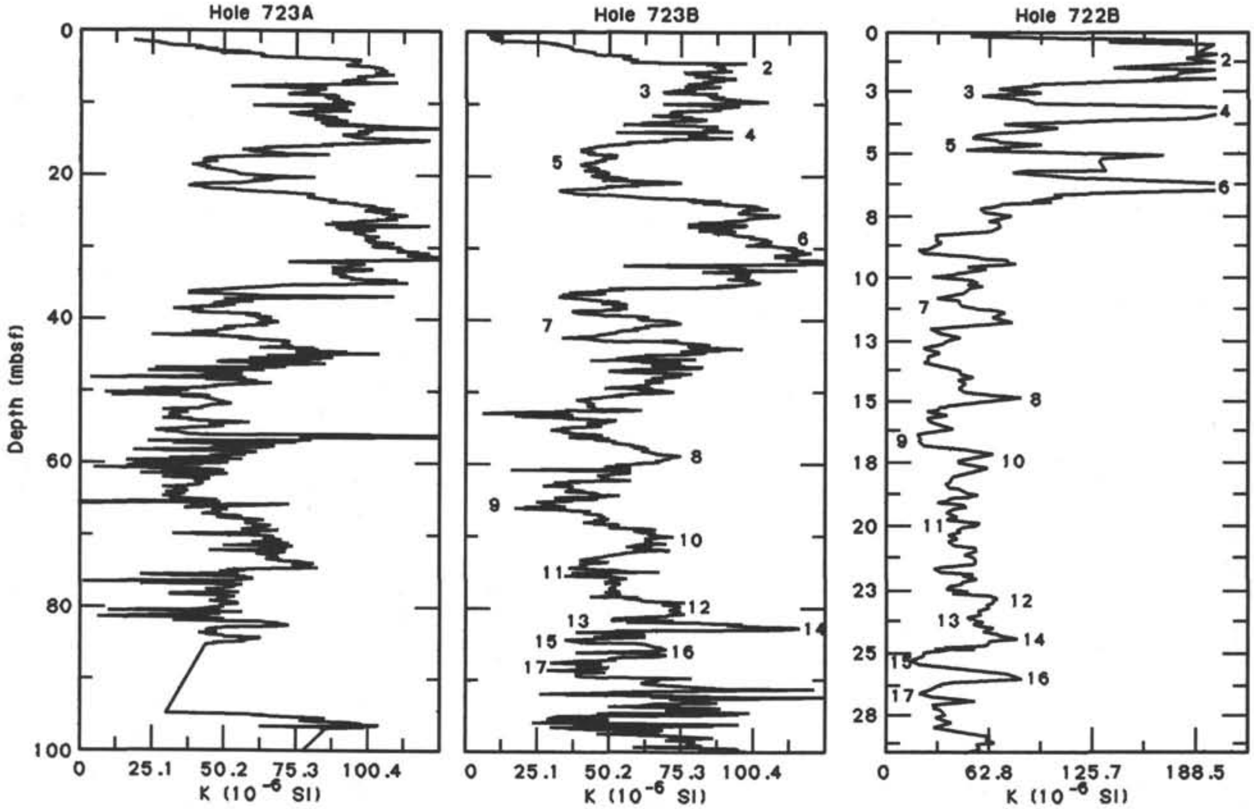

Figure 22. Preliminary correlations between the Oman margin (Holes 723A and 723B) and Owen Ridge (Hole 722B).

Table 7. Preliminary estimates of susceptibility flux, calculated as the product of accumulation rate and dimensionless susceptibility, for Sites 720, 721, 722, and 723.

Site	Accumulation rate (m/Ma)	"Stage 2" susceptibility	Flux
720	30.0	23.0	690
721	43.0	16.0	688
722	47.0	15.5	728
723	185.0	7.1	1313

Note: The Indus Fan (720) and Owen Ridge (721 and 722) sites have comparable susceptibility fluxes, whereas the Oman margin (723) site is more than twice this value.

in the Hamilton Frame were only successful in the indurated dolomites of Facies II.

Wet-bulk density and compressional-wave velocity were measured on the least disturbed, most coherent, whole-round core sections in the GRAPE and *P*-wave logging systems. Only those cores from the upper 50 m of each hole, however, yielded reliable data. All techniques and equipment used are described in the "Explanatory Notes" (this volume).

Index Properties

Throughout Holes 723A and 723B the index properties of the sediments display trends with depth that are controlled not only by increasing overburden pressures but also by changes in sediment composition (Fig. 25). The entire section at Site 723 is characterized by relatively low wet-bulk and grain densities because of the high organic carbon content that averages 2.5% in the upper 200 m of the section and 4.5% in the remainder of the drilled sequence.

In the uppermost portion of the foraminifer-bearing marly nannofossil ooze and calcareous clayey silts in Facies I, porosity and water content averages decrease relatively rapidly from 66% and 42%, respectively, near the seafloor to 56% and 30%, respectively, at 195 mbsf. The average wet-bulk density increases from 1.65 to 1.75 g/cm^3 over this interval, in response to the decreasing water content. The bulk densities also show considerable variation that is attributable to changes in grain density.

Table 8. Sedimentation and accumulation rate data for the top 330 m of Site 723.

Depth interval (mbsf)	Age range (m.y.)	$CaCO_3$ ($\overline{X}$ %)	C_{org} ($\overline{X}$ %)	Dry-bulk density ($\overline{X}$ g/cm^3)	Sed. rate ($\overline{X}$ m/m.y.)	$CaCO_3$ acc. rate (g/cm^2/k.y.)	Non-$CaCO_3$ acc. rate (g/cm^2/k.y.)	C_{org} acc. rate (mg/cm^2/k.y.)
0–35.6	0–0.19	52.6	2.76	0.924	187.4	9.11	8.21	477.9
35.6–74.2	0.19–0.49	61.1	2.57	1.035	128.7	8.14	5.18	342.3
74.2–153.3	0.49–0.82	60.2	2.68	1.064	239.7	15.35	10.15	683.5
153.3–247.6	0.92–1.45	55.6	3.27	1.143	149.7	9.51	7.60	559.5
247.6–286.5	1.45–1.66	55.2	4.2	1.106	185.2	11.31	9.18	860.3
286.5–331.9	1.66–1.9	56.3	4.43	1.089	189.2	11.60	9.00	912.8

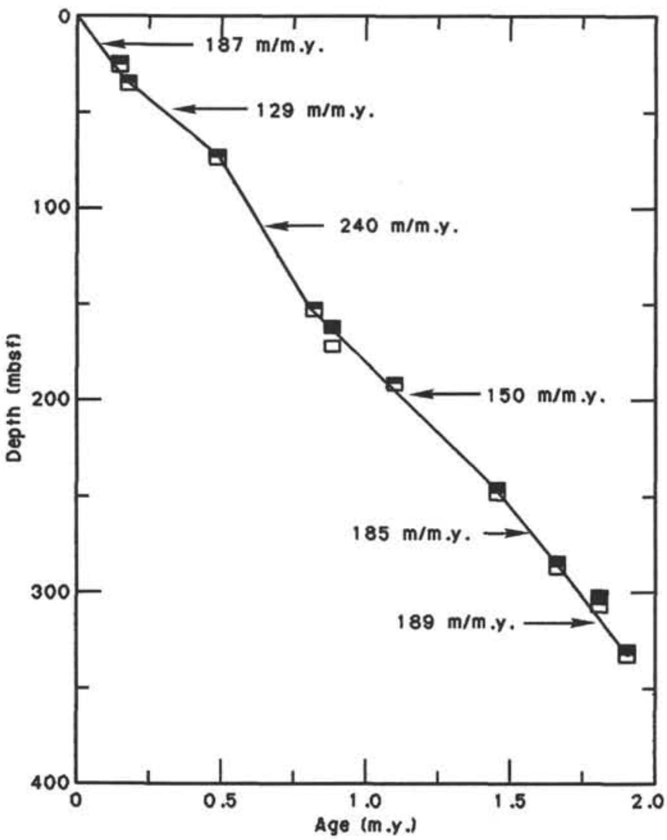

Figure 23. Age-depth plot of stratigraphic datums listed in Table 5. The filled and open boxes are the upper and lower depths of each datum level, respectively. Indicated sedimentation rates are calculated between reliable datum levels.

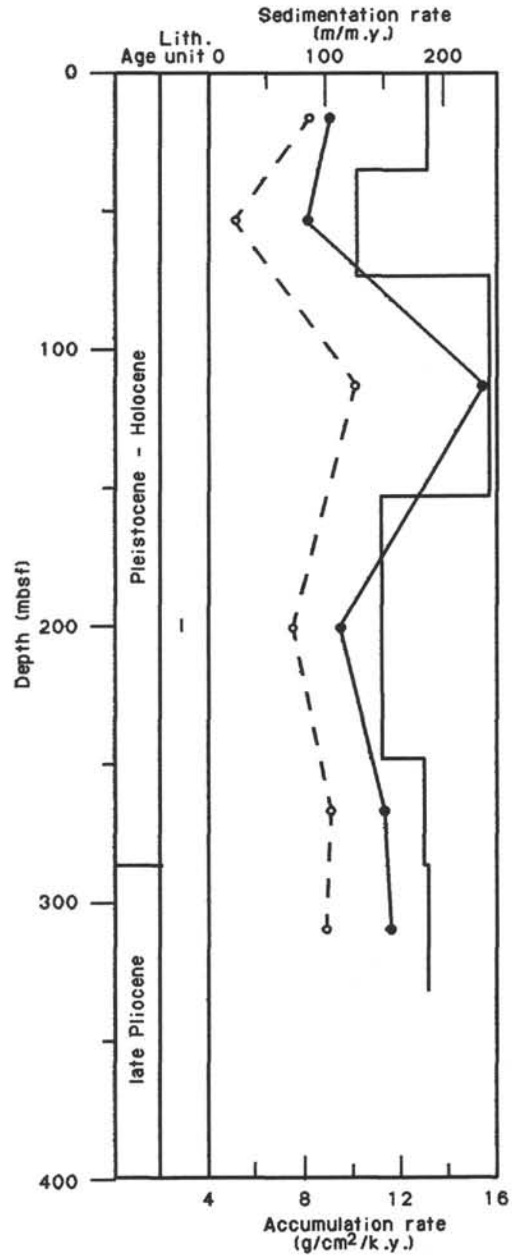

Figure 24. Sedimentation rate (m/m.y.; solid line), calcium carbonate accumulation rate ($g/cm^2/k.y.$; dots), and noncarbonate accumulation rate ($g/cm^2/k.y.$; circles) vs. depth (mbsf) at Site 723. Accumulation rates are plotted at the midpoint of the respective depth intervals.

Grain densities vary from a minimum of 2.267 g/cm^3 in a diatom-rich layer (Facies II) in Core 117-723B-18X to a maximum of 2.648 g/cm^3 in Core 117-723A-4H, but they average 2.50 g/cm^3. Varying concentrations of calcium carbonate and organic carbon are most likely responsible for the variation in grain density through this interval (Fig. 26).

Between 195 and 270 mbsf calcium carbonate decreases and organic carbon increases in abundance, and the porosity and water content are relatively constant at 56% and 32%, respectively. Wet-bulk density decreases from 1.75 to 1.70 g/cm^3 over this interval in response to a continuous decrease in grain density from 2.60 to 2.40 g/cm^3 that is associated with an increase in the abundance of radiolarians and diatoms (see "Biostratigraphy" section, this chapter). This portion of the section also shows a distinctly higher average organic carbon content (4.5%) than the overlying sequence (2.5%).

In the interval from 270 to 340 mbsf, the average values of water content and porosity increase slightly with depth (i.e., from 54% to 62% and from 32% to 40%, respectively). Local maxima in porosity and water content of 63% and 40%, respectively, occur coincidently with an increase in calcium carbonate content to 70% near 280 mbsf (Figs. 25 and 26). Average values of wet-bulk density increase slightly from 270 to 340 mbsf, but individual values vary widely. Grain densities vary widely in response to fluctuations in the abundance of radiolarians and diatoms and are primarily responsible for controlling variations in bulk density.

Throughout the basal sequence (360–410 mbsf), continuous decreases in wet-bulk density (from 1.75 to 1.50 g/cm^3) and in grain density (from 2.55 to 2.20 g/cm^3) reflect a marked increase in the occurrence of radiolarians and diatoms. The gradual increase in porosity and water content throughout this interval can be attributed to the more open sediment fabric created by the occurrence of abundant siliceous microfossils.

The wet-bulk density of four samples of dolomites of Facies II from Holes 723A and 723B were measured using 2-min GRAPE counts (Table 9). Wet-bulk densities of these samples ranged from 2.71 to 2.77 g/cm^3.

Compressional-Wave Velocity

Compressional-wave velocities were measured on four dolomite samples from Holes 723A and 723B (Table 9). Velocities

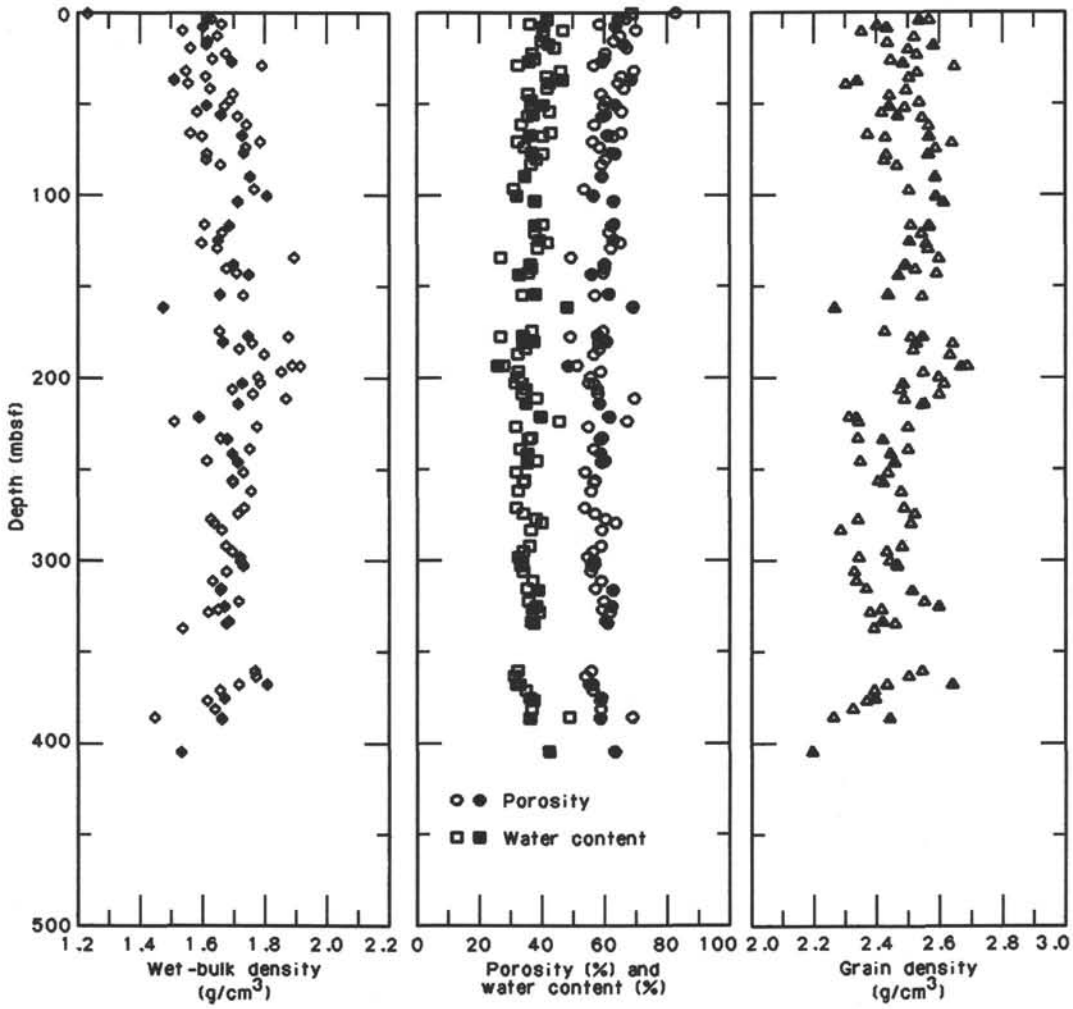

Figure 25. Index properties (wet-bulk density, porosity, water content, and grain density) measured on discrete samples from Holes 723A (open symbols) and 723B (solid symbols). Values are not corrected for sediment expansion.

perpendicular to bedding ranged from 4467 to 5383 m/s. Velocities parallel to bedding averaged 9% higher than those perpendicular to bedding, ranging from 4944 to 5560 m/s.

GRAPE and *P*-Wave Logs

Acquisition of continuous GRAPE and *P*-wave logs at Site 723 was limited by gas-induced sediment expansion. Useful GRAPE records were obtained for the intervals cored with the APC (Cores 117-723A-1H through -9H and Cores 117-723B-1H through -9H). Accurate wet-bulk-density determination by the GRAPE was limited to Cores 117-723A-1H to -4H (0–36.8 mbsf) and Cores 117-723B-1H to -5H (0–42.9 mbsf).

A comparison of GRAPE records and measurements on discrete samples indicates that below 36.8 mbsf in Hole 723A and below 42.9 mbsf in Hole 723B GRAPE density is less than the actual wet-bulk density (Fig. 27), probably as a consequence of small, expansion-related fractures. In the intervals where density is reduced by expansion, a high-frequency variation is superimposed on the records, but the overall character of the profiles remains the same. The pattern that is displayed in the profiles is a cyclic variation with cycles on the order of 5-m thick. This pattern is similar to that of GRAPE records at Sites 721 and 722, except that cycles of density variation at those sites are 1–2 m thick.

We obtained *P*-wave logs only for Cores 117-723A-1H through -3H (0–27.1 mbsf) and Cores 117-723B-1H through -4H (0–33.3 mbsf); these data are presented in Figure 28. Below these intervals, *P*-wave transmission through the cores was inhibited by the lack of coupling of the sediment and the core liner. The *P*-wave velocity is positively correlated to the density determined by the GRAPE, and the logs display a pattern of cyclic variation similar to that of the GRAPE data. The velocity determined by the *P*-wave logger ranges from 1535 to 1620 m/s. This range is comparable with velocities determined for sediments of equivalent depth at Owen Ridge, Sites 721 and 722.

Vane Shear Strength

The extreme sediment disturbance caused by expansion of gas during recovery rendered most of the sediments from Site 723 unsuitable for vane shear strength measurements. Six measurements were made in Cores 117-723A-1H through -9H (Table 9). No correlation is seen between sub-bottom depth and increasing shear strength, perhaps due to the gas-induced sediment disturbance.

In Hole 723B one vane measurement was taken in each of Cores 117-723B-1H through -6H (Table 9). Shear-strength values increased from 7.1 kPa in Core 117-723B-1H (3.60 mbsf) to 45.4 kPa in Core 117-723B-6H (50.90 mbsf).

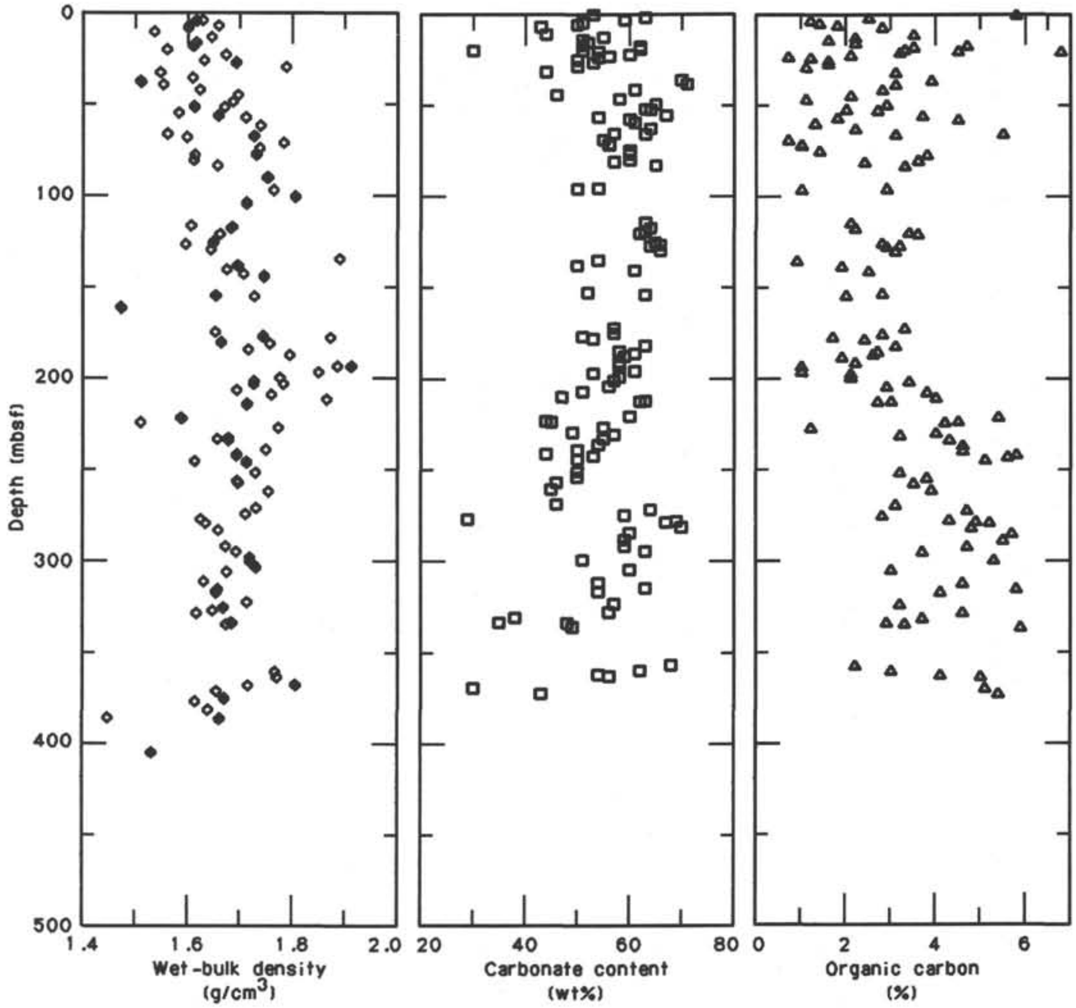

Figure 26. Wet-bulk density for Holes 723A (open symbols) and 723B (solid symbols), and calcium carbonate and organic carbon percentages for Hole 723A. All measurements were made on discrete samples.

SEISMIC STRATIGRAPHY

General Setting

Site 723 is located in the western slope basin of the Oman margin. This slope basin is not a basin from the standpoint of submarine topography, however. The continental slope dips seaward at an angle of 1°–2° throughout, and slopes are much steeper on the eastern flanks of the two basement highs that confine the slope basin (Fig. 29).

A seismic dip section across the slope basin shows a synclinal morphology of seismic horizons. This morphology arises from two sources: (1) normal faulting at boundary faults that separate the slope basin from the adjacent basement highs, and (2) a greater thickness of the seismic units in the center of the basin, with an onlap of seismic horizons toward both basement highs.

Based on lateral variations in traveltime between reflector pairs, the highest sedimentation rates have occurred very near the central axis of the slope basin down to at least 1 s sub-bottom traveltime, the limit of our seismic penetration.

As seen on a dip line, Site 723 is located on the central axis of the slope basin (Fig. 29). This location implies that the site has sampled the most continuous and highest sedimentation rates within the portion of the basin traversed by the dip line. On a strike line (Fig. 30), the site is also near the portion with the highest sedimentation rates; the visible section of the sub-basin thins substantially toward the northeast. Three other sites are located in the slope basin. Site 724 also is located along the central axis of the sub-basin, far to the northeast where average accumulation rates are about half those at Site 723. Site 725 is located near Site 724 but on the northwest flank of the sub-basin. Site 727 is located near the central axis of the sub-basin to the southwest of Site 723, where sedimentation rates are about 50% of those at Site 723.

Relative to the flanking basement highs, the western basin has been rapidly subsiding since at least 2 Ma. Sedimentation probably has kept up with subsidence and to some extent has isostatically driven this subsidence, so that the graben structure has maintained a seaward slope of the seafloor and has seldom, if ever, been topographically a basin during the last 2 m.y. This conclusion is based largely on the fact that seismic sequences thin but continue over the southeastern basement high. Some sudden truncation of reflectors against this basement high is possible, which would indicate that basement was occasionally a topographic high; however, such truncation, if present, is below the resolution of our seismic data.

If the southeast ridge was a topographic high for a significant period of time, then the location of thickest sediment accumulation might be expected to be near the ridge, at the downslope edge of the sub-basin. Instead, the currently deepest portion of each visible horizon deeper than the Site 723 penetration is immediately below Site 723. In contrast, from the base of Site 723 up to the seafloor, the axis of the depositional syncline mi-

Table 9. Physical properties summary for Holes 723A and 723B.

Core, sample, interval (cm)	Depth (mbsf)	Wet-bulk density (g/cm^3)	Porosity (%)	Water content (%)	Grain density (g/cm^3)	Dry-bulk density (g/cm^3)	Velocity (m/s)	Vane shear strength (kPa)
117-723-								
1H-1, 50-52	0.50	1.233	82.7	68.7	1.858	0.386		
1H-3, 50-52	3.50	1.628	66.8	42.0	2.568	0.944		
1H-5, 50-52	6.50	1.659	58.4	36.1	2.403	1.060		
1H-6, 5-7	7.55							15.2
2H-2, 50-52	9.80	1.536	70.0	46.7	2.353	0.819		
2H-4, 50-52	12.80	1.646	64.8	40.4	2.520	0.982		
2H-6, 50-52	15.80	1.616	63.0	39.9	2.436	0.971		
2H-7, 33-35	17.13							46.1
3H-2, 50-52	19.50	1.560	67.1	44.0	2.501	0.873		
3H-4, 50-52	22.50	1.673	60.2	36.9	2.529	1.056		
3H-6, 50-52	25.50	1.631	60.0	37.7	2.446	1.016		
3H-7, 15-17	26.65							21.9
4H-2, 50-52	29.10	1.788	56.6	32.4	2.648	1.208		
4H-4, 50-52	32.10	1.547	69.4	46.0	2.530	0.836		
4H-6, 50-52	35.10	1.609	65.3	41.5	2.504	0.941		
5H-2, 50-52	38.80	1.553	64.4	42.5	2.303	0.893		
5H-4, 50-52	41.80	1.623	66.2	41.8	2.495	0.945		
5H-6, 50-52	44.80	1.696	58.9	35.6	2.442	1.092		
6H-2, 50-52	48.40	1.686	60.3	36.6	2.536	1.069		
6H-4, 50-52	51.40	1.670	59.8	36.7	2.490	1.057		
6H-6, 50-52	54.40	1.582	65.4	42.4	2.418	0.912		
7H-2, 45-47	56.96	1.711	59.3	35.5	2.545	1.104		
7H-5, 50-52	61.51	1.739	56.8	33.5	2.565	1.157		
7H-8, 52-54	66.03	1.561	65.3	42.8	2.373	0.893		30.4
8H-2, 50-52	67.80	1.598	62.8	40.2	2.429	0.955		
8H-4, 50-52	70.80	1.783	56.3	32.3	2.640	1.207		
8H-6, 50-52	73.80	1.737	58.4	34.4	2.588	1.139		22.8
9H-2, 50-52	77.40	1.613	63.4	40.3	2.432	0.963		
9H-4, 50-52	80.40	1.611	60.3	38.4	2.425	0.993		
9H-6, 50-52	83.40	1.657	59.1	36.6	2.466	1.051		40.4
11X-2, 50-52	96.80	1.764	53.5	31.1	2.504	1.215		
13X-2, 50-52	116.10	1.606	63.0	40.2	2.509	0.960		
13X-5, 50-52	120.60	1.662	61.5	37.9	2.543	1.032		
14X-2, 91-93	126.21	1.596	64.9	41.7	2.558	0.930		
14X-4, 90-92	129.20	1.645	61.9	38.5	2.563	1.011		
15X-1, 88-90	134.28	1.891	49.2	26.7	2.597	1.386		
15X-5, 80-82	140.20	1.675	59.9	36.6	2.523	1.062		
15X-7, 28-30	142.68	1.707	59.5	35.7	2.590	1.097		
17X-2, 60-62	154.90	1.728	56.8	33.7	2.544	1.145		
19X-2, 78-80	174.38	1.653	59.4	36.8	2.426	1.045		
19X-4, 90-92	177.50	1.873	49.0	26.8	2.509	1.371		
19X-6, 127-129	180.87	1.757	58.2	34.0	2.642	1.160		
20X-2, 80-82	184.10	1.716	58.2	34.7	2.516	1.120		
20X-4, 80-82	187.10	1.795	56.6	32.3	2.633	1.214		
21X-2, 30-32	193.20	1.886	51.2	27.8	2.689	1.362		
21X-4, 65-67	196.55	1.850	58.7	32.5	2.548	1.249		
21X-6, 60-62	199.50	1.776	55.5	32.0	2.597	1.208		
22X-2, 20-22	202.80	1.783	55.0	31.6	2.615	1.219		
22X-4, 59-61	206.19	1.694	57.8	35.0	2.475	1.101		
22X-6, 16-18	208.76	1.760	57.9	33.7	2.599	1.167		
23X-3, 8					2.552			
23X-1, 50-52	211.30	1.866	69.5	38.2	2.488	1.154		
24X-1, 82-84	221.22	1.587	61.3	39.6	2.313	0.958		
24X-3, 37-39	223.77	1.510	67.2	45.6	2.342	0.822		
24X-5, 32-34	226.72	1.773	54.8	31.7	2.500	1.212		
25X-2, 127-129	232.87	1.657	59.3	36.6	2.341	1.050		
25X-6, 120-122	238.80	1.749	56.6	33.1	2.501	1.169		
26X-4, 97-99	245.27	1.613	60.1	38.2	2.349	0.997		
27X-2, 65-67	251.55	1.730	53.8	31.9	2.437	1.179		
27X-5, 67-69	256.07	1.695	56.9	34.4	2.407	1.112		
27X-6, 11-13	257.01	1.697	56.7	34.2	2.422	1.117		
28X-2, 124-126	261.84	1.755	55.7	32.5	2.479	1.185		
29X-2, 68-70	270.88	1.731	53.5	31.7	2.487	1.183		
29X-4, 98-100	274.18	1.711	56.8	34.0	2.521	1.129		
29X-6, 94-96	277.14	1.625	60.2	38.0	2.340	1.007		
30X-1, 91-93	279.21	1.635	63.4	39.8	2.508	0.985		
30X-4, 24-26	283.04	1.659	59.0	36.4	2.285	1.055		
31X-3, 94-96	291.84	1.673	58.8	36.0	2.481	1.071		
31X-5, 95-97	294.85	1.693	56.2	34.0	2.432	1.117		
31X, CC, 56-58	297.90	1.719	54.5	32.5	2.344	1.161		
32X-2, 98-100	299.98	1.719	56.6	33.7	2.441	1.139		
32X-4, 78-80	302.78	1.729	56.0	33.2	2.466	1.155		
32X-6, 78-80	305.78	1.675	55.6	34.0	2.329	1.105		
33X-3, 91-93	311.01	1.631	58.9	37.0	2.335	1.027		
33X-6, 64-66	315.24	1.658	57.0	35.2	2.367	1.073		
35X-1, 75-77	322.25	1.714	59.7	35.7	2.551	1.102		

Table 9 (continued).

Core, sample, interval (cm)	Depth (mbsf)	Wet-bulk density (g/cm^3)	Porosity (%)	Water content (%)	Grain density (g/cm^3)	Dry-bulk density (g/cm^3)	Velocity (m/s)	Vane shear strength (kPa)
117-723- (Cont.)								
35X-4, 72–74	326.72	1.648	59.3	36.9	2.416	1.040		
36X-2, 60–62	328.19	1.617	61.7	39.1	2.379	0.986		
36X-6, 69–71	334.28	1.674	60.9	37.3	2.459	1.050		
37X-1, 116–118	336.96	1.536	65.5	43.7	2.392	0.866		
39X-4, 75–77	360.25	1.767	55.7	32.3	2.545	1.197		
39X-6, 73–75	363.23	1.770	54.0	31.3	2.503	1.217		
40X-3, 4–6	367.74	1.715	55.1	32.9	2.434	1.150		
40X-5, 20–22	370.90	1.655	56.3	34.9	2.394	1.078		
41X-2, 76–78	376.56	1.614	58.7	37.3	2.369	1.013		
41X-5, 86–88	381.16	1.639	58.8	36.8	2.325	1.036		
42X-2, 3–5	385.53	1.448	68.9	48.8	2.263	0.742		
45X, CC, 10–12	413.10	2.766					[a]5383	
45X, CC, 10–12	413.10						[b]5560	
117-723B-								
1H-3, 60–62	3.60	1.616	64.5	40.9	2.537	0.956		7.1
2H-3, 50–52	7.80	1.601	63.5	40.6	2.434	0.950		18.2
3H-3, 60–62	17.60	1.611	66.2	42.1	2.582	0.932		20.0
4H-3, 50–52	27.10	1.692	59.3	35.9	2.485	1.085		18.5
5H-3, 60–62	36.90	1.509	68.5	46.5	2.340	0.807		25.4
6H-6, 50–52	50.90	1.612	63.5	40.4	2.442	0.961		45.4
7H-3, 50–52	56.10	1.658	60.3	37.2	2.469	1.041		
8H-4, 60–62	67.40	1.726	61.0	36.2	2.567	1.100		
9H-4, 50–52	76.90	1.731	62.2	36.8	2.566	1.094		
10X-6, 80–82	89.90	1.751	59.2	34.6	2.587	1.145		
11X-7, 30–32	100.50	1.805	56.4	32.0	2.590	1.228		
12X-3, 50–52	103.64	1.712	62.9	37.7	2.614	1.067		
13X-5, 60–62	116.90	1.685	62.3	37.9	2.568	1.046		
14X-4, 50–52	124.90	1.650	62.9	39.1	2.506	1.006		
15X-6, 90–92	138.00	1.697	60.0	36.2	2.492	1.083		
16X-3, 141–143	143.61	1.746	55.8	32.7	2.470	1.175		
17X-4, 100–102	154.40	1.654	61.3	37.9	2.438	1.026		
18X-2, 132–134	161.42	1.474	69.0	48.0	2.267	0.767		
19X-6, 134–136	177.04	1.744	57.8	33.9	2.546	1.152		
20X-2, 88–90	180.28	1.664	60.6	37.3	2.526	1.042		
21X-4, 137–139	193.47	1.912	48.3	25.9	2.670	1.417		
22X-4, 112–114	202.92	1.726	56.6	33.6	2.485	1.146		
23X-5, 123–125	214.13	1.713	58.4	34.9	2.545	1.115		
24X-4, 55–57	221.55	1.589	61.6	39.7	2.336	0.958		
25X-5, 133–135	233.53	1.678	58.7	35.8	2.421	1.077		
26X-4, 106–108	241.46	1.694	58.7	35.5	2.445	1.092		
27X-1, 50–52	246.10	1.712	59.2	35.4	2.459	1.106		
27X, CC, 16–18	247.16	2.771					[a]5131	
27X, CC, 16–18	247.16						[b]5541	
31X-6, 73–75	301.93	1.727	56.7	33.6	2.465	1.147		
33X-3, 22–24	316.22	1.655	62.6	38.8	2.512	1.014		
33X, CC, 28–30	317.10	2.712					[a]4650	
33X, CC, 28–30	317.10						[b]5285	
35X-2, 92–94	325.12	1.669	62.2	38.1	2.598	1.033		
36X-1, 76–78	333.26	1.683	60.3	36.7	2.419	1.066		
39X-5, 2–4	367.62	1.806	56.1	31.8	2.641	1.232		
40X-3, 80–82	375.10	1.670	58.9	36.1	2.396	1.067		
40X, CC, 31–33	376.79	2.726					[a]4467	
40X, CC, 31–33	376.79						[b]4944	
41X-4, 67–69	386.17	1.661	58.6	36.2	2.443	1.061		
42X-3, 115–117	404.45	1.531	63.2	42.3	2.196	0.883		

[a] Velocity measurement perpendicular to bedding.
[b] Velocity measurement parallel to bedding.

grates to a position about halfway between the site and the southeast basement high. This migration does not imply any change in the subsidence pattern. If future deposition continues to be highest in the center of the basin, the associated differential subsidence will cause the axis of the present upper portion of the syncline to migrate to the center of the basin, to a position concordant with the maximum sedimentation rate. From the seismic section across Site 723, we can infer only relative subsidence within the basin and with respect to flanking basement highs. We can draw no conclusions concerning the amount of absolute subsidence of the entire region.

On the seismic lines crossing Site 723 (Figs. 29 and 30), we can see that the sediment section is almost devoid of faults, except for the major normal faults on the flanks. These two faults are not imaged well on the unmigrated sections. A single small-offset reverse fault may be present just below Site 723. The reversed nature of this possible fault does not require horizontal compression; indeed, a strong dominance of horizontal extension is implied by the thinning of both faulted and overlying seismic sequences away from the axis of the depositional syncline. Instead, the reversed fault is probably caused by slight differential subsidence of the northwestern portion of the basin.

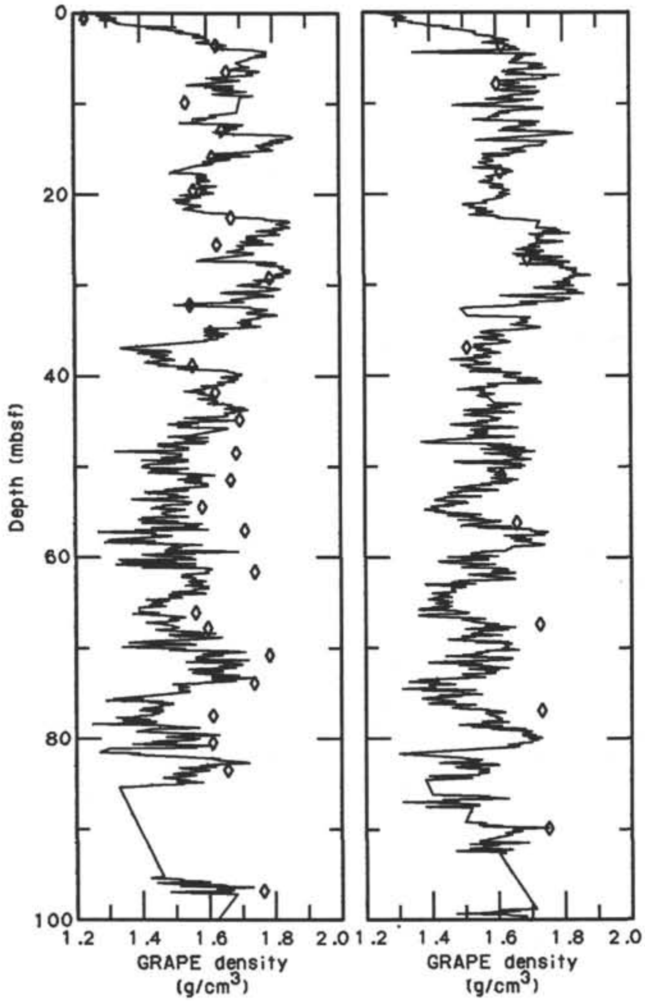

Figure 27. GRAPE wet-bulk density (solid line) and wet-bulk density from discrete samples (diamonds) for Holes 723A and 723B. GRAPE profile is based on 10-cm-block averages of the data.

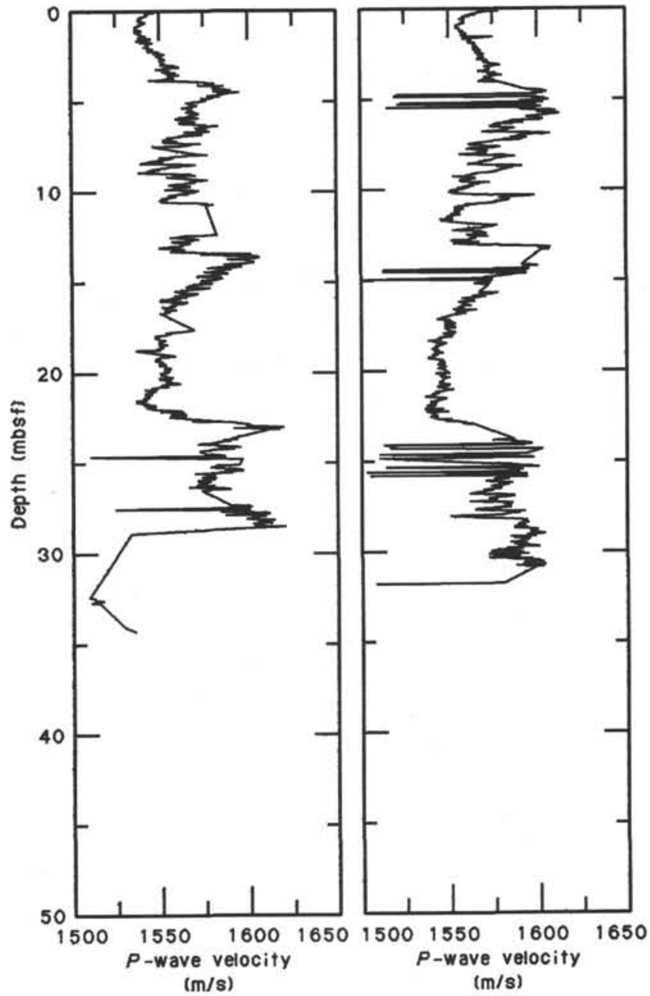

Figure 28. Compressional-wave velocity as measured by the *P*-wave logger in Cores 117-723A-1H to -3H and Cores 117-723B-1H to -4H.

The reversed fault dies out upsection just below the deepest portion of Site 723; it was active, therefore, ~2.5 Ma. This fault is a possible conduit for the advecting fluids hypothesized on the basis of pore fluid geochemistry, hydrocarbon type, and downhole logging (see "Inorganic Geochemistry," "Organic Geochemistry," and "Downhole Measurements" sections, this chapter). However, the offset on this suspected fault is too small for confirmation of the fault's existence.

Relation of Seismic Traveltime to Core Depth

Both sonic velocity and density logs were obtained for Site 723. Reliable velocity log data extend from 97.5 to 413.8 mbsf; reliable density log data extend from 88.4 to 425.5 mbsf. We estimated sonic velocities for 413.8 to 424.4 mbsf, based on resistivity for this depth interval and a regression of sonic traveltime on resistivity ($r = -0.677$) from the overlying interval (372.0–413.8 mbsf).

Continuous sonic and density logs for the interval from 97.5 to 424.4 mbsf were used to calculate a synthetic seismogram for Site 723. A convolutional model with interbed multiples was used. The wavelet was estimated from *Conrad* profiles from the same site survey cruise as the profiles of Figures 29 and 30 (see "Site 720" chapter, this volume). A synthetic seismogram calculated with the sonic log and a constant-density assumption was almost identical to the one based on both sonic and density logs. No reliable velocity information is available from the top 88.4 m of Site 723. Thus, when comparing the synthetic seismogram to the seismic section, the starting time of the synthetic must be based on character correlation between seismic and synthetic.

Figure 31 compares the synthetic seismogram from Site 723 with a single expanded seismic trace and the portion of Figure 29 approaching the site. The single seismic trace is a 10-trace mix centered at the site. The single trace and seismic section are from the same *Conrad* seismic line. The single trace is more useful for a direct comparison to the synthetic seismogram because it includes both peaks and troughs. The adjacent seismic section provides complementary information concerning lateral variability of reflector strength. The amplitudes of the synthetic seismogram and seismic trace are individually scaled to the largest peak or trough. Thus, the much lower plot amplitudes in the correlated portion of the seismic section compared with the synthetic seismogram are not significant. This difference arises simply from the fact that only the seismic trace encompasses the very high-amplitude seafloor return. Relative amplitudes and character within each trace are unaffected by the scaling.

Pronounced spikes are evident on the relative impedance log of Figure 31. These spikes are much more obvious on the sonic and density logs (see below) because the latter logs are closely sampled at 0.15-m depth increments, while the impedance log is an integrated record more coarsely sampled at a 0.002-s incre-

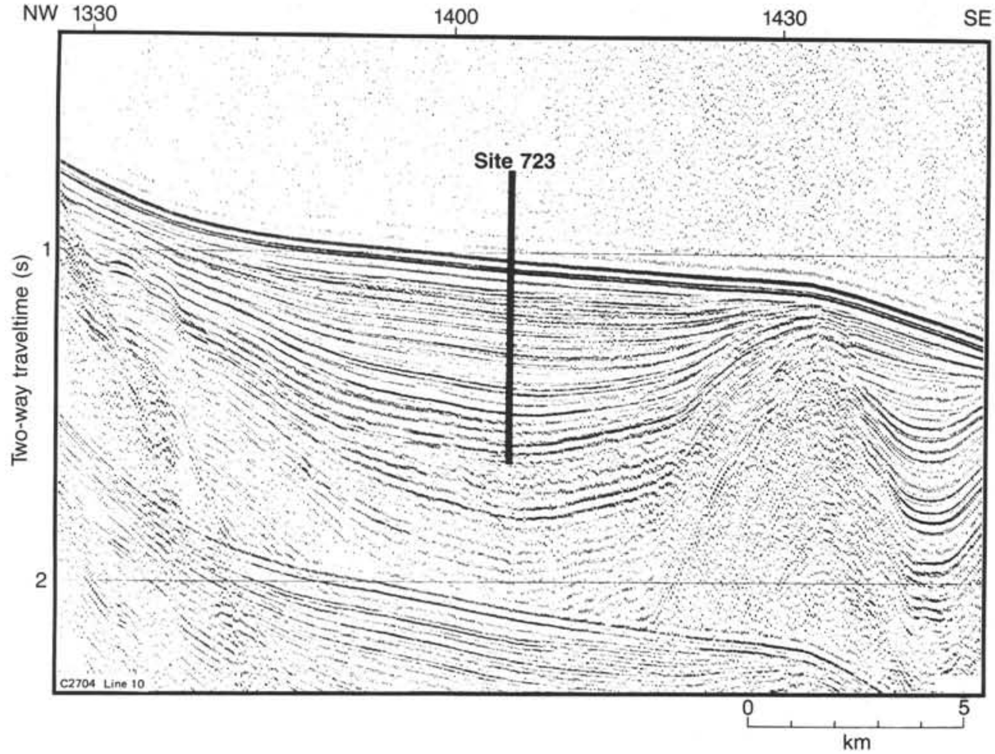

Figure 29. Seismic line 10 of site survey cruise RC2704, showing a dip section across Site 723 (Mountain and Prell, this volume).

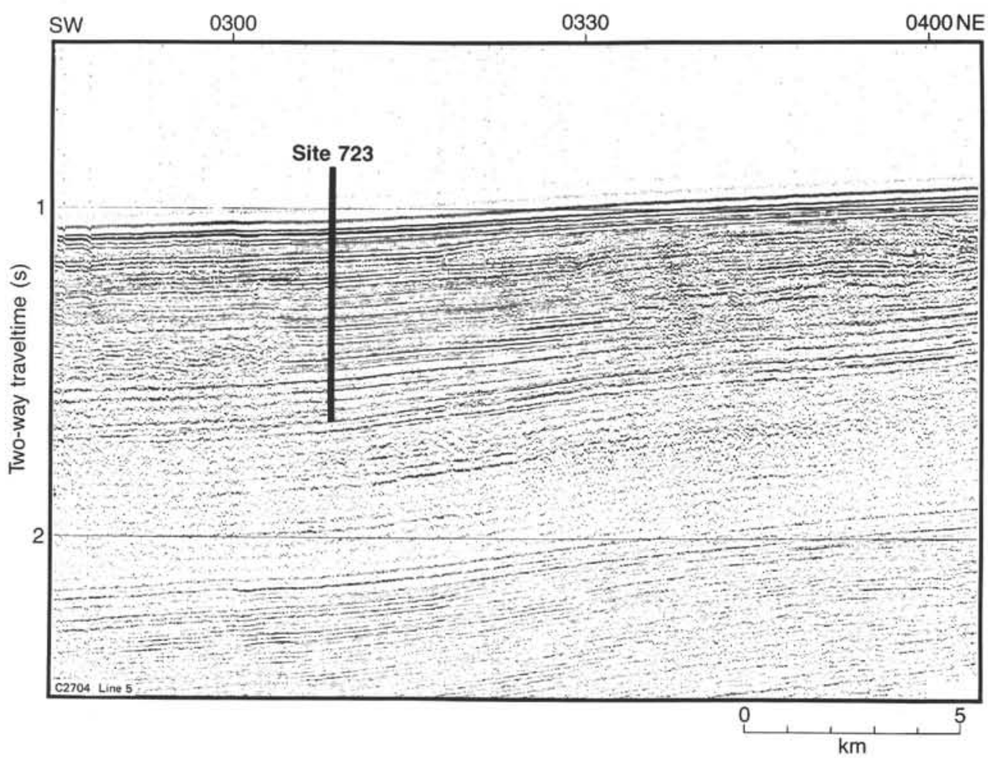

Figure 30. Seismic line 5 of *Robert Conrad* site survey cruise RC2704, showing a strike section across Site 723.

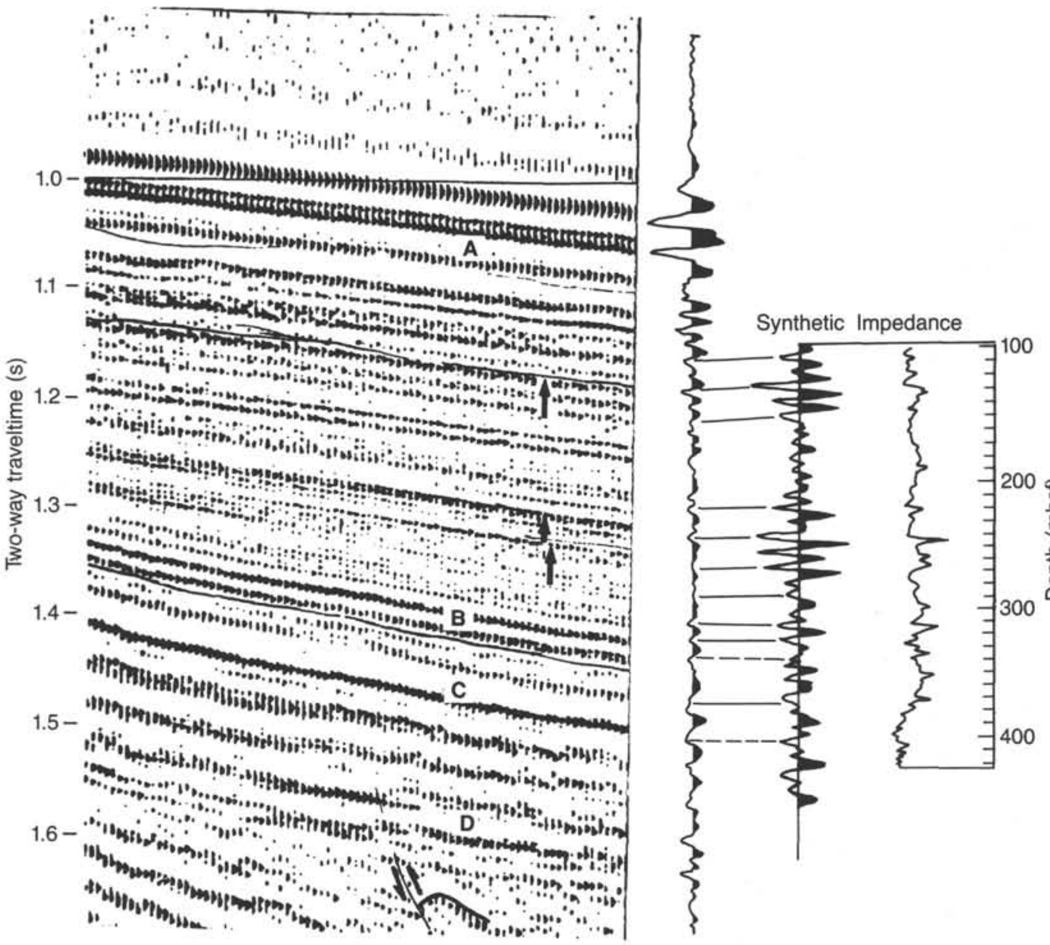

Figure 31. Synthetic seismogram for Site 723, based on sonic and density logs, and correlated with both the seismic trace nearest the site and seismic line 10. The vertical axis of all three is two-way traveltime; a depth scale for the site is shown at right.

ment. These thin spikes are 0.5–2.0-m-thick dolomite beds, with a much higher velocity and density than the surrounding sediments. The thinnest beds are invisible to seismic, because reflection coefficients at the top and bottom of each bed are nearly identical but opposite in sign, and the seismic traveltime between the two reflection coefficients is extremely short in comparison to the frequency of the wavelet.

Only the dolomite bed at 244 mbsf obviously produces a substantial seismic reflector, and this reflector is created as much by the possibly spurious 7-m-thick zone of increasing velocities toward the dolomite bed (Fig. 48) as by the dolomite bed itself. The correlative portion of the seismic trace has much lower relative amplitudes than does the synthetic, indicating that the 244-mbsf dolomite horizon is undetected or only faintly detected by the seismic line.

This difference probably has two causes:

1. The existence of a seismic Fresnel zone is not modeled in a 1-D synthetic seismogram, so the actual vertical resolution of seismic data is slightly lower than implied by a 1-D synthetic.
2. The dolomite beds may lack lateral continuity, based on their inconsistent detection in the A and B holes and on the lack of evidence for permeability barriers to compaction (see "Lithostratigraphy" and "Downhole Measurements" sections, this chapter).

With the exception of the 244-mbsf "reflector," a reasonably good character match exists between the synthetic seismogram and seismic trace.

Only in the bottom-most portion of the synthetic seismogram is the correlation with seismic tenuous. For most of the interval from 97.5 to 390 mbsf, core depths can be matched to seismic traveltime with moderate confidence.

The most distinctive seismic reflector peaks at Site 723 are at 1.18 s (122 mbsf), 1.42–1.43 s (312–330 mbsf), and 1.49 s (382 mbsf). The doublet of peaks at 1.42–1.43 s corresponds to the base of a laminated unit and to the top of a unit rich in siliceous material. This horizon can be traced to the northwest on Figure 29 and identified as approximately the first horizon deposited after abandonment of a small feeder channel once active at the base of the northwest basement high. The channel probably carried sediments from the shallower northeast part of the subbasin down along the base of the basement high. The peak at 1.18 s results from a porosity decrease and is not clearly related to any lithologic change. The peak at 1.49 s, along with the trough just above it, is associated with a zone from 352 to 395 mbsf of rapidly increasing porosity downhole, due to a high organic content and, in particular, to a high siliceous content.

The traveltime/depth relationship of Figure 31 is shown in crossplot form in Figure 32. Also shown is a similarly determined time/depth curve for Site 728, the only other Oman mar-

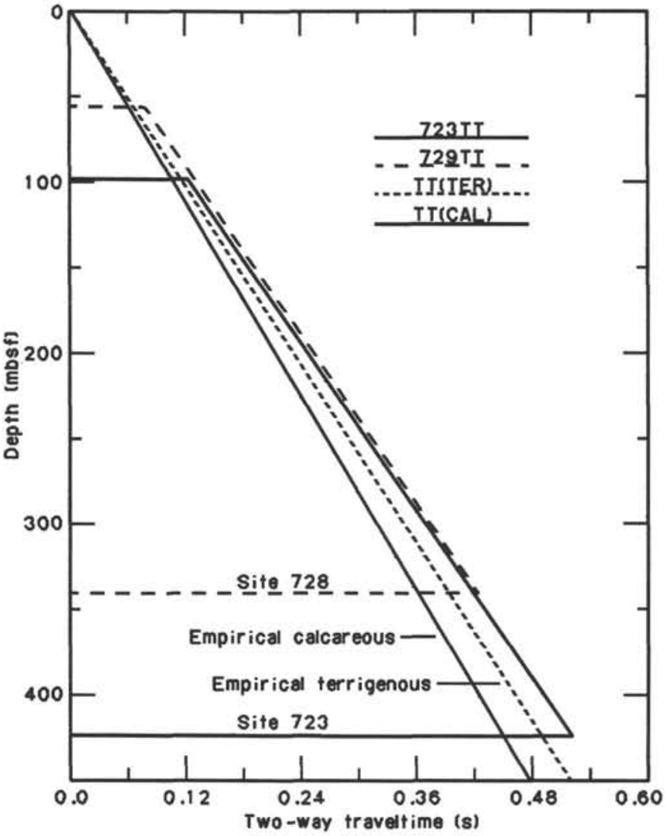

Figure 32. Four plots of two-way traveltime as a function of sub-bottom depth, based on the following velocity/depth functions: Site 723 sonic log, Site 728 sonic log, empirical relation for terrigenous sediments (Hamilton, 1979), and empirical relation for calcareous sediments (Hamilton, 1979).

gin site that was logged. The two curves are almost identical, and both indicate significantly slower velocities than the empirical trends for terrigenous and calcareous sediments of Hamilton (1979). However, some caution is needed when applying the Site 723 and 728 curves to other Oman margin sites. The Site 723 curve is slowed substantially with respect to empirical trends by the very high organic matter throughout the site, higher than at any of the other Oman margin sites. In contrast, the Site 728 curve is slowed by the presence of half as much organic matter as at Site 723, plus a substantial siliceous component below 85 mbsf. Thus, varying amounts of organic and siliceous matter at other sites would cause departures from the curves for Sites 723 and 728.

INORGANIC GEOCHEMISTRY

Introduction

At Site 723, we collected 33 interstitial water samples from Holes 723A and 723C, 30 by squeezing and 3 with the Barnes *in-situ* water sampler. All analytical results are listed in Tables 10 and 11 and presented in Figures 33 through 36.

Salinity, Chloride, and pH

The concentration profiles of salinity, chloride, and pH are shown in Figure 33. As at previous sites, the ~2‰ decrease in salinity over the top 60 m can be attributed mainly to the loss of sulfate and magnesium from solution. Salinities near 36‰ in the lowermost 100 m of the hole reflect the progressive addition of alkalinity to pore waters at depth.

One important feature of the chloride distribution at this site is the 30–40 mmol/L decrease in concentration between surface sediments and the bottom of the hole (Fig. 33). The profile suggests that dilution of the pore waters by the upward diffusion and/or advection of fresher water may be occurring.

The pH data listed in Table 10 and the profile in Figure 33 should be regarded with caution because a very strong upward drift of successive pH measurements made on the same sample was observed, especially in those waters with very high alkalinities. The drift was attributed to degassing of high concentrations of dissolved CO_2 in the laboratory.

Sulfate and Alkalinity

Sulfate depletion is pronounced at Site 723, with a gradient of ~0.5 mmol/L/m over the top 45 m in both Holes 723A and 723C. The high-resolution profile shown in Figure 34 indicates that the sulfate concentration falls to zero near 44 mbsf. Significant concentrations of sulfate up to 2.2 mmol/L were measured in the lower 200 m of Hole 723A (Fig. 33); the gradual increase with depth between 240 and 400 mbsf suggests that sulfate is diffusing upward from a source below the base of the cored sequence. Reduction of the upward-diffusing sulfate may be occurring at almost any depth between 200 and 400 mbsf. It is not possible given the available resolution to pinpoint more precisely the zone or zones of reaction in the lower half of the hole.

The titration alkalinities measured in Hole 723A (Table 10 and Figs. 33 and 34) are among the highest ever recorded during the history of ODP/DSDP, exceeding 100 mmol/L near the bottom of the hole. Higher concentrations have been measured previously only on the Peru margin during Leg 112. Because the reduction of the total sulfate inventory of buried seawater could produce a maximum of roughly 60 mmol/L of alkalinity, the higher levels below ~100 m depth must reflect contributions from other sources.

One source for the "excess" alkalinity must be the generation of ammonia via methane-producing fermentation reactions, which increases titration alkalinity by producing hydroxyl in the reaction $NH_3 + H_2O = NH_4^+ + OH^-$. In Hole 723A, ammonium concentrations increase with depth by about 20 mmol/L in the zone between ~60 and 200 m depth (Table 10 and Fig. 33) where no sulfate is present. This distribution probably reflects production of ammonia during methanogenesis. Between ~185 and 385 mbsf alkalinity increases by ~20 mmol/L (Table 10) while ammonia increases by only about 3 mmol/L. Presumably, the difference is due to the reduction of sulfate, which is diffusing upward from a deep-seated source and continuing to produce alkalinity, in this case largely as bicarbonate, below a depth of ~200 m. In addition, upward diffusion of bicarbonate could contribute to the observed distribution of alkalinity in the lowermost 200 m of the hole.

Such phenomena were observed on the Peru margin during Leg 112, where both chloride and sulfate profiles indicated that upward-diffusing brines were supplying sulfate to zones of reduction at depth in a number of holes (Suess, von Huene et al., 1988). A major difference between the Peru margin model and our observations here, however, is that the chloride concentration at Site 723 *decreases* with depth. We suggest that the only mechanism which can explain the observed trio of distributions (the chloride decrease and the alkalinity and sulfate increases with depth) is diffusion related to an underlying fluid which is sulfate enriched and chloride depleted. Such a fluid could be produced by the percolation of relatively fresh groundwater through gypsum or anhydrite beds. However, the location of such deposits is unknown.

If such a mechanism was active, one would expect calcium, in addition to sulfate, to be added to the percolating water. A small increase in the calcium concentration with depth is observed in the lower 100 m of Hole 723A (Fig. 33), which tends to support our suggestion. Therefore, a plausible explanation for the unusual pore-water chemistry at this site is the presence of a fluid of rather unique composition in the sediments below 400 mbsf. This conclusion is supported by logging results (see "Downhole Measurements" section, this chapter).

Calcium and Magnesium

Dissolved calcium and magnesium profiles are shown in Figures 33 and 34. The concentrations of both ions decrease with depth, with the exception of the calcium addition to solution below ~300 mbsf that was discussed above. The depletion of both elements is more severe than has been observed at either Sites 722, 724, or 725, which is probably related to the extremely high alkalinity below a depth of only ~50 mbsf. Presumably, precipitation of calcite is responsible for the increase in the magnesium/calcium ratio in the top 15 m of Hole 723C (Fig. 34). Immediately below this level, the magnesium concentration decreases quite markedly to ~37 mmol/L at 40 mbsf.

The downward concavity of the detailed profile suggests that dolomite is currently forming within the sulfate reduction zone between 20 and 40 mbsf (Fig. 34), and smear slide observations indicate that euhedral dolomite rhombs of apparent authigenic origin are indeed present in small amounts throughout the cored sequence. The magnesium concentration continues to decrease to the bottom of the hole, apparently linearly, which suggests that the postulated fluid at greater depths is magnesium depleted. Thus, Mg^{2+} is diffusing steadily downward, evidently without involvement in diagenetic reactions between ~100 mbsf and the bottom of the hole.

Carbonate mineral layers occur at several horizons between 250 mbsf and the bottom of Hole 723A and are occasionally associated spatially with laminated sediments. The X-ray diffraction results (see "Sediment Mineralogy," below) indicated that these layers consist of nearly 100% dolomite. Five such layers were observed in the recovered sediments (see "Lithostratigraphy" section, this chapter); nine were noted in the logging records for the hole (see "Downhole Measurements" section, this chapter). Dolomite can precipitate via a number of reactions in continental margin sediments, including the following (Baker and Burns, 1985):

(1) $2CaCO_3 + Mg^{2+} = CaMg(CO_3)_2 + Ca^{2+}$ (replacement of aragonite or calcite);

(2) $Ca^{2+} + Mg^{2+} + 4HCO_3^- = CaMg(CO_3)_2 + 2CO_2 + 2H_2O$ (direct precipitation from solution); and

(3) $CaCO_3 + Mg^{2+} + 2HCO_3^- = CaMg(CO_3)_2 + CO_2 + H_2O$ (addition of magnesium without Ca^{2+} release).

The layers recovered at Site 723 range up to nearly a meter thick. One view on their significance, which was favored by the shipboard geochemists, is that the layers could not have formed at any significant depth because it is physically impossible for vertical diffusion to supply much magnesium (and/or calcium) to precipitation loci at depth in rapidly accumulating sediments. Therefore, the formation of the dolomite layers must have commenced when those horizons were nearer the sediment-water interface. Because reactions (2) and (3) above would be more likely to proceed when the bicarbonate concentration is high, a high organic carbon accumulation rate, which would lead to high alkalinity in interstitial waters, would facilitate dolomite formation. Reaction (1) would also proceed more readily in the sulphate reduction zone in carbon-rich sediments because high alkalinity will result first in the precipitation of $CaCO_3$ which will increase the Mg/Ca ratio, making subsequent formation of dolomite chemically more favorable.

A slowed rate of sedimentation will also permit more Mg^{2+} to diffuse to the precipitation site from overlying seawater. Therefore, we tentatively suggest that the dolomite layers at Site 723 represent periods of high organic matter input coincident with episodes of reduced sedimentation. Such an association has been proposed previously to explain the distribution of dolomite in Holocene sediments off Baja California (Shimmield and Price, 1984). The depositional conditions required to support such a model are met at times of maximum transgression of sea level and lead to the formation of condensed sections (Haq et al., 1987).

Ammonia, Phosphate, and Silica

The distribution of these metabolites is shown in Figures 33 and 34. Ammonia concentrations are very high below 30 mbsf at this site, which is due to two factors. First, the sedimentary organic matter content is very high, which leads to the relatively rapid depletion of sulfate over the top 40 m and methanogenesis below this level. Sulfate reduction probably replaces fermentation in the lower 100 m of the hole as the principal mechanism by which the degradation of organic matter proceeds. Both bacterially mediated processes produce ammonia from the nitrogenous fraction of organic matter; the abundance of organic nitrogen is reflected by the high interstitial ammonia concentrations.

The second factor which governs the level of dissolved ammonia is uptake of NH_4^+ by clay minerals. In many organic-rich sediments, the exchange of NH_4^+ for K^+ and Na^+ is of a magnitude comparable to the concentration of ammonia produced (see, e.g., Moore and Gieskes, 1980), and it is possible that such exchange is an important reaction at Site 723. If so, then in the discussion above, a larger proportion of the "excess" alkalinity at depth should be credited to the protonation of NH_3 and a smaller proportion to the generation of HCO_3^-.

Dissolved phosphate concentrations are much lower than expected given the high ammonia levels and can be explained by the precipitation of fluorapatite, which is common throughout the section (see "Sediment Mineralogy," below). The disagreement between the high-resolution phosphate profile obtained from Hole 723C (Fig. 34) with the Hole 723A results between about 20 and 70 m depth is an analytical artifact caused by interference of sulfide during the analysis of samples from the latter hole. Large quantities of a brown precipitate, believed to be antimonyl sulfide, formed in the reaction cuvettes upon the addition of the potassium antimonyl tartrate reagent during the colorimetric analysis. The resulting turbidity gave spuriously high absorbances. To avoid this problem in subsequent determinations (including measurements on samples from Hole 723C), we bubbled N_2 through the pore-water samples for ~1 hr prior to the addition of the colorimetric reagents. The additional step reduced the dissolved sulfide concentration to very low values and effectively eliminated the interference.

The dissolved silica profile (Figs. 33 and 34) is similar to that seen previously. Dissolution of opal yields concentrations which approach an asymptotic value of ~1000 μmol/L near 40 m depth; the rather shallow gradient (~20 μmol/L/m) indicates that the sediments at this site are not rich in opal. The increase to 1400 μmol/L near the bottom of the hole suggests that an opal-rich horizon may exist near 400 mbsf. This observation agrees with the logging results (see "Downhole Measurements" section, this chapter), which indicate the occurrence of a low-density, high-porosity band at a similar depth.

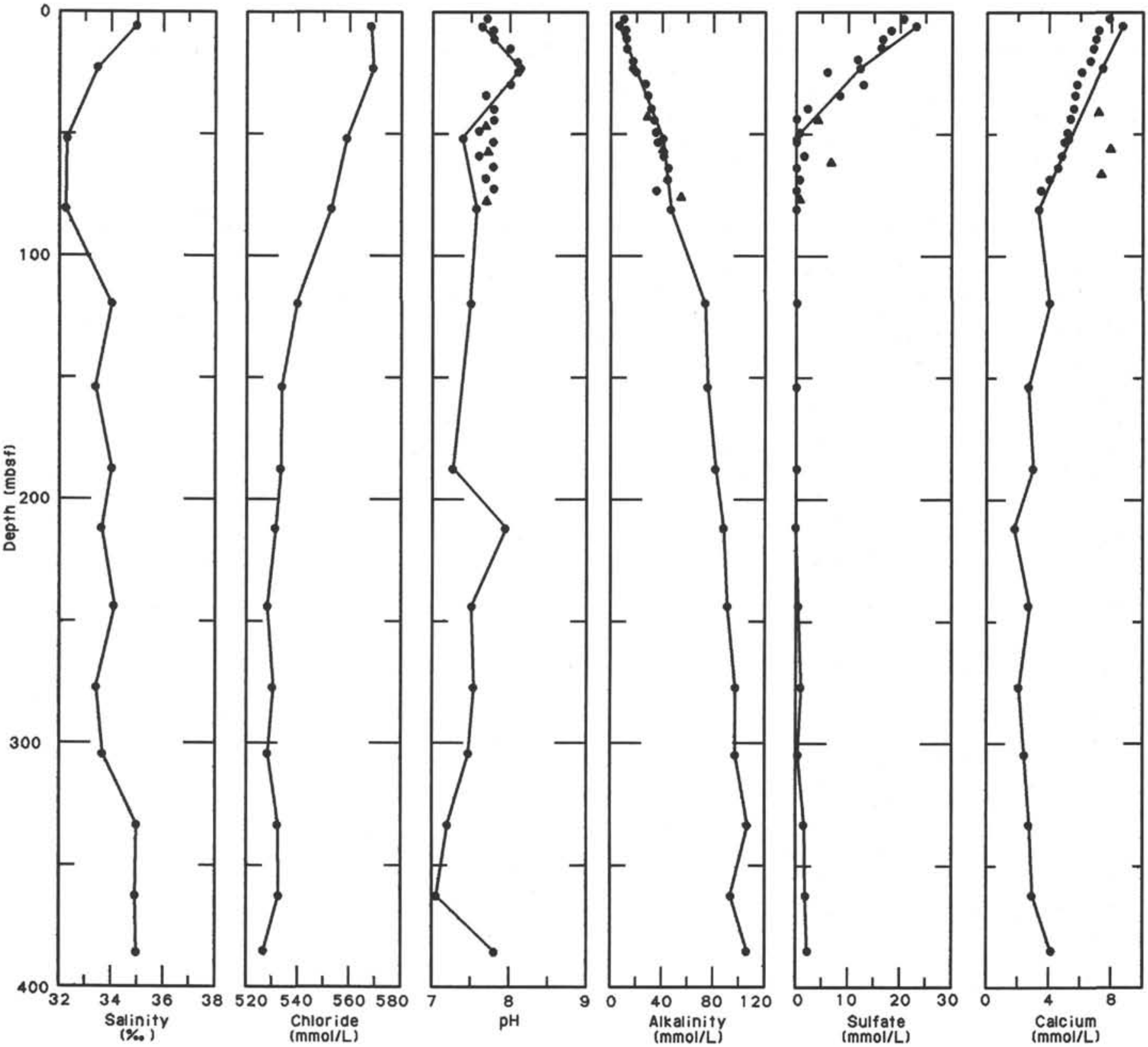

Figure 33. Concentrations vs. depth for Site 723. Dots = squeezed pore waters; triangles = *in-situ* pore-water samples obtained with the Barnes water sampler. The solid lines join data points from Hole 723A only. The other points represent measurements made on samples from Hole 723C.

Dissolved Organic Carbon

Relative concentrations of dissolved organic carbon (DOC) in the interstitial water samples were determined at this site by measuring the absorbance of the pore water at a wavelength of ~240 nm. The results are listed in Table 11 and plotted in Figures 35 and 36. Note that the data are given in absorbance units rather than as absolute values and are therefore useful only as a relative indication of DOC abundance. However, the measured absorbance is directly proportional to the DOC concentration (Krom, 1976).

In general, DOC at this site increases downhole to a maximum value at 385 mbsf which is about four times its concentration at shallow depths (Fig. 36). This profile reflects the general distribution of organic matter in the cored section (see "Organic Geochemistry" section, this chapter). The sharp increase in DOC at ~30 mbsf correlates well with inflections in the magnesium and alkalinity profiles and suggests that diagenetic activity is particularly pronounced at this depth. Such reactivity may be related to the local maximum in the organic carbon concentration evident between 25 and 35 mbsf (see "Organic Chemistry" section, this chapter).

In-Situ Samples

Three interstitial water samples were collected from Hole 723C using the Barnes downhole water sampler (DHWS). Analytical results are listed in Table 10 and are plotted as triangles on the previously discussed figures. With the exception of phosphate, the results are in reasonable agreement with the measurements made on the squeezed samples. The *in-situ* results for phosphate are highly variable and appear to be spurious; such variability is common for phosphate in *in-situ* samples and is thought to be due to contamination from the stainless steel coil in the Barnes sampler (R. Barnes, pers. comm.).

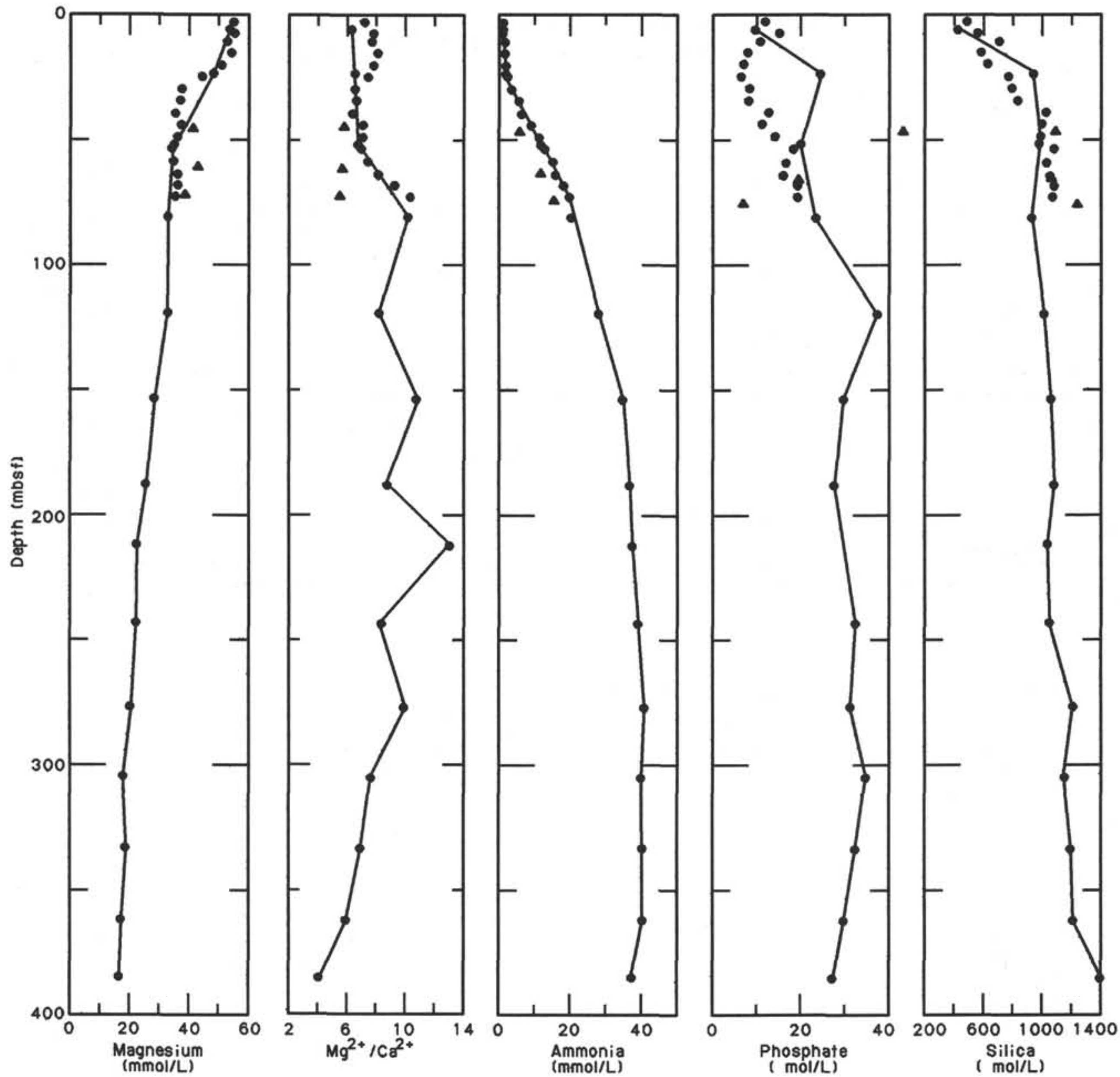

Figure 33 (continued).

Dissolved sulfate is higher than expected in the sample collected from Core 117-723C-8I (~66 mbsf), indicating some contamination with seawater. Concentrations of Ca^{2+} are also high compared with measurements made on squeezed samples from the same depths, suggesting that some $CaCO_3$ may have precipitated from the pore waters during core recovery. Based on the slight downward offset of the *in-situ* ammonia data, as compared with the regular sample (Fig. 33I; R. Barnes, pers. comm.), we believe that the *in-situ* samples may have been collected several meters higher than indicated by the driller.

Sediment Mineralogy

The mineralogy of 10 sediment residues from Hole 723A remaining after interstitial water extraction was determined by X-ray diffractometry. In all cases, $CaCO_3$ was removed with 10% HCl prior to analysis; the acid treatment was followed by two washes of the insoluble residue with deionized water. Diffractograms were also obtained for three additional samples thought to be apatite, aragonite, and dolomitic limestone, respectively. No glycolation was carried out at this site, but slow scans were made on three samples in an attempt to differentiate between overlapping pairs of clay mineral spectra.

The noncarbonate fraction of the sediments at Site 723 is composed largely of the same suite of minerals observed in the calcareous units on the Owen Ridge (Site 722). Quartz, feldspar, chlorite, and illite and/or mica are common to all samples. There appears to be no gross variation in the relative abundances of these minerals with depth throughout the Quaternary and late Pliocene, suggesting that source areas have not changed significantly during the last 2–3 m.y.

Pyrite occurs in significant quantities throughout the cored section at Site 723, in contrast to only traces observed in lithologic Units I, II, and III at Site 722. This difference can be attributed to the higher organic carbon content and concomitant severe sulfate depletion at Site 723.

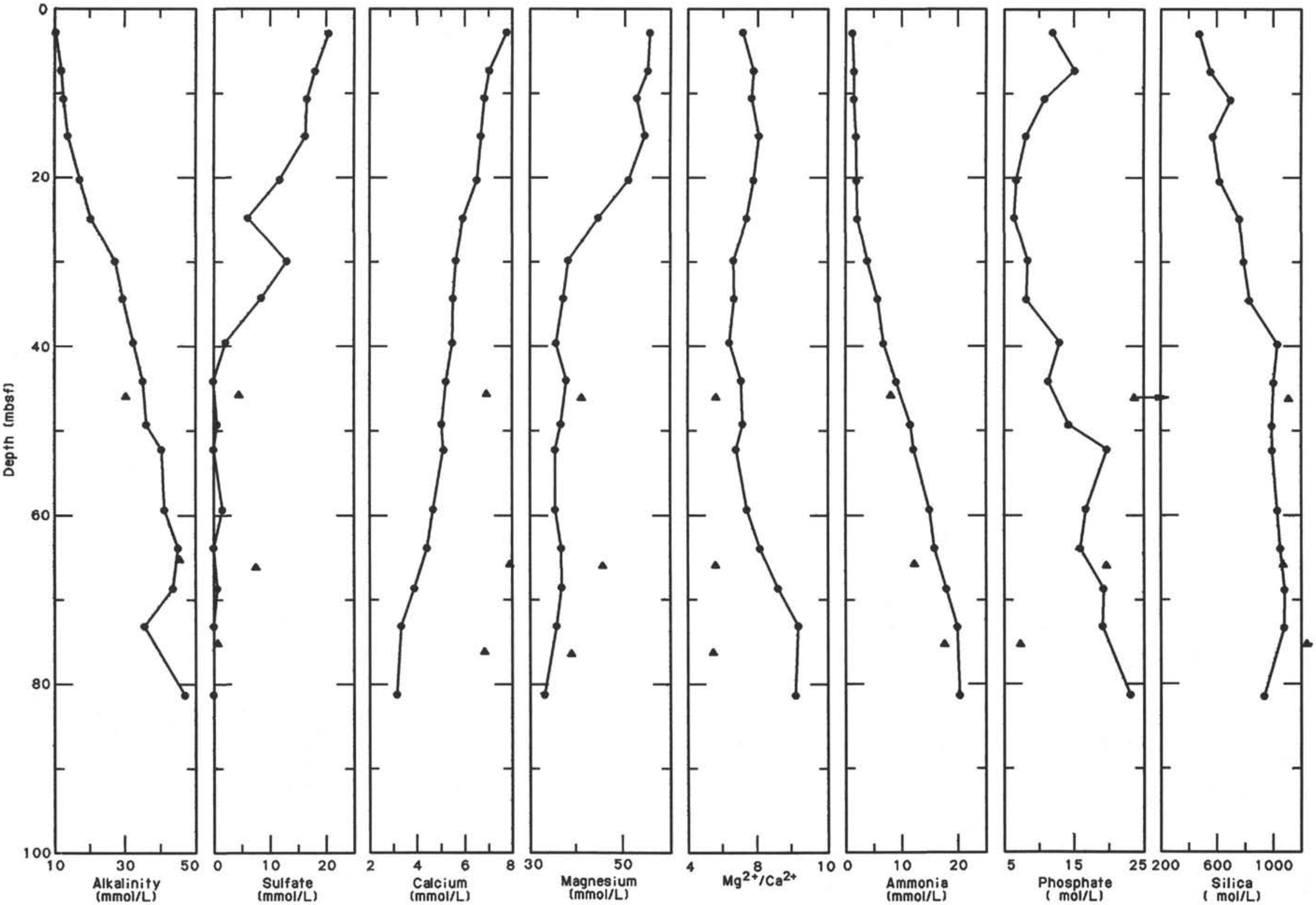

Figure 34. High-resolution profiles of samples from Hole 723C. Dots = squeezed pore waters; triangles = *in-situ* pore-water samples obtained with the Barnes downhole water sampler.

Table 10. Summary of interstitial water geochemical data for Holes 723A and 723C.

Core, sample, interval (cm)	Depth (mbsf)	Vol. (mL)	pH	Alk. (mmol/L)	Sal. (g/kg)	Mg (mmol/L)	Ca (mmol/L)	Cl (mmol/L)	SO_4 (mmol/L)	PO_4 (μmol/L)	NH_4 (mmol/L)	SiO_2 (μmol/L)	Mg/Ca
117-723C-1H-2, 145-150	2.95	59	7.70	10.45	—	55.66	7.77	—	20.6	12.0	1.20	477	7.16
117-723A-1H-4, 145-150	5.95	56	7.65	7.42	36.0	54.15	8.58	568	23.2	9.5	1.22	423	6.31
117-723C-1H-5, 145-150	7.45	57	7.80	12.04	—	55.09	7.07	—	18.1	15.2	1.40	562	7.79
117-723C-2H-2, 145-150	10.75	53	7.80	12.71	—	52.99	6.88	—	16.6	10.8	1.56	703	7.70
117-723C-2H-5, 145-150	15.25	58	8.00	13.99	—	54.69	6.76	—	16.3	8.1	1.81	580	8.09
117-723C-3H-2, 145-150	20.45	56	8.10	17.35	—	51.25	6.56	—	11.8	6.9	2.04	625	7.81
117-723A-3H-4, 145-150	23.45	38	8.14	18.40	35.0	48.28	7.26	569	12.2	24.6	2.51	937	6.65
117-723C-3H-5, 145-150	24.95	44	8.10	20.66	—	44.67	6.01	—	6.1	6.7	2.13	770	7.43
117-723C-4H-2, 145-150	30.05	36	8.00	27.39	—	37.99	5.72	—	13.0	8.4	3.89	799	6.64
117-723C-4H-5, 145-150	34.55	46	7.70	29.68	—	37.12	5.56	—	8.5	8.3	5.80	838	6.68
117-723C-5H-2, 145-150	39.75	37	7.80	32.50	—	35.57	5.53	—	2.2	13.0	6.91	1030	6.43
117-723C-5H-5, 145-150	44.25	53	7.80	35.26	—	37.71	5.29	—	0	11.4	9.13	1004	7.13
117-723I-6I-1, 0-1	46.40	10	7.70	30.17	—	41.40	7.36	—	4.6	43.6	7.77	1110	5.58
117-723C-6H-2, 145-150	49.35	32	7.60	36.28	—	36.56	5.09	—	0.7	14.4	11.69	991	7.18
117-723A-6H-4, 145-150	52.35	41	7.38	40.60	34.2	35.26	5.17	559	0	19.9	12.17	991	6.82
117-723C-6H-5, 145-150	53.85	30	7.80	36.47	—	34.92	4.91	—	0	18.2	12.96	1082	7.11
117-723C-7H-3, 145-150	59.46	35	7.60	41.45	—	35.33	4.74	—	1.6	16.7	15.09	1030	7.45
117-723C-7H-6, 145-150	63.96	39	7.80	45.33	—	36.62	4.48	—	0	16.0	16.06	1053	8.17
117-723I-8I-1, 0-1	65.80	10	7.60	43.96	—	43.96	7.99	—	7.3	19.4	13.08	1077	5.50
117-723C-8H-2, 145-150	68.75	48	7.70	43.85	—	36.79	3.99	—	0.7	19.4	18.14	1082	9.22
117-723C-8H-5, 145-150	73.25	42	7.80	35.67	—	35.67	3.45	—	0	19.2	20.03	1077	10.34
117-723I-9I-1, 0-1	75.40	10	7.70	58.91	—	38.61	7.32	—	0.7	6.8	17.77	1230	5.27
117-723A-9H-4, 145-150	81.35	36	7.58	47.20	34.2	33.12	3.25	553	0	23.2	20.46	941	10.19
117-723A-13X-4, 140-150	120.05	35	7.49	73.90	35.4	33.09	4.04	540	0	37.4	28.29	1020	8.19
117-723A-17X-1, 145-150	154.25	33	—	76.30	35.0	28.65	2.66	534	0	29.5	35.25	1062	10.77
117-723A-20X-4, 145-150	187.75	36	7.26	82.40	35.4	25.98	3.00	534	0	27.7	37.04	1085	8.66
117-723A-23X-1, 145-150	212.25	35	7.96	88.50	35.2	22.82	1.77	532	0	—	37.84	1042	12.89
117-723A-26X-3, 145-150	244.25	30	7.51	91.60	35.5	22.60	2.76	529	0.6	32.5	39.62	1052	8.19
117-723A-29X-6, 145-150	277.65	30	7.55	97.70	35.0	20.65	2.07	531	1.1	31.3	41.0	1211	9.98
117-723A-32X-5, 145-150	304.95	39	7.47	97.80	35.2	18.29	2.39	529	0.4	34.6	40.0	1144	7.65
117-723A-36X-5, 145-150	333.54	53	7.21	106.80	36.0	19.09	2.74	533	1.6	32.3	40.4	1196	6.97
117-723A-39X-5, 145-150	362.45	53	7.06	93.90	36.0	17.35	2.92	533	1.9	29.8	40.4	1211	5.94
117-723A-42X-1, 140-150	385.40	49	7.81	106.70	36.0	16.67	4.08	527	2.2	27.4	37.0	1401	4.09

Table 11. Dissolved organic carbon data, Site 723.

Core, sample, interval (cm)	Depth (mbsf)	Dissolved organic carbon (a.u.)
117-723C-1H-2, 145	2.95	0.602
117-723C-1H-5, 145	7.45	0.644
117-723C-2H-2, 145	10.75	0.660
117-723C-2H-5, 145	15.25	0.694
117-723C-3H-2, 145	20.45	1.004
117-723C-3H-5, 145	24.95	1.070
117-723C-4H-2, 145	30.05	2.366
117-723C-4H-5, 145	34.55	1.360
117-723C-5H-2, 145	39.37	1.215
117-723C-5H-5, 145	44.25	1.200
117-723C-6I-1, 1	46.60	1.449
117-723C-6H-2, 145	49.35	1.241
117-723C-6H-5, 145	52.35	1.216
117-723C-7H-3, 145	59.46	1.160
117-723C-7H-6, 145	63.96	1.267
117-723C-8I-1, 1	65.80	0.920
117-723C-8H-2, 145	68.75	1.230
117-723C-8H-5, 145	73.25	1.228
117-723C-9I-1, 1	75.00	0.993
117-723A-17X-1, 145	154.25	1.412
117-723A-20X-4, 145	187.75	1.360
117-723A-26X-3, 145	244.25	1.827
117-723A-29X-6, 145	244.25	2.004
117-723A-32X-5, 145	304.95	2.103
117-723A-36X-5, 145	333.45	2.031
117-723A-39X-4, 145	362.45	2.104
117-723A-42X-1, 145	385.40	2.166

Note: a.u. = absorbance unit.

Kaolinite is not present in the sediments at this site. Slow scans from 24°–26.5° of a pair of samples from Cores 117-723A-3H and -9H showed only a peak corresponding to the chlorite 003 reflection: the kaolinite 002 peak was absent in both cases. These observations agree with the results of Kolla et al. (1981), who showed that sediments near the coast of northern Oman are chlorite rich and kaolinite poor. Farther to the south, kaolinite becomes increasingly more abundant.

Illite is common throughout the cored sequence. We use the term illite in a generic sense here—muscovite and/or biotite may also be present in the sediments but yield diffraction spectra which overlap that of illite. We have made no attempt to differentiate these minerals. The illite 001 peak is broader than that observed in diffractograms of Indus Fan sediments, as was noted in lithologic Units I and II at Site 722. We attribute the broadening to the presence of palygorskite, which has its principal reflection at ~10.5 A, adjacent to the 10 A illite 001 peak. Indeed, a slow scan from 7° to 10° of Sample 117-723A-3H-4, 145 cm, showed a shallow but distinct separation between the two peaks confirming the presence of palygorskite. This mineral is abundant in soils on the Arabian Peninsula (Müller, 1961, cited in Kolla et al., 1981), and its occurrence at Site 723 probably reflects eolian transport from the adjacent landmass.

Fluorapatite occurs in trace concentrations throughout the hole as brown to golden fragments of fish bones and apparently authigenic aggregates having rough or knobby surface textures. This material was recovered from the >250 μm sieve fraction of four core-catcher samples spaced across the cored sequence. The bone fragments and aggregates tended to be very small, typically <1 mm in size. The occurrence of the apparently authigenic material in visible quantities at this site is consistent with the distribution of phosphate in interstitial water as discussed above.

A single sample of a whitish or cream-colored, partly fibrous aggregate about 1 cm in diameter was collected from Core 117-723B-24X and diffracted. The material was found to consist of a mixture of aragonite and calcite and was suspected to be a partly comminuted shell fragment in a matrix of nannofossil ooze.

A sample of one of the "limestone" layers from the lower half of Hole 723A was shown by diffractometry to be nearly pure dolomite. The spacing of the (211) reflection can be used

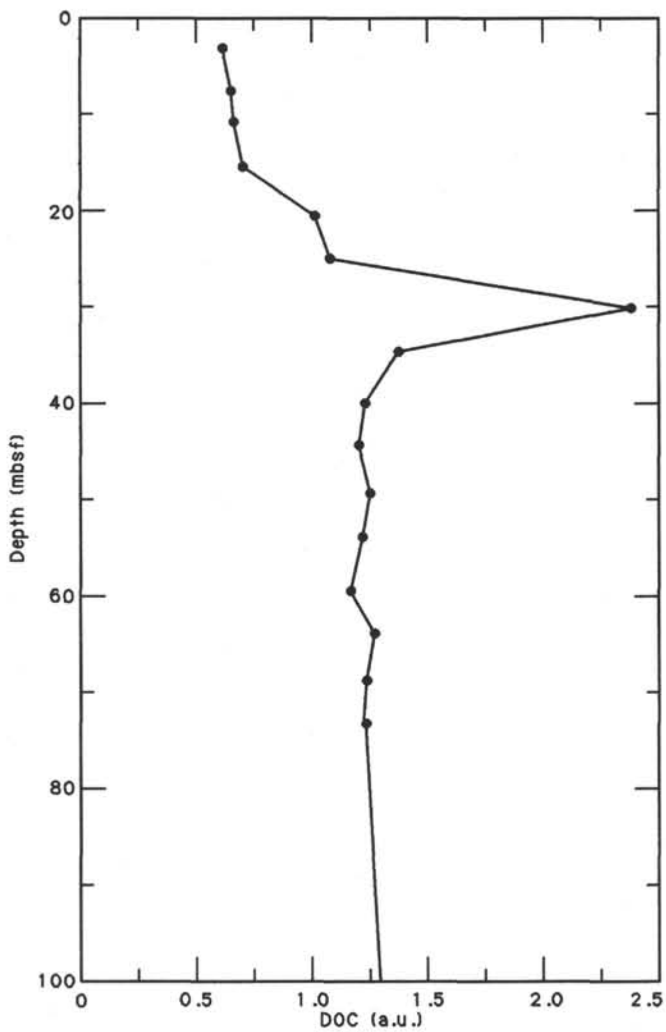

Figure 35. High-resolution dissolved organic carbon (DOC) profile, Hole 723C. Note that the data are plotted in terms of absorbance units (a.u.) and indicate relative concentration only.

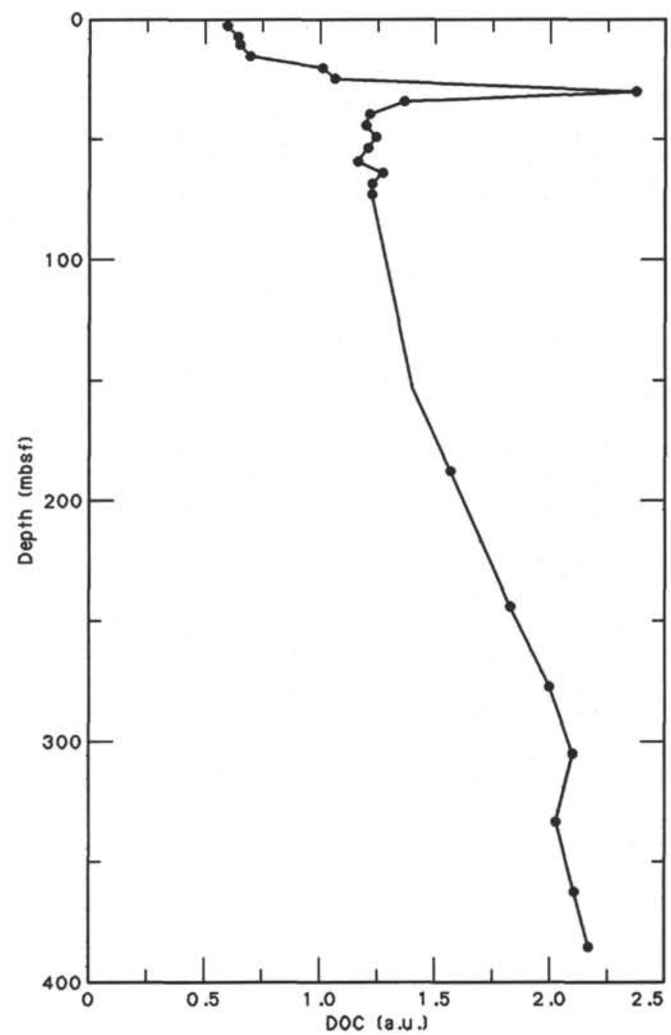

Figure 36. Stacked dissolved organic carbon (DOC) profile at Site 723 compiled from data from Holes 723A and 723C. Note that the data are plotted in terms of absorbance units (a.u.) and indicate relative concentration only.

as an indicator of the magnesium content; in this case, the spacing indicated that dolomite comprising the dolostone contained 52 mol% magnesium.

ORGANIC GEOCHEMISTRY

The organic carbon concentration in 125 Pleistocene to upper Pliocene sediment samples from Site 723 ranges from 0.71% to 6.83% (mean of 3.23%) and shows a slight increase with depth. Organic matter is immature and rich in marine-derived, lipid-rich material, which has not been noticeably degraded by diagenesis.

The influx of sulfate from the subsurface produces high alkalinity in pore waters while depleting interstitial methane or impeding biogenic fermentation reactions. Gas expansion throughout the recovered section thus appears to be due mainly to high partial pressures of CO_2 gas. The fairly steady increase of ethane and propane with depth points to a production of gas at greater depth by early thermogenic cracking of organic matter.

Variations in paleotemperatures of the sea-surface water, as recorded by the U^k_{37} index, are of the same magnitude as measured at Site 721 (Owen Ridge). The molecular index for relative temperatures shows, however, that water temperatures were colder over the margin when compared with the more distal Owen Ridge.

Organic Matter Abundance and Character

The Pleistocene to uppermost Pliocene sediments at Site 723 are rich in organic carbon. Values reach up to 6.83% and rarely fall below 1% (Fig. 37). A trend toward higher values at the base of the hole may indicate that the oldest sediments recovered are the richest organically, although the data may be biased by nonrepresentative sampling. Such high organic carbon values are most likely the result of high primary productivity in the monsoon-induced seasonal upwelling. Given the high sedimentation rates at this site and concomitant enhanced preservation, the Neogene sediments constitute ideal substrates for anaerobic remineralization at depth.

A subset of 88 samples was subjected to Rock-Eval pyrolysis in order to decipher the nature and maturity of the organic matter. The results are given in Table 12. The Rock-Eval apparatus is equipped with a module to analyze total organic carbon (TOC) and these results are listed as TOC[a] in Table 12. A comparison of the Rock-Eval TOC values with the TOC values measured by difference (TOC[b] in Table 12; see "Explanatory Notes,"

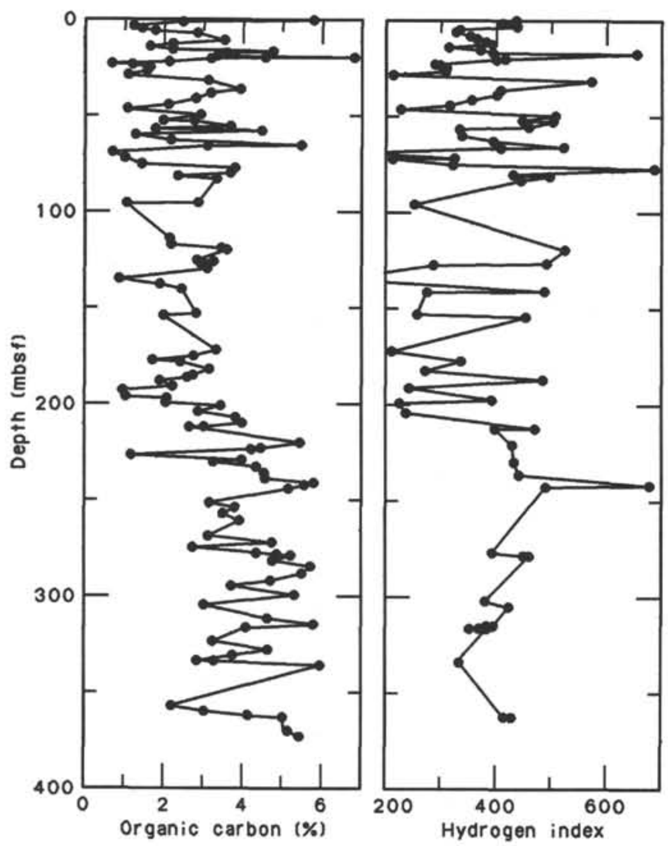

Figure 37. Downhole plots of organic carbon and the hydrogen index in Hole 723A.

this volume) shows that the Rock-Eval results are unreliable. Therefore, the hydrogen (HI) and oxygen indices (OI) were recalculated on the basis of the TOC[b] data (Table 12). They are plotted in Figure 38, together with the results from Site 722.

Generally, samples from the margin sites are characterized by higher HI and lower OI values when compared with samples from Site 722 on the Owen Ridge. This can best be explained by a higher input of lipid-rich organic material at the margin sites due to increased primary productivity in combination with enhanced preservation conditions. The uniformly low temperatures of maximum pyrolysis ($T_{max} < 435°C$) point to an immature character of the organic matter (Table 12).

The hydrogen and oxygen indices are measures of the amount of hydrocarbons and CO_2, respectively, liberated by pyrolysis and normalized to the organic carbon content of the sample. They should be constant if organic matter was produced by one type of primary producers and not altered by diagenesis. A plot of the HI and the OI vs. organic carbon of samples from Site 723 is shown in Figure 39. We can see that the HI appears to stabilize around 400 at a value of approximately 3% organic carbon, while the OI stabilizes at a value of around 100. It seems that with rapid burial of sediments containing 3% or more organic carbon, hydrogen-rich material is not further depleted.

Hydrocarbon Gases

Samples for interstitial gas analysis with the headspace method were taken in several cores from Hole 723A and 723B, and in Sections 2 and 5 from each core of Hole 723C. The results are given in Table 13 and are shown vs. depth in Figure 40. Methane concentrations are high in the uppermost 100 m of the sedimentary sequence and tend to level out at depth. This contrasts with the ethane and propane concentrations, which both show a steady increase with depth. Even though Whelan et al. (1982) reported the occurrence of trace amounts of volatile C_1–C_8 hydrocarbons in macroalgae, it is not clear whether any biogenic source can account for C_2–C_8 hydrocarbons in sediments. Therefore, we are inclined to ascribe the observed downhole increase of ethane and propane to early thermogenic cracking of organic matter at depth.

Production of biogenic methane in the deeper sediments is inhibited because an increase of interstitial sulfate was observed (see "Inorganic Geochemistry" section, this chapter). The expected concentrations of thermogenic methane in addition to ethane and propane are likely to be masked by traces of biogenic methane persisting throughout the section. Gas concentrations measured quantitatively in Holes 723A and 723C, while showing similar trends, do not agree well and suggest that the method of quantifying interstitial gas with the shipboard methodology is far from being truly quantitative.

Similar gas distribution profiles were compiled from measurements of vacutainer samples of gas pockets (Table 14 and Fig. 41). In addition to the aforementioned gases, butane and isobutane were observed to increase with depth, which corroborates the suggestion that the C_{2+} interstitial gas is thermogenic in origin.

Lipid Analyses

We analyzed 18 samples from the first three cores of Hole 723B for the relative abundance of di- and triunsaturated ketones (see "Explanatory Notes" and "Organic Geochemistry" section, "Site 721" chapter, this volume). The results, expressed as an alkenone unsaturation index U^k_{37}, together with the organic carbon and $CaCO_3$ content of these samples, are listed in Table 15 and are shown vs. depth in Figure 42.

The U^k_{37} ratio ranges from 0.80 to 0.91. This corresponds to sea-surface water temperatures of 23°C and 26.5°C, respectively. These values are significantly lower than those measured on sediments from Site 721, located on the Owen Ridge (U^k_{37} = 0.88–0.97). The shift to lower values is the expected result of upwelling of deep cold water near the margin. Of notable interest is that the interval between 9 and 13 mbsf is characterized by low U^k_{37} values, pointing to cold sea-surface water temperatures during the time of deposition, which might be related to an intensification of the upwelling. The organic carbon values of this interval are also slightly enhanced in comparison with the bounding sediments, but they never reach the value measured in the uppermost sample. This sample shows the highest U^k_{37} index and has thus been deposited under warm sea-surface water conditions.

DOWNHOLE MEASUREMENTS

Three logging runs of Schlumberger tool strings were conducted in Hole 723B. The seismic stratigraphic combination (BHC/DIT/GR/CALI; see "Explanatory Notes," this volume) was run in the openhole interval, logging downward from 92.2 to 415.0 mbsf, followed by logging upward from 429.0 to 100.9 mbsf. The lithoporosity combination (LDT/CNL/NGT/GPIT) was run through both pipe and openhole, logging downward from just above the seafloor to 410.8 mbsf, then logging upward from 426 mbsf to the seafloor. The geochemical combination (GST/ACT/GPIT) was run logging upward from 422.1 to 70.5 mbsf. Very little fill was encountered in the hole, so the bottom of the tool strings reached between 0 and 6 m of the 429 mbsf total depth on different runs.

Log Quality and Processing

Unedited original logs are shown following the barrel sheets. Log quality was generally very good. The major exception was that the caliper was unreliable; this is often true for ODP caliper

Table 12. Results of Rock-Eval pyrolysis of sediment samples from Holes 723A and 723B.

Core, sample, interval (cm)	Depth (mbsf)	S_1	S_2	S_3	S_2/S_3	TOC[a]	TOC[b]	HI	OI
117-723A-									
1H-1, 43-44	0.43	5.26	23.29	9.80	2.37	5.38	5.80	402	169
1H-2, 43-44	1.93	1.56	9.28	4.74	1.95	2.27	2.51	370	189
1H-3, 43-44	3.43	0.45	3.31	2.79	1.18	0.76	1.25	265	223
1H-4, 43-44	4.93	0.47	3.58	2.38	1.50	1.07	1.49	240	159
1H-4, 144-145	5.94	0.53	4.16	2.93	1.41	1.27	1.80	231	163
1H-5, 43-44	6.43	0.61	4.29	2.68	1.60	1.31	ND	327	[c]204
2H-1, 43-44	8.23	0.85	5.52	2.96	1.86	1.56	ND	353	[c]189
2H-2, 43-44	9.73	1.50	9.94	4.22	2.35	2.73	ND	364	[c]154
2H-3, 43-44	11.23	2.09	12.29	4.14	2.96	3.24	3.56	345	116
2H-4, 43-44	12.73	1.22	7.22	3.44	2.09	1.85	2.25	321	151
2H-5, 43-44	14.23	0.29	3.00	2.36	1.27	0.95	1.68	179	140
2H-6, 43-44	15.73	0.97	6.47	3.21	2.01	1.74	2.27	285	141
2H-7, 43-44	17.23	2.06	11.56	4.62	2.50	2.94	4.77	242	97
3H-1, 43-44	17.93	1.22	10.74	4.75	2.26	1.64	3.59	299	132
3H-2, 43-44	19.43	1.23	10.42	4.50	2.31	2.58	3.38	308	133
3H-2, 128-129	20.28	2.57	15.67	5.19	3.01	3.85	4.58	342	113
3H-2, 138-139	20.38	8.87	33.96	7.46	4.55	8.19	6.83	497	109
3H-3, 43-44	20.93	1.83	13.20	5.03	2.62	3.30	3.20	412	157
3H-4, 144-145	23.44	0.17	1.54	1.87	0.82	0.53	0.71	217	263
3H-5, 43-44	23.93	0.38	3.13	1.99	1.57	1.05	1.23	254	162
3H-6, 43-44	25.43	0.46	3.07	1.73	1.77	0.99	1.66	185	104
3H-7, 43-44	26.93	1.05	4.88	2.21	2.20	1.58	1.60	305	138
4H-2, 43-44	29.03	0.25	2.23	1.43	1.55	1.04	1.12	199	128
4H-4, 43-44	32.03	1.75	10.59	3.39	3.12	1.85	3.16	335	107
4H-7, 43-44	36.53	2.99	15.53	4.38	3.54	3.81	3.98	400	110
5H-2, 43-44	38.73	2.19	12.21	3.90	3.13	3.04	3.19	382	122
5H-4, 43-44	41.73	1.24	10.20	3.45	2.95	0.97	2.85	358	121
5H-6, 43-44	44.73	0.82	6.16	2.45	2.51	1.95	2.16	285	113
6H-1, 43-44	46.83	0.42	2.48	2.28	1.08	1.08	1.12	221	203
6H-3, 43-44	49.83	1.22	10.81	3.29	3.28	2.14	2.95	366	111
6H-4, 144-145	52.34	0.89	8.13	3.35	2.42	1.82	2.04	398	164
6H-5, 43-44	52.83	0.97	8.69	3.54	2.45	1.74	2.79	311	127
6H-7, 43-44	55.83	1.96	14.11	4.01	3.51	3.08	3.72	379	108
7H-2, 43-44	56.94	0.85	5.08	2.74	1.85	1.52	1.82	279	150
7H-4, 43-44	59.94	0.58	3.93	2.34	1.67	1.16	1.32	297	177
7H-6, 43-44	62.94	1.20	7.85	3.13	2.50	1.99	2.22	354	141
7H-8, 43-44	65.94	4.80	22.67	5.61	4.04	4.35	5.51	411	102
8H-1, 43-44	66.23	1.86	11.84	3.63	3.26	2.90	3.12	397	116
8H-3, 43-44	69.23	0.18	1.07	1.77	0.60	0.75	0.76	140	233
8H-4, 149-150	71.79	0.33	2.74	1.94	1.41	0.84	1.09	251	178
8H-5, 43-44	72.23	0.30	2.06	1.96	1.05	0.96	1.07	193	183
8H-7, 43-44	75.23	0.62	3.98	2.15	1.85	1.23	1.48	269	145
9H-2, 43-44	77.33	2.58	14.66	3.99	3.67	2.13	3.85	381	104
9H-4, 43-44	80.33	3.90	16.10	3.65	4.41	3.74	3.68	438	99
9H-4, 144-150	81.34	1.47	10.93	2.97	3.68	2.20	2.42	452	123
9H-6, 43-44	83.33	1.35	9.57	2.62	3.65	2.16	3.37	284	78
11X-1, 149-150	96.29	0.44	2.77	1.81	1.53	1.09	1.09	254	166
13X-4, 119-120	119.79	1.54	15.25	3.85	3.96	2.91	3.49	437	110
14X-2, 149-150	126.79	2.00	13.69	3.36	4.07	2.78	3.28	417	102
14X-3, 70-71	127.50	2.01	12.38	2.40	5.15	4.31	2.97	417	81
15X-2, 43-44	135.33	0.29	1.66	1.05	1.58	1.28	0.92	180	114
15X-6, 0-1	140.90	1.74	10.58	2.95	3.58	2.16	2.51	422	118
15X-6, 70-71	141.60	2.32	11.24	2.05	5.48	4.05	2.81	400	73
17X-1, 43-44	153.23	2.20	9.90	2.45	4.04	3.80	2.86	346	86
17X-2, 0-1	154.30	0.99	7.81	2.46	3.17	1.72	2.06	379	119
19X-1, 42-43	172.52	1.09	7.99	2.02	3.95	3.71	3.35	239	60
19X-4, 64-65	177.24	0.52	4.68	2.39	1.95	1.38	1.76	266	136
20X-1, 40-41	182.20	1.71	12.14	2.39	5.07	4.43	3.17	383	75
20X-4, 30-31	186.60	1.21	10.47	3.02	3.46	2.16	2.65	395	114
20X-7, 40-41	191.20	1.27	8.26	2.08	3.97	3.35	2.26	365	92
21X-5, 0-1	197.40	0.94	7.67	2.51	3.05	1.94	2.12	362	118
21X-6, 45-46	199.35	1.21	8.49	2.12	4.00	3.70	2.11	402	100
22X-3, 29-30	204.39	1.84	11.44	2.34	4.88	4.74	2.92	392	80
23X-2, 0-1	212.30	1.88	12.00	3.46	3.46	2.54	3.04	395	114
23X-2, 31-32	212.61	1.55	10.84	2.63	4.12	4.16	2.71	400	97
24X-1, 48-49	220.88	5.14	23.61	3.97	5.94	7.95	5.49	430	72
24X-7, 27-28	229.67	3.86	17.33	2.88	6.01	7.06	4.01	432	72
25X-5, 43-44	236.53	3.84	20.44	3.43	5.95	7.28	4.60	444	75
26X-2, 24-25	241.54	3.64	22.31	3.79	5.88	3.29	5.85	381	65
26X-3, 0-1	242.80	3.58	25.78	4.65	5.54	5.22	5.60	460	83
29X-6, 119-120	276.70	6.19	18.43	3.56	5.17	4.62	4.39	420	81
30X-1, 0-1	278.30	4.19	22.10	3.46	6.38	4.78	4.90	451	71
30X-1, 0-1	278.30	4.41	21.25	4.10	5.18	4.69	4.90	434	[d]84
32X-3, 119-120	301.69	1.82	11.94	3.28	3.64	3.10	ND	385	[c]105
32X-5, 119-120	304.69	1.70	12.30	2.69	4.57	2.89	3.06	402	88
33X-2, 78-79	315.28	6.00	18.33	3.50	5.23	4.62	ND	396	[c]75

Table 12 (continued).

Core, sample, interval (cm)	Depth (mbsf)	S_1	S_2	S_3	S_2/S_3	TOC[a]	TOC[b]	HI	OI
117-723A-									
33X-2, 88-89	315.38	3.67	11.07	3.11	3.55	2.85	ND	388	[c]109
33X-2, 98-99	315.48	5.00	16.92	3.38	5.00	4.21	ND	401	[c]80
33X-2, 118-119	315.68	4.91	15.45	4.10	3.76	3.93	ND	393	[c]104
33X-2, 128-129	315.78	3.88	11.99	3.98	3.01	3.12	ND	384	[c]127
33X-2, 138-139	315.88	4.21	12.18	3.75	3.24	3.25	ND	374	[c]115
33X-2, 148-149	315.98	4.11	13.23	3.98	3.32	3.59	ND	368	[c]110
33X-3, 8-9	316.08	3.65	15.15	4.42	3.42	3.90	ND	388	[c]113
33X-3, 20-21	316.20	4.23	15.23	3.71	4.10	4.07	ND	374	[c]91
33X-3, 28-29	316.28	2.44	11.20	3.67	3.05	3.17	ND	353	[c]115
33X-3, 38-39	316.38	1.99	10.48	3.27	3.20	2.91	2.91	360	112
33X-3, 48-49	316.48	3.19	12.87	3.30	3.90	3.32	3.32	387	99
36X-6, 0-1	333.59	3.12	11.60	3.23	3.59	3.44	2.91	399	111
36X-6, 0-1	333.59	3.75	12.09	3.52	3.43	3.57	2.91	415	[d]121
39X-5, 119-120	362.19	2.16	18.19	3.33	5.46	4.25	4.17	436	80
39X-5, 119-120	362.19	2.99	18.44	3.80	4.85	4.42	4.17	442	[d]91

Note: HI = hydrogen index and OI = oxygen index; the hydrogen and oxygen indices were calculated on the basis of the TOC[b] values. For a detailed description of parameters, see "Explanatory Notes" chapter (this volume). ND = not determined.
[a] Organic carbon measured by Rock-Eval.
[b] Organic carbon measured by difference.
[c] Hydrogen and oxygen values calculated from Rock-Eval organic carbon data.
[d] Duplicate analysis.

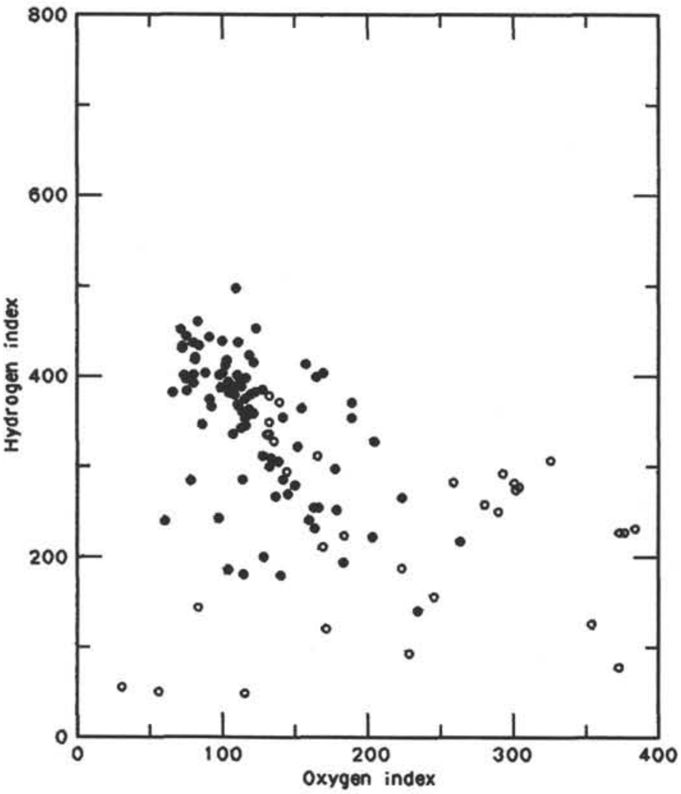

Figure 38. Plot of hydrogen index vs. oxygen index of samples from Holes 723A and 723B (dots) compared with samples from Hole 722 (circles).

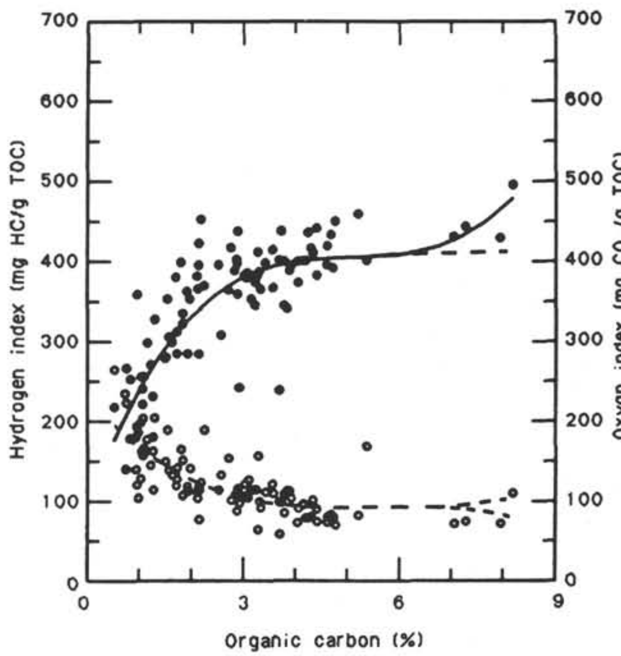

Figure 39. Cross plot of hydrogen index (dots) and oxygen index (circles) vs. organic carbon of samples from Hole 723A and 723B. Lines are polynomial least-squares regressions. TOC values are from the Rock-Eval instruments.

logs. A caliper was calculated from sonic traveltimes, but it indicated only a minimum size of 0.4 m for the borehole. The sonic log exhibited some cycle skipping, which was removed manually before reprocessing. Geochemical logs were reprocessed postcruise and converted to oxide dry weight percentages, as described in the "Explanatory Notes" chapter (this volume). Reproducibility of logs was generally excellent, based on a comparison of downgoing and upcoming logs for the first two tool strings. The lowest reproducibility was found for the hole deviation and magnetometer logs. Except for these logs, usually only the upcoming logs are shown in the figures.

Logs from the seismic stratigraphic combination were depth shifted downward by 2.4 m, and logs from the lithoporosity and geochemical combinations were depth shifted downward by 2.2 m. The amount of the depth adjustment was based on detection of three horizons in logs that were also measured during drilling: the base of pipe, a thin dolomite bed at 247.2 mbsf, and a thin dolomite bed at 317.3 mbsf. These two dolomite beds are

Table 13. Concentrations of methane (C_1), ethane (C_2), and propane (C_3) per liter of wet sediment in cores of Holes 723A, 723B, and 723C.

Core, sample, interval (cm)	Depth (mbsf)	C_1 (μL/L)	C_2 (μL/L)	C_3 (μL/L)	C_1:C_2
117-723A-					
1H-4, 144-145	5.94	346210	21	5	16486
3H-4, 144-145	23.44	165220	11	2	15020
6H-4, 144-145	52.34	106240	14	10	7589
7H-7, 149-150	65.50	123415	23	26	5366
8H-4, 140-141	71.70	13415	5	4	2683
9H-4, 144-145	81.34	117000	20	21	5850
11X-1, 149-150	96.29	55290	15	20	3686
13X-4, 119-120	119.79	42095	20	30	2104
14X-2, 149-150	126.79	24115	15	25	1608
15X-6, 0-1	140.90	5850	20	45	293
17X-2, 0-1	154.30	7380	12	24	607
19X-4, 149-150	178.09	41835	6	0	6972
20X-4, 30-31	186.60	160425	23	20	6975
21X-5, 0-1	197.40	6895	20	35	345
23X-2, 0-1	212.30	4440	30	55	15
24X-3, 0-1	223.40	5687	17	33	335
26X-3, 0-1	242.80	2457	30	67	82
29X-6, 119-120	277.39	4200	24	54	175
30X-1, 0-1	278.30	3550	35	70	101
32X-5, 119-120	304.69	2740	25	50	110
36X-6, 0-1	333.59	6335	25	55	253
39X-5, 119-120	362.19	2410	50	105	48
117-723B-					
2H-3, 149-150	8.79	4990	9		554
4H-3, 149-150	28.09	235			
5H-3, 149-150	37.79	188420	20	10	9421
10X-2, 0-1	83.10	535			
13X-4, 149-150	116.29	180520	40	50	4513
16X-2, 149-150	142.19	54710	15	25	3647
18X-5, 0-1	164.60	10515	20	30	526
22X-6, 0-1	204.80	6675	35	65	191
25X-5, 149-150	233.69	6655	85	140	78
33X-2, 0-1	314.50	1745	45	95	39
40X-3, 149-150	375.79	5950	10		595
117-723C-					
1H-2, 144-145	2.94	125	5		8
1H-5, 144-145	7.44	150	1		30
2H-2, 144-145	12.14	415	15	20	28
2H-5, 144-145	16.64	355	5		71
3H-2, 144-145	21.84	1330	15	10	89
3H-3, 144-145	23.34	1005	15		67
4H-2, 144-145	31.44	194055	25	5	7762
4H-5, 144-145	35.94	289880	30	10	9663
5H-2, 144-145	41.14	163505	10	5	16351
5H-5, 144-145	45.64	175775	20	10	8789
6H-2, 144-145	50.74	151880	25	20	6075
6H-5, 144-145	55.24	137815	25	15	5513
7H-3, 144-145	61.94	36490	10	10	3649
7H-5, 144-145	64.94	113800	30	30	3793
8H-2, 144-145	70.14	128531	52	65	2472
8H-5, 144-145	74.64	25955	10	15	2596

Note: Values are expressed in μL/L (volume gas/volume wet sediment).

the only dolomites with precisely known depths based on core recovery.

Only the spectral gamma-ray and neutron logs were run through pipe. Pipe attenuates the signal of both tools, but useful information is still present, though of lower quality than openhole logs. Figure 43 illustrates this conclusion with a comparison of upcoming and downgoing uranium logs. The through-pipe logs shown in Figure 43 are obtained after multiplying raw counts by an empirical gain model to correct for the attenuation of gamma rays by passage through pipe. The shape of this model (Fig. 43) is based on known variations in pipe thickness: the BHA is twice as thick as drill pipe, and drill pipe has increased thickness every 10 m at pipe joints.

The amplitude of the gain model is based on a comparison of the mean uranium reading for 15-m intervals immediately above and below pipe, which suggests that the BHA suppresses uranium counts by a factor of about 6; a similar suppression of the standard deviation was seen. This estimate is probably less accurate at Site 723 than at most sites because of the strong cyclicity and variability in the short intervals used for establishing the gain factor. Indeed, a gain of only 3 was estimated from a similar analysis at Site 728 (see "Site 728" chapter, this volume), and we know of no published research on pipe attenuation. The gain factor has only a small effect on the agreement between logs. Pipe was not set at exactly the same depth for both runs, and the small peak shown at 92-99 mbsf in the downgoing through-pipe log is confirmed by the upcoming openhole log (Fig. 43).

Character match between through-pipe logs is generally reasonable, though less than observed for the openhole logs (Fig. 43). The one marked disagreement between the two through-pipe logs is in the magnitude of the uranium peak at 36 mbsf. Small depth shifts between the two logs appear to be present, as evidenced by slight differences in the depths of peaks or troughs between runs.

Dolomite Layers

The most obvious feature of many of the logs is the occurrence of several thin spikes. These spikes are high in velocity, resistivity, and density and low in neutron porosity (Figs. 44 and 45). Within-log variability of spike amplitudes is probably a function more of bed thickness than of differences in composition or porosity of these hard streaks, or cemented intervals. Many of the beds are thinner than the vertical resolution of the logs, and amplitudes are reduced accordingly.

Based on log responses alone, we identified nine hard streaks: at 223, 247, 260, 268, 300, 317-318, 337-338, 374, and 408 mbsf. These nine are visible on the sonic and resistivity logs (Fig. 44). All are also detectable on the signal strength (CSIG) of the gamma spectrometry tool, but the horizons at 223 and 268 mbsf are too subtle to have been picked from this log alone. These two hard streaks are subtle also on the neutron porosity and density logs, as is the 30-mbsf horizon, but the other six hard streaks are obvious on the density log. Five of the six are also obvious on the neutron log (Fig. 45). The hard streaks at 223, 268, and 300 mbsf are probably thinner than the others. Even thinner hard streaks may be present (e.g., at 192 and 355 mbsf), but they cannot be identified as such with confidence. The most pronounced hard streaks are also detected at the same depths in cores and are marked by substantial decreases in the penetration rate on the drilling record (see "Lithostratigraphy" section, this chapter).

These hard streaks are probably dolomite, based on a single X-ray diffraction measurement (see "Inorganic Geochemistry" section, this chapter) and the similarity in log responses of different beds. Most log responses (e.g., density, velocity, porosity, and thorium/potassium natural radioactivity; Figs. 44 and 45) are consistent with either dolomite or calcite, with near-zero porosities. However, the photoelectric effect (Fig. 45) is much more consistent with dolomite (Pe = 3.14) than with calcite (Pe = 5.08). Most of the hard streaks are subtle or undetectable (Pe = 2.9-3.3) on the log of photoelectric effect, presumably because dolomite Pe is near the 2.5-3.5 range of most of the Pe log. In contrast, the low "background" Pe below 350 mbsf makes the hard streaks at 374 and 408 mbsf quite evident on the Pe log, with maximum Pe values of 3.1 and 3.5.

Geochemical logs (Fig. 46) indicate that the hard streaks are either dolomite or calcite plus dolomite. Calcium and magne-

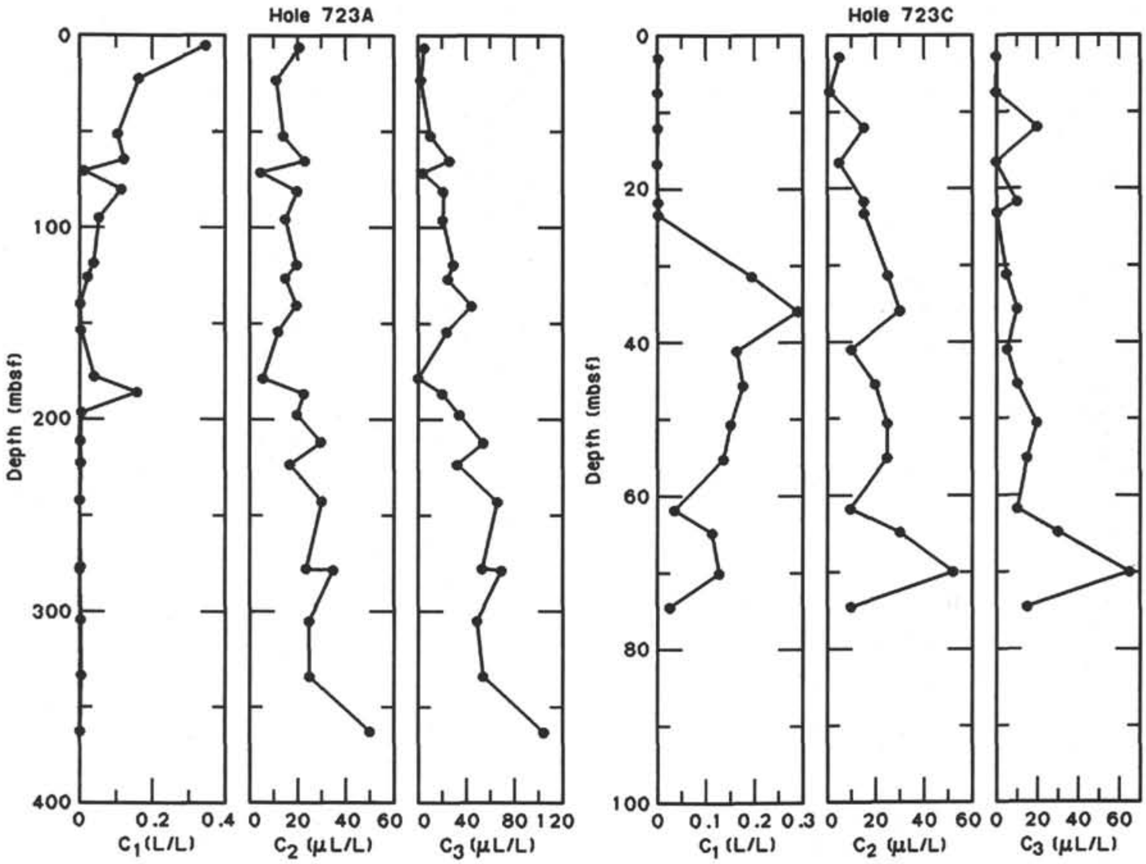

Figure 40. Downhole concentrations of methane (C_1), ethane (C_2), and propane (C_3) in headspace samples from Holes 723A and 723C.

sium spikes to high values invariably occur at the locations of hard streaks. Magnesium oxide never reaches a peak abundance greater than 12%, but the much higher concentrations of calcium oxide could be caused by the thin-bed effect rather than by a mixture of calcite and dolomite in the hard streaks. The hard streaks at 247 and 374 mbsf are particularly obvious on the geochemical logs (Fig. 46). Quartz depletion in the hard streaks is indicated by consistently low concentrations of SiO_2, falling to zero at 374 mbsf. Aluminum and potassium are usually low (a notable exception is the potassium peak at 300 mbsf), indicating low clay content. Other elements (iron, titanium, sulfur, gadolinium, thorium, and uranium) show a less consistent pattern at locations of the dolomite beds.

Diagenetic precipitation from advecting fluids is clearly the cause of the dolomite stringers. In general, geochemical log behavior in the dolomite stringers suggests that dolomite precipitation occurred preferentially in locations high in carbonate and low in clay (K_2O, thorium, Al_2O_3), quartz (SiO_2), and organic carbon (U). Uranium is often dissolved from calcite by circulating fluids; it is then concentrated at the depth of precipitation (e.g., Fertl, 1979; "Site 722" chapter, this volume) if this depth is adjacent to reducing sediments (e.g., an organic-rich horizon). Such a concentration is notably absent at Site 723.

The compaction pattern at Site 723, as revealed by the sonic, density, and neutron porosity logs, is unaffected by the presence of dolomite horizons. A significant density borehole correction (DRHO) usually occurs in the 2 m immediately below each dolomite bed, and both low density and high porosity are often logged in the 2 m immediately above each dolomite bed. However, these changes are probably washouts, caused by increased circulation during drilling of the hard horizons; the changes do not reflect actual porosity lows. The absence of shifts in the porosity baseline across the dolomite beds, in spite of their very low permeability, suggests that they are stringers lacking lateral continuity rather than widespread horizons. Thus, they do not significantly retard continuing compaction. This conclusion is supported by the comparison of a synthetic seismogram with the seismic line across the site, discussed in the "Seismic Stratigraphy" section (this chapter). This conclusion is also supported by the observation that only some of the dolomite horizons detected in cores and the drilling record at Hole 723B were also detected at 723A, only a few meters away.

The source of the magnesium in the dolomite stringers is not known with certainty. Magnesium in interstitial waters exhibits a rapid decrease with increasing depth, suggesting diffusion and depletion of seawater magnesium (see "Inorganic Geochemistry" section, this chapter). The geochemical logs (Fig. 46) indicate generally high magnesium oxide contents of 4%–9%. The magnesium oxide is inversely correlated with SiO_2, indicating that it is not residing primarily in clays. Magnesium oxide is very positively correlated with calcium oxide, suggesting that dolomite is present in significant quantities throughout the logged section. However, mineral identification from smear slides (see barrel sheets) detected only trace amounts of authigenic dolomite. Based on calcium oxide and magnesium oxide log responses, it is possible that about a third of the detrital carbonate identified in smear slides is actually detrital dolomite. Dissolution of part of this possible detrital dolomite could be a source of much of the magnesium incorporated in the dolomite beds.

Table 14. Concentrations of methane (C_1), ethane (C_2), and propane (C_3) measured in gas pockets from Holes 723A and 723B.

Core, sample, interval (cm)	Depth (mbsf)	C_1 (ppm)	C_2 (ppm)	C_3 (ppm)	C_1:C_2
117-723A-					
5H-2, 18	38.48	778327	84	14	9265
6H-5, 34	52.74	799301	93	20	8595
7H-4, 117	60.68	487234	51	12	9572
8H-4, 110	71.40	864514	99	27	8732
9H-4, 25	80.15	819498	125	43	6556
11X-2, 75	97.05	383750	118	62	3252
13X-4, 39	118.99	451209	68	21	6635
14X-3, 30	127.10	117515	12	4	9793
15X-6, 8	140.98	653047	113	34	5779
17X-2, 73	155.03	616270	113	33	5454
19X-4, 64	177.24	619615	118	35	5251
20X-2, 105	184.35	632353	124	34	5099
21X-5, 20	197.60	555827	137	41	4057
22X-5, 71	207.81	550780	130	35	4237
23X-2, 35	212.65	494590	119	33	4156
24X-4, 127	226.17	430408	122	38	3528
25X-3, 115	234.25	571509	158	39	3617
26X-2, 6	241.36	403730	146	41	2765
26X-3, 23	243.03	171725	69	22	2489
27X-4, 44	254.34	166538	108	44	1542
28X-2, 48	261.08	430532	183	53	2353
29X-4, 104	274.24	563682	178	51	3167
30X-4, 66	283.46	241637	247	96	978
31X-5, 146	295.36	413737	156	46	2652
32X-5, 20	303.70	559190	223	66	2508
33X-4, 62	312.22	386984	119	31	3252
35X-3, 120	325.70	272376	182	60	2046
36X-5, 50	332.59	429494	252	81	1704
39X-4, 120	360.70	488516	253	73	1930
40X-4, 149	370.69	440110	305	94	1443
41X-2, 120	377.00	288194	193	60	1493
117-723B-					
6H-3, 17	46.07	983462	91	16	10807
10X-4, 100	87.10	884868	121	40	7313
13X-4, 145	116.25	821589	125	50	6573
16X-2, 145	142.15	11466	1		11466
18X-5, 40	165.00	810462	123	35	6589
20X-5, 50	184.40	306936	49	13	6264
22X-4, 95	202.75	149635	22	7	6802
25X-5, 120	233.40	665682	150	39	4438
27X-1, 95	246.55	338439	179	49	1891
33X-1, 146	314.46	58354	104	44	561
35X-2, 38	324.58	109688	115	45	954
38X-2, 20	353.60	332627	177	55	1879
40X-3, 30	374.60	219835	257	94	855
41X-4, 50	386.00	263462	257	114	1025
42X-3, 59	403.89	411146	240	75	1700

Note: Values are expressed in μL/L (volume gas/volume wet sediment.

Chlorinity

Interstitial water analyses show that chlorinity decreases markedly between the seafloor and about 150 mbsf, decreases more subtly between 150 and 250 mbsf, and is relatively constant below that depth (see "Inorganic Geochemistry" section, this chapter). This pattern is also revealed by the chlorine/hydrogen count rate ratio from the gamma spectroscopy tool (Fig. 47). The chlorine/hydrogen ratio is low and relatively constant from 390 to 255 mbsf, then rises at an accelerating pace from 255 mbsf to the shallowest measurements at 70 mbsf.

The chlorine/hydrogen log has two ambiguities not present in the interstitial water analyses: (1) it does not distinguish between pore water and bound water in clays, so the pattern could be caused by a downhole increase in clay mineral abundance, or (2) the pattern could be caused by a downhole decrease in hole diameter, with a constant low chlorinity of interstitial waters. However, the gamma-ray log shows no evidence of downhole clay enrichment, nor does the neutron porosity log show an uphole increase in apparent porosities. Thus, the broad trend shown by the chlorine/hydrogen log is probably a real indicator of relative chlorinities. High-frequency fluctuations on Figure 47 may reflect variations in porosity, bound water in clays, and organic matter rather than changes in chlorinity of pore waters.

The chlorinity/hydrogen log exhibits one important feature that was undetected in interstitial water samples: a substantial increase in the chlorinity/hydrogen ratio below 390 mbsf. The deepest interstitial water sample was at 385 mbsf; core recovery drops to very low values below 387 mbsf. The log-based chlorinity/hydrogen rise at the bottom of the hole should be considered tentative, because it is not confirmed by interstitial water samples and could conceivably be caused by an increase in hole diameter associated with higher-porosity sediments.

The lowest portion of the hole has very low grain densities (see "Physical Properties" section, this chapter), wet- and dry-bulk densities, and velocities as well as high porosities (Fig. 48 and "Physical Properties" section, this chapter). However, the decrease in these properties is not sudden at 390 mbsf; instead, a gradual downhole decrease begins at 352 mbsf (Figs. 44 and 45). Uranium and sulfur show sudden decreases at about 390 mbsf in agreement with the chlorinity/hydrogen rise, suggesting that water with an apparently higher chlorinity/hydrogen ratio is oxic.

The occurrence of dolomite stringers is not random throughout Site 723; instead they appear to be confined to the interval of lowest chlorinity/hydrogen ratios. We did not confidently identify any dolomite stringers above 221 mbsf in the region of rising chlorinity. A dolomite stringer does occur at 407 mbsf, within the region of the increasing chlorinity/hydrogen ratio; but it occurs exactly on a chlorinity/hydrogen trough to low baseline values. However, the wide spacing of dolomite stringers and the narrowness (28 m) of the measured zone of apparently increasing chlorinity makes any speculation about a lower limit to stringer formation tenuous.

In general, no correlation between the chlorinity/hydrogen ratio and the location of modern dolomite stringers is found within the long interval of low chlorinity/hydrogen. This apparent association of low present chlorinity/hydrogen ratios with dolomite stringers may be coincidental. Magnesium in interstitial waters decreases with depth and is too low to support much modern dolomite precipitation in the depth range containing dolomite stringers (see "Inorganic Geochemistry" section, this chapter).

Uranium Concentrations

Uranium concentrations at Site 723 are an order of magnitude higher than in most deep-sea sediments. Normally, the gamma-ray log, which detects the natural radioactivity of potassium, thorium, and uranium, is dominated by potassium in clays. In contrast, uranium accounts for about 80% of the total gamma radioactivity at Site 723, and uranium concentrations are predominantly about 5–10 ppm. Potassium and thorium tend to be positively correlated with aluminum, as is commonly the case, because variations in clay mineral abundance are usually larger than variations in clay mineral composition. However, the positive correlation between uranium and both thorium and potassium is weaker at Site 723 than in most other regions, and this correlation is not present in some portions of the hole. Clay minerals probably carry most of the potassium and thorium, but the majority of uranium is in a different component.

The component associated with the anomalously high uranium concentrations is probably organic matter. Other conceivable components with high uranium concentrations (phosphorite, zircon, magnetite, and biotite) are absent at Site 723 or are

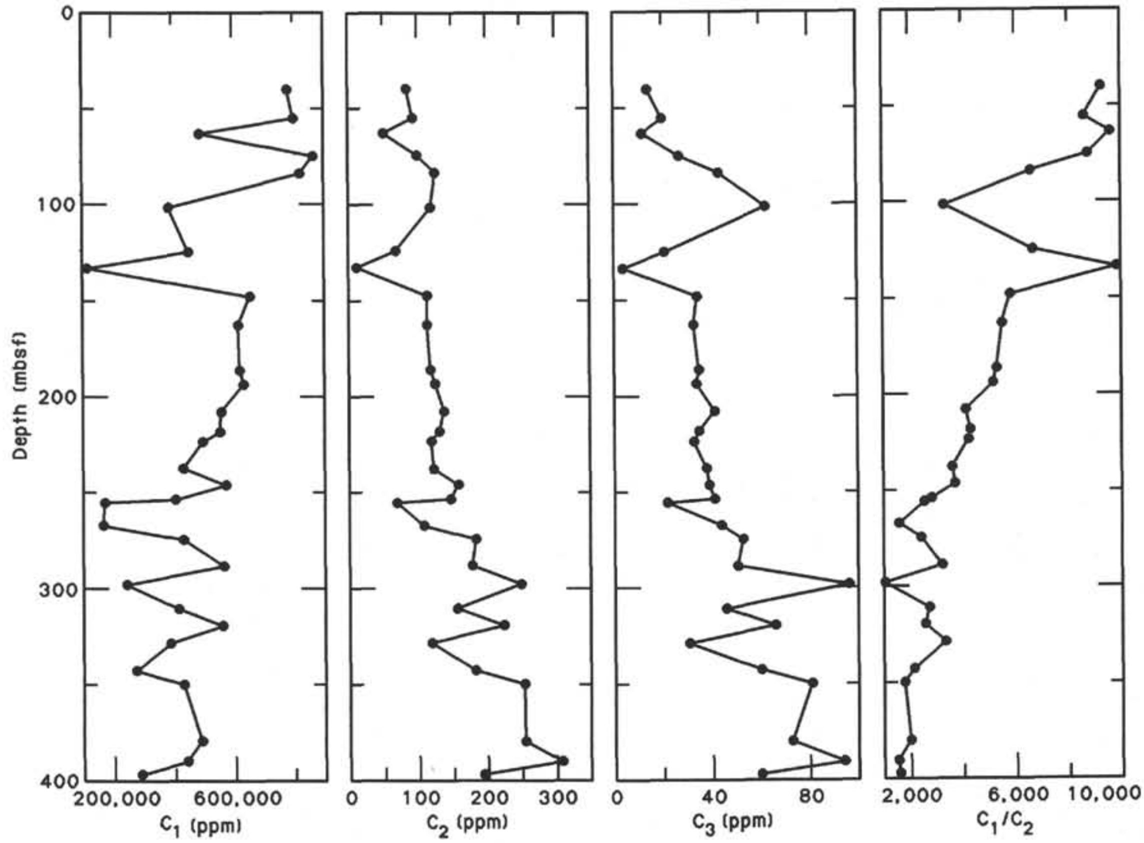

Figure 41. Downhole concentrations of methane (C_1), ethane (C_2), propane (C_3), and the C_1:C_2 ratio in gas pockets from Hole 723A.

Table 15. Organic carbon, $CaCO_3$, and U^k_{37} values of selected samples from Hole 723B.

Core, sample, interval (cm)	Depth (mbsf)	Organic carbon (%)	$CaCO_3$ (%)	U^k_{37}
117-723B-				
1H-1, 50-53	0.50	5.66	51.4	0.91
1H-2, 50-53	2.00	2.83	63.6	0.89
1H-3, 50-53	3.50	2.28	53.4	0.88
2H-1, 50-53	4.80	1.73	50.6	0.88
2H-1, 100-103	5.30	2.27	47.6	0.89
2H-2, 50-53	6.30	2.21	50.1	0.84
2H-2, 100-103	6.80	1.17	51.2	0.88
2H-3, 55-58	7.85	2.45	49.0	0.87
2H-3, 100-103	8.30	1.96	51.9	0.88
2H-4, 50-53	9.30	2.49	48.3	0.84
2H-4, 100-103	9.80	3.87	35.7	0.81
2H-5, 50-53	10.80	3.25	46.2	0.80
2H-5, 100-103	11.30	3.89	55.6	0.82
2H-6, 50-53	12.30	1.80	52.7	0.84
2H-6, 100-103	12.80	2.46	53.8	0.83
3H-1, 50-53	14.50	1.57	53.7	0.86
3H-1, 100-103	15.00	3.73	47.5	0.86
3H-2, 50-53	16.00	3.21	62.6	0.86

present in concentrations far too low to account for observed uranium concentrations. Phosphorite could be present in thin horizons in sufficient concentrations to affect the uranium log, but it is not pervasive enough to account for uranium variability. Uranium/thorium and uranium/potassium ratios are far too high for clay minerals.

In contrast, organic matter is very high at Site 723 (see "Organic Geochemistry" section, this chapter), and organic carbon is often found to be rich in uranium (Fertl, 1979). Figure 43 compares the core measurements of organic carbon percentages (see "Organic Geochemistry" section, this chapter) with the uranium logs. Considering the difficulty of correlating discrete measurements with a continuous log, the character correlation between the two data types is remarkably good.

It is surprising that the organic matter appears to be approximately constant in uranium concentrations, since the relationship between the two is not based on the primary uranium content of organic matter. Instead, it is based on preferential precipitation of uranium in the low-redox conditions associated with organic matter. The uranium spike at 18 mbsf, corresponding with the largest measured organic carbon percentage, occurs close to but not exactly at a 30-mbsf, very high spike in dissolved organic carbon. The peak in dissolved organic carbon is within the sulfate reduction zone (see "Inorganic Geochemistry" section, this chapter), and it is likely that the uranium concentration is still changing at these shallow depths.

In the interval from 100 to 175 mbsf, the uranium concentration exhibits a high-frequency oscillation, with a period of 5–10 m. This cyclical behavior has far too high a frequency to be detected with the discrete organic carbon measurements or correlated with these measurements. These uranium cycles are highly correlated with physical properties cycles (Figs. 44 and 49): uranium highs correspond to lows in bulk density, photoelectric effect, resistivity, and sonic velocity, and to highs in neutron porosity. This correlation is strongest in the interval from 100 to 150 mbsf, where uranium variations are largest, but a correlation between uranium and density clearly continues below 150

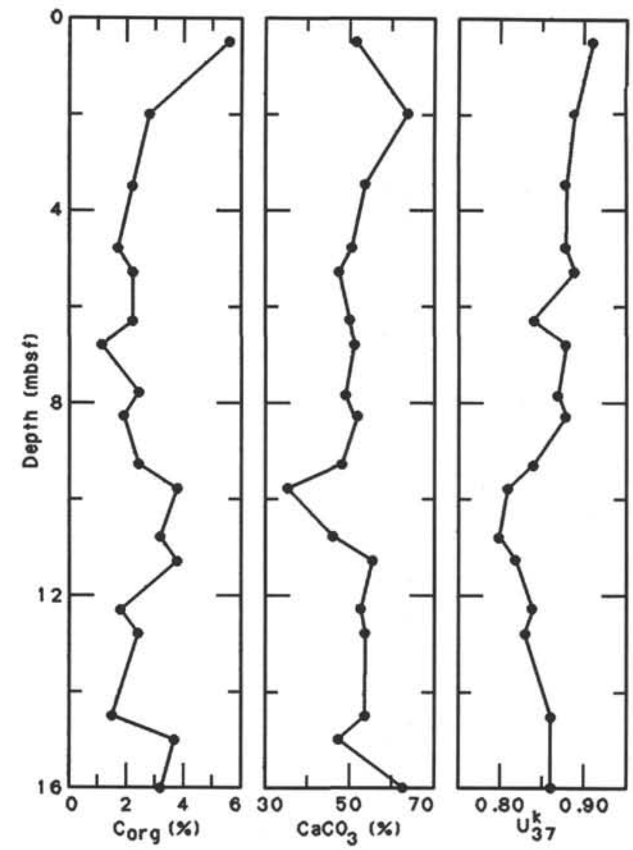

Figure 42. Downhole plot of organic carbon, $CaCO_3$, and the U^k_{37} index in sediment samples from Hole 723B.

mbsf. High organic matter accounts for both the anomalously low grain densities (see "Physical Properties" section, this chapter) and correlation of uranium with physical properties.

In contrast, clay content exhibits a poor correlation with both uranium and the physical properties logs above 145 mbsf, where the uranium fluctuations are highest in amplitude. Clay content often controls porosity variations and is indicated in Figure 49 by the potassium/thorium gamma-ray log. Only below 145 mbsf does the potassium/thorium log exhibit some correlation with uranium and physical properties. However, here too organic carbon fluctuations may be a more important source of physical property variations than is clay content. The correlation between potassium/thorium gamma ray and uranium in this lower interval of Figure 49 implies that the concentration of organic matter is higher in the clay-rich zones than in the carbonate-rich zones; this association is common also in other regions.

Although uranium variations at Site 723 are controlled primarily by variations in organic matter, a small amount of uranium must also be present in the clays. Based on typical uranium/potassium and uranium/thorium ratios for clay minerals (Fertl, 1979), about 1-3 ppm of uranium may be in the clays. As a result, the approximate doubling of average organic carbon concentrations below 200-220 mbsf is accompanied by an increase, but not a doubling, of uranium concentrations (Fig. 43).

Velocity, Density, and Porosity

The trends of velocity, density, and porosity with depth are anomalous in two respects: (1) lack of the normal compaction trends, and (2) velocity and density decrease below 352 mbsf. Of the three physical properties measured *in situ*, only velocity exhibits a compaction trend (Fig. 44). Excluding the dolomite stringers, velocities show an overall increase from 1.55 km/s at 100 mbsf to about 1.8 km/s near 350 mbsf. This compaction trend is substantially lower in velocity than empirical trends such as those of Hamilton (1979) and Carlson et al. (1986). Superimposed on this broad trend is substantial variability on scales of meters to tens of meters. Much of this velocity variability (Fig. 44) correlates well with uranium variations (Fig. 45) and is attributable to fluctuations in the concentration of organic matter.

Density and neutron porosity exhibit no evidence of a compaction trend between 100 and 352 mbsf. Except for fine-scale variability correlated with uranium fluctuations, density is virtually constant and neutron porosity actually increases slightly downhole. The neutron porosity undergoes a baseline shift upward at about 200-220 mbsf, the same depth interval at which organic carbon percentage undergoes a baseline shift to almost double the average amount from 100 to 200 mbsf (see Fig. 43 and "Organic Geochemistry" section, this chapter). The photoelectric effect, which is relatively insensitive to porosity, closely parallels the neutron porosity fluctuations (except in dolomite stringers), indicating a compositional control on neutron porosity variations. Again, organic matter is the likely cause: the higher neutron porosities are probably due as much to high bound water in organic matter as to high pore volume.

The lack of any evidence of compaction in porosity and density trends is both important and puzzling, particularly in light of the subdued compaction trend of the sonic log. Further, density is far lower, and porosity is higher, than is normal for any lithology (Hamilton, 1976). The very high rate of sedimentation at this site would account for some retardation of compaction, but porosities are high enough to imply sufficient permeability for some compaction.

To our knowledge, greatly undercompacted sequences are found in only two environments: deltas and accretionary prisms. In deltaic environments such as the U.S. Gulf Coast, the combination of extremely high sedimentation rates and high clay contents (relatively low permeability) results in underpressured zones. In these zones, overburden-related compaction is retarded at the lowest permeability zones, resulting in a sudden downward increase in porosity. In accretionary prisms, undercompacted sediments are caused by pervasive fluid flow from below associated with subduction (e.g., ODP Leg 110).

The undercompaction at Site 723 is more similar to the gradual porosity profiles of accretionary prisms than to the sudden porosity increases of overpressured deltaic sediments. Therefore, our preferred interpretation is that compaction is retarded by fluid replenishment. Unlike the replenishment from below that occurs in accretionary prisms, the flow at Site 723 may be from either below or subhorizontally. The geochemistry of pore fluids suggests a deeper source of sulfate-enriched and chloride-depleted sediments (see "Inorganic Geochemistry" section, this chapter). We cannot completely exclude the Gulf Coast analog, because clay variability is subtle and conceivably permeability is relatively uniform.

Below 355 mbsf, porosity increases and velocity, density, and resistivity decrease to very low values for such depths. This zone could be an overpressured zone. However, several observations suggest a different interpretation. First, chlorinities are higher than in the overlying sediments (Fig. 47); thus, this zone cannot be the source of hydraulically pumped brackish water or the cause of undercompaction in the overlying sediments. Second, the sharp top of this zone at 355 mbsf, though relatively high in density and low in porosity, corresponds with lows in Al_2O_3, K_2O, and thorium (Fig. 46) and is therefore unlikely to be an impermeable clay. The very high Pe of 3.3 is consistent with dolomite, but the neutron porosity of 70% would appear to pre-

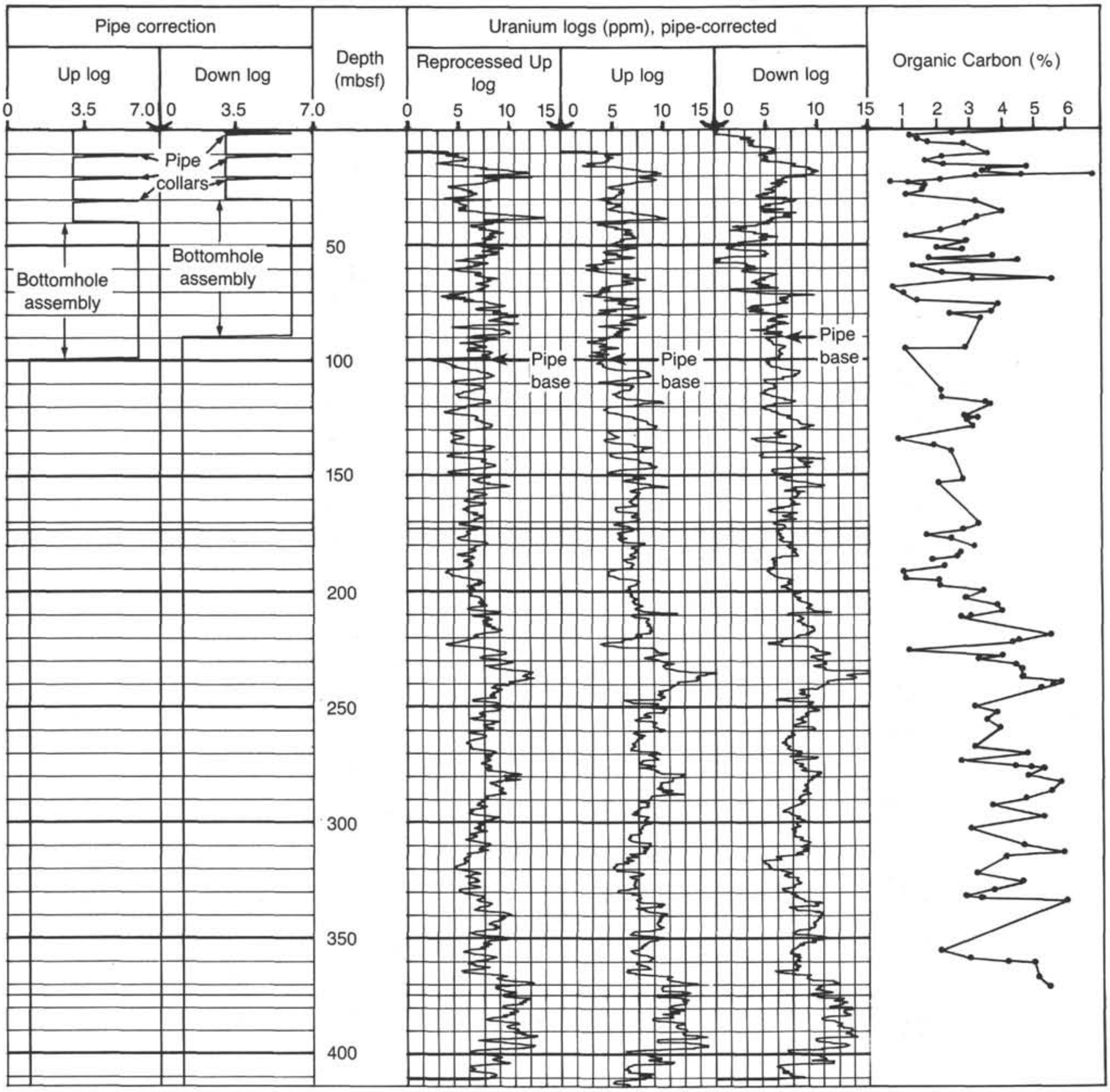

Figure 43. Comparison of organic carbon percentage measured on core samples with logs of uranium concentration. The three uranium logs shown are reprocessed upcoming (left), original upcoming (center), and original downgoing (right) logs.

clude impermeable dolomite. Third, Pe drops dramatically beneath 355 mbsf, indicating that this high-porosity zone is compositionally distinct from overlying sediments (except perhaps for the Pe peaks).

Siliceous microfossils are the most likely explanation of the high-porosity, low-velocity, low-density zone at the bottom of Site 723. Comparable low velocities and high porosities were observed in diatom oozes at shallower depths at ODP Site 647 (Arthur, Srivastava, et al., 1987). Core recovery below 387 mbsf is too low for quantitative estimation of representative siliceous microfossil abundance, and this recovery probably is heavily biased toward the more compacted clay interbeds. Of four cores recovered below 387 mbsf from Holes 723A and 723B, three are only a few centimeters long and are composed of clay or limestone, and one is 5 m long and composed of diatomaceous shale (see "Lithostratigraphy" section, this chapter).

Grain densities decrease substantially in this zone (see "Physical Properties" section, this chapter) to values consistent with that of opal. Further, Pe decreases to a value appropriate for pure opal in some portions of this zone. Very high levels of dissolved silica are present in the deepest interstitial water sample, at 385 mbsf (see "Inorganic Geochemistry" section, this chapter), but core recovery precluded interstitial water sampling below 387 mbsf. At about the depth of this water sample, a diatomaceous clay layer is identified in both Holes 723A and 723B (see "Lithostratigraphy" section, this chapter) and a siliceous bed is evident in log responses around 384–385 mbsf (Fig. 48).

Based on log responses, siliceous microfossil abundance is quite variable below 380 mbsf (Fig. 48). At the bottom of the hole, immediately below the lowest dolomite stringer, the log responses are quite sinusoidal, with a period of 3.3 m. This log response is not an artifact, as it is evident and correlatable in the

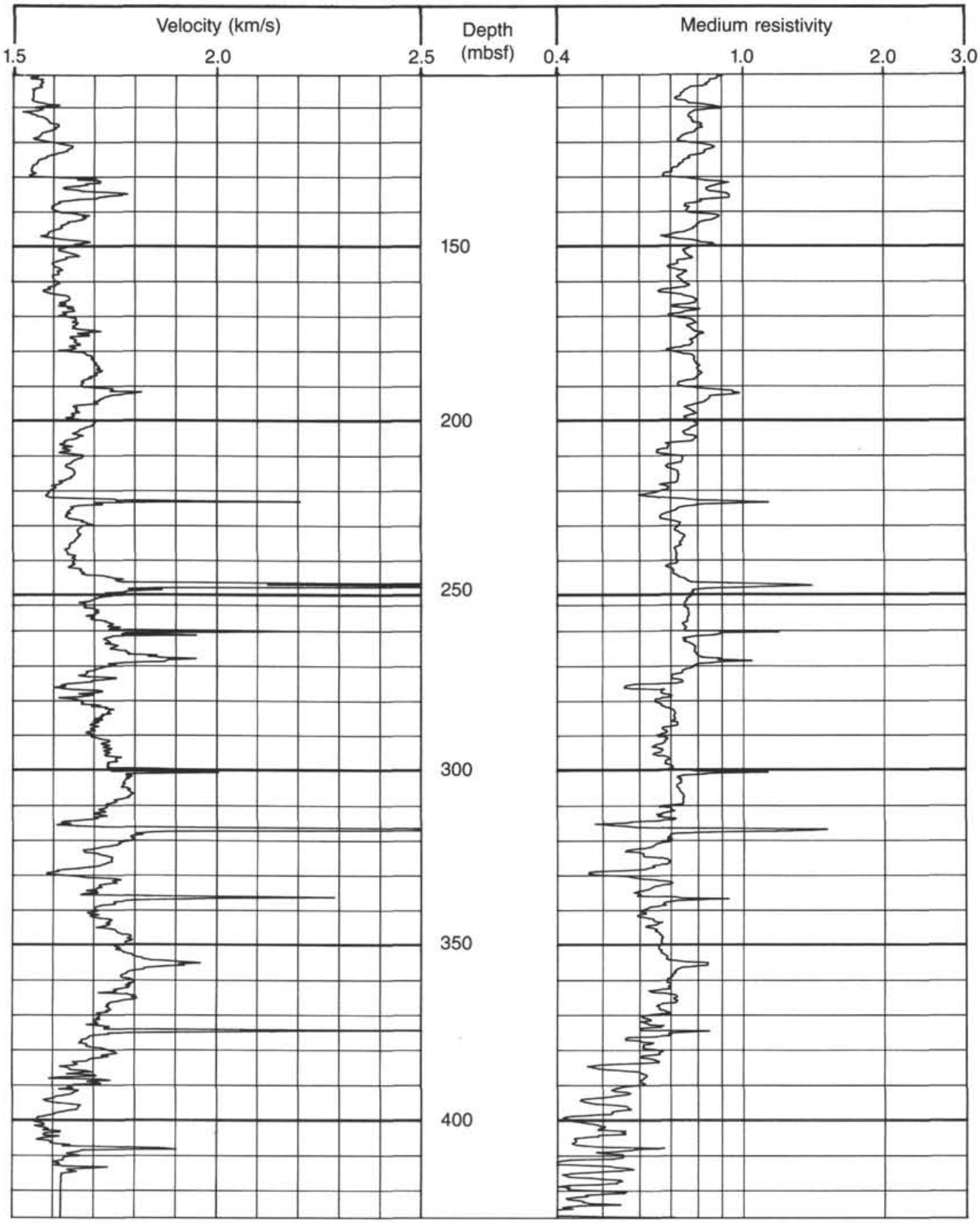

Figure 44. Velocity and resistivity logs. The spikes are interpreted to be dolomite stringers.

lowest logging tool of every logging run. Unfortunately, this zone is so near the bottom of the hole that the length of each tool string prevented all but the bottom tool from sampling this zone. Based on the very low density and Pe of 1.7 for the troughs in log response, the troughs are nearly pure siliceous ooze (Pe = 1.7).

The probable cause of the disappearance of core recovery below 387 mbsf is evident in Figure 48: very soupy sediments (except for the dolomite stringer), more appropriate for an APC core catcher than for an XCB. Neither core recovery nor the number of logs permits accurate determination of the mineralogy of the peaks below 411 mbsf (Fig. 48). The increases in Al_2O_3 and SiO_2 below 380 mbsf (Fig. 46), with Fe_2O_3 and K_2O, suggest that palygorskite may be the dominant clay mineral below 380 mbsf. Both palygorskite and opal may be indicators of high monsoon intensity.

Hole Deviation and Downhole Magnetics

The Schlumberger GPIT tool measures acceleration, hole deviation, and magnetic moment. At Site 723, this tool was included in two tool strings: the lithoporosity combination (Run #2) and the geochemical combination (Run #3). Because Run #2 obtained both downgoing and upcoming logs, a total of three openhole passes with the GPIT was obtained.

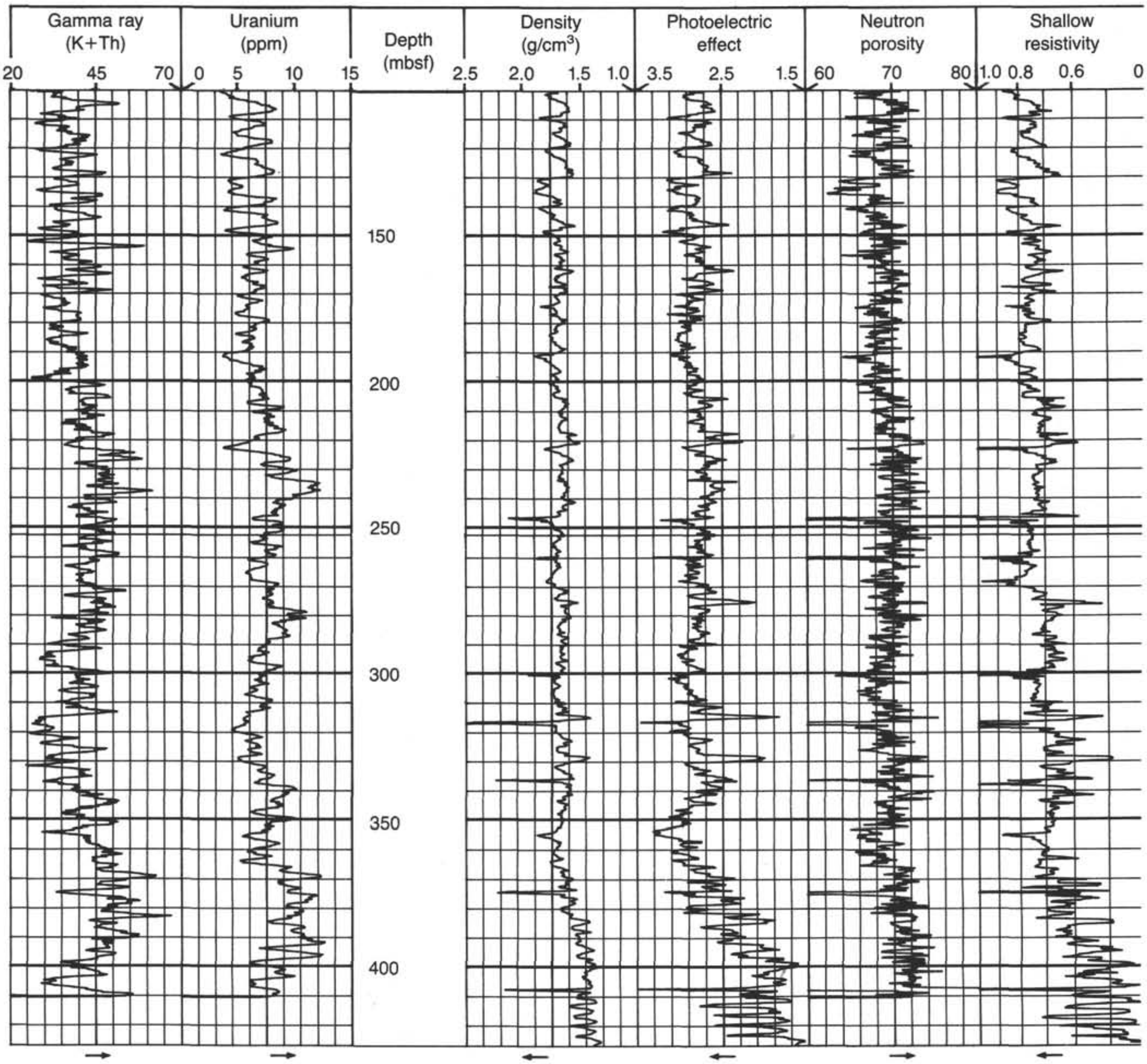

Figure 45. Comparison of physical properties logs (density, photoelectric effect, neutron porosity, and shallow-focused resistivity) with two indicators of components that can control these properties. Clay content, as indicated by the potassium + thorium (CGR) log, shows much lower correlation with physical properties than does uranium concentration, an indicator here of organic matter variations.

The two deviation surveys of Run #2 were quite consistent (Fig. 50). Borehole deviation increases gradually from a 1° tilt to the southeast at 100 mbsf to a 2.5° tilt to the east at 400 mbsf. These deviations are too small to have a significant effect on any interpretations (including paleomagnetism) in this report. A slight difference between the downgoing and upcoming surveys of Run #2 occurs in the interval 210–310 mbsf (Fig. 50). In the downgoing log, a temporary 0.6° deviation excursion begins at the 244-mbsf dolomite stringer, and in the upcoming log a similar 0.3° excursion begins at the same point. These excursions are minor in their impact on the measurement of hole deviation, but they are more significant for the subsequent interpretation of downhole magnetics.

The Run #3 deviation survey also shows the gradual increase from 1° to 2.5°, but azimuth control is poor. Unlike Run #2, which is pressed against the borehole wall by bowsprings, Run #3 is free to wobble in the borehole. Temporary deviation excursions are common in this log, occurring when the GPIT portion of the toolstring is 4 m above a dolomite stringer (Fig. 50). This correlation can be seen by comparing locations of double-peaked excursions with locations of dolomite stringers, as indicated by the signal strength (CSIG) log obtained on the same logging run.

The three perpendicular fluxgate magnetometers used for measuring azimuth of deviation can also be used to calculate total moment (in oersteds) and magnetic inclination. The three logs of total moment indicate that the magnetic field of the tool string is quite different for Run #2 than for Run #3. Furthermore, the tool-deviation excursions noted in Figure 50 are echoed by magnetic-moment excursions. This similarity indicates that

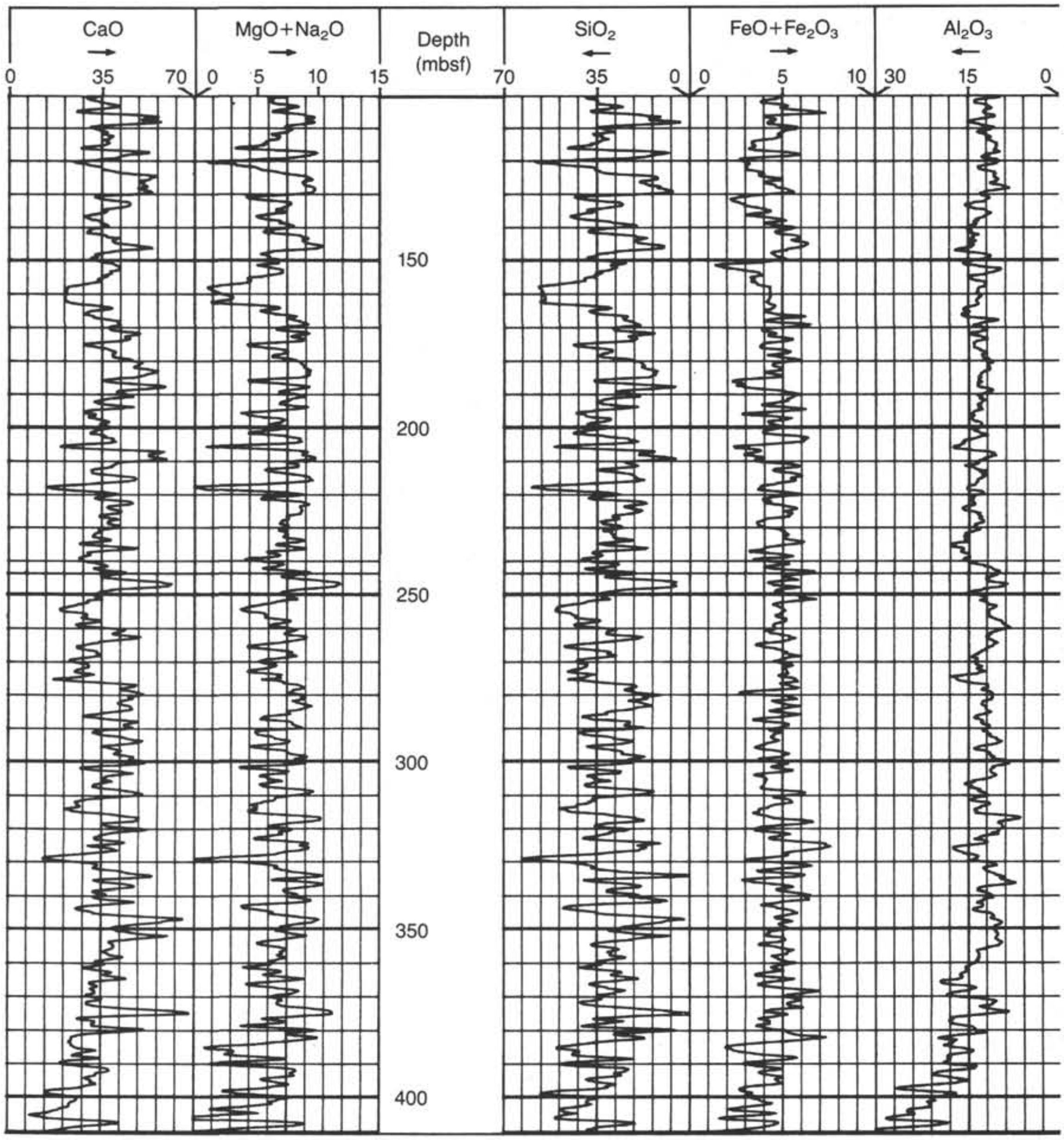

Figure 46. Elemental concentration logs based on reprocessing of geochemical logs. Most logs (CaO, MgO + Na_2O, SiO_2, Fe_2O_3, Al_2O_3, K_2O, and TiO_2) are expressed as oxide dry-weight percentages. Sulfur is in dry-weight percentage. Trace elements (gadolinium, thorium, and uranium) are in wet-volume percentage.

although the total measured moment is usually a constant vector sum of the earth's magnetic field and logging tool, tool tilt changes the magnitude of this vector sum.

Like total moment, magnetic inclination (Fig. 51) is dominated by the vector sum of the earth's and tool's magnetic moments; thus, the horizontal scale in Figure 51 is different for Run #3 than for Run #2. The character of the three inclination records is very similar, except for an obvious excursion at 244–303 mbsf in downgoing Run #2, associated with the same collision of the logging tool with a dolomite stringer that was detected in Figure 50. A second collision at the same horizon during the upcoming log is subtler in its magnetic effect, detectable at 244 mbsf only by comparison with Run #3.

The depth-coherent character of the three logging runs strongly suggests that the variations in magnetic inclination are caused by variations in magnetization of the sediments. The sediment magnetization variations could be associated with induced magnetization, viscous remanent magnetization, or magnetic reversals. Although shipboard paleomagnetic analyses to date have not included estimation of the relative magnitudes of these three components, induced magnetization is always much larger than remanent magnetization in deep-sea sediments.

INTERHOLE CORRELATION

Here we provide detailed interhole correlations in the upper 80 m of the drilled sediments at Site 723. The upper interval has an age range from 0 to 0.5 Ma and is characterized by cyclic changes in the nature of sediments that can be identified by visual observation and by variations of magnetic susceptibility and $CaCO_3$ content. Correlation of the sedimentary cycles of layers among these holes provides valuable information on the relative rate of sedimentation, which is necessary information for any

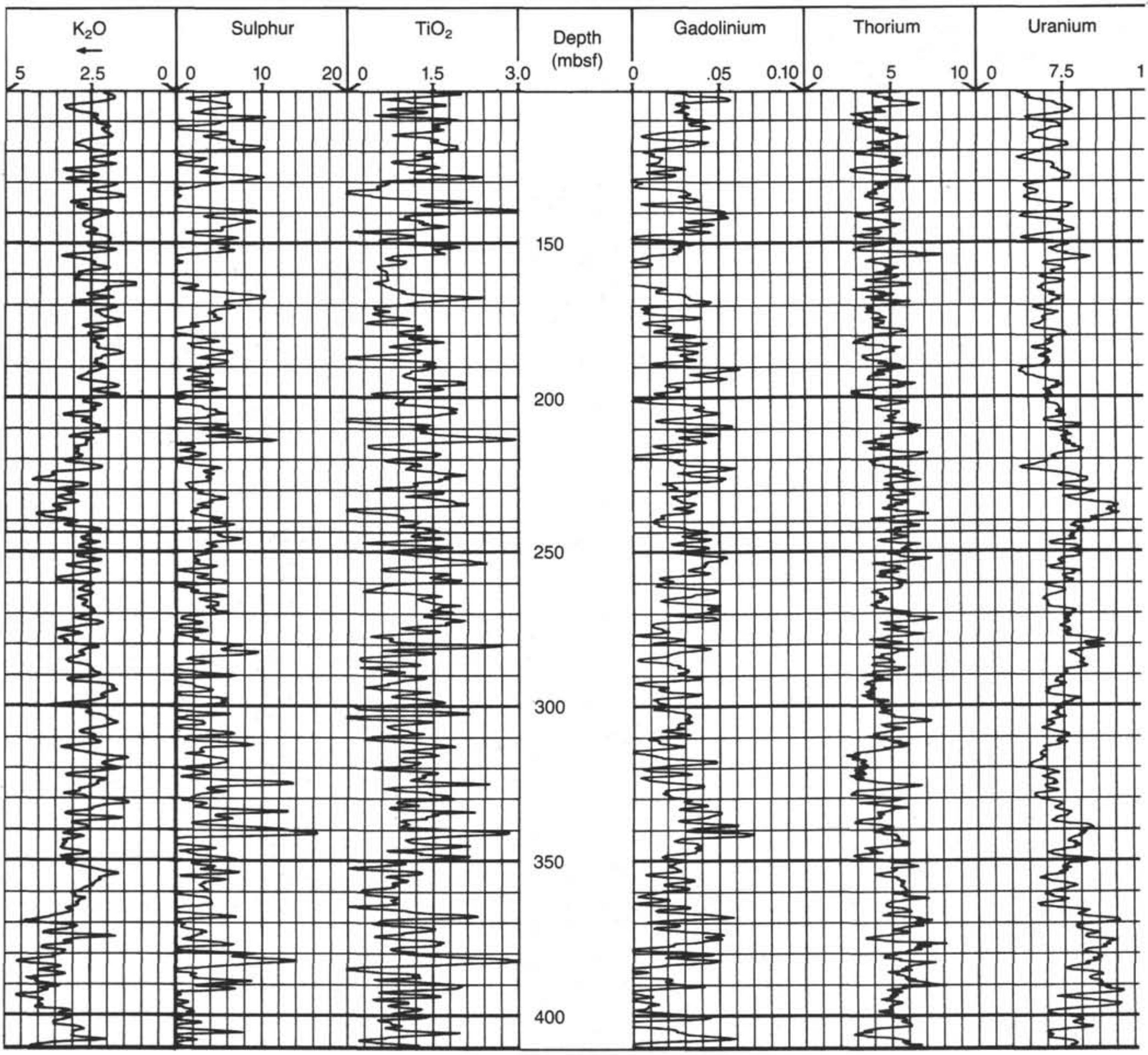

Figure 46 (continued).

high-resolution study of depositional environments. The essence of the correlation process is outlined in the "Explanatory Notes" chapter (this volume).

Hole-to-hole correlations were made on the basis of visual identification of distinctive layers, which were then verified using physical property and magnetic data. The magnetic susceptibility was measured at 10-cm intervals on whole-core sections. Photographs were then taken of the split cores.

The visual correlation of the cores relied primarily on the core photographs. We determined 23 distinct and traceable layers in the upper 80-m interval of the correlatable sedimentary sequence at Site 723 and notated them as OM-a_1, . . . , h_3, and h_4. The letter code (i.e., a, b, c, . . . , etc.) refers to the sequence of cores, and the number code indicates the number of marker layers in each core. For example, the notation "a_2" corresponds to the second marker layer defined in Core 117-723A-1H, and "b_1" denotes the first marker layer in Core 117-723A-2H. The marker layers a_1–h_4 were defined on the cored sediments of Hole 723A above 78.75 mbsf. In order for a marker layer to be defined as such it had to meet the following criteria: the layer must be distinct enough to trace in the sedimentary sequence of the other holes and its character must not change. Useful criteria for recognizing markers are color boundaries, distinctly colored layers, the shape of bioturbation, and the sequence of color changes in the surrounding sediments.

Figure 52 shows the magnetic susceptibility curve and positions of individual, visually correlatable layers. The pattern of the susceptibility and the positions of layers match very well. The stratigraphy of the magnetic susceptibility data and the visually identified layers are extremely consistent in that a particular visually characteristic layer always coincides in depth with a distinct feature in the magnetic susceptibility curve. In this way the lithologic correlations could be verified using the magnetic susceptibility data, which are quantitative. The reliability of the correlations is great; the accuracy of correlation is bounded by the magnetic susceptibility measurement interval (10 cm).

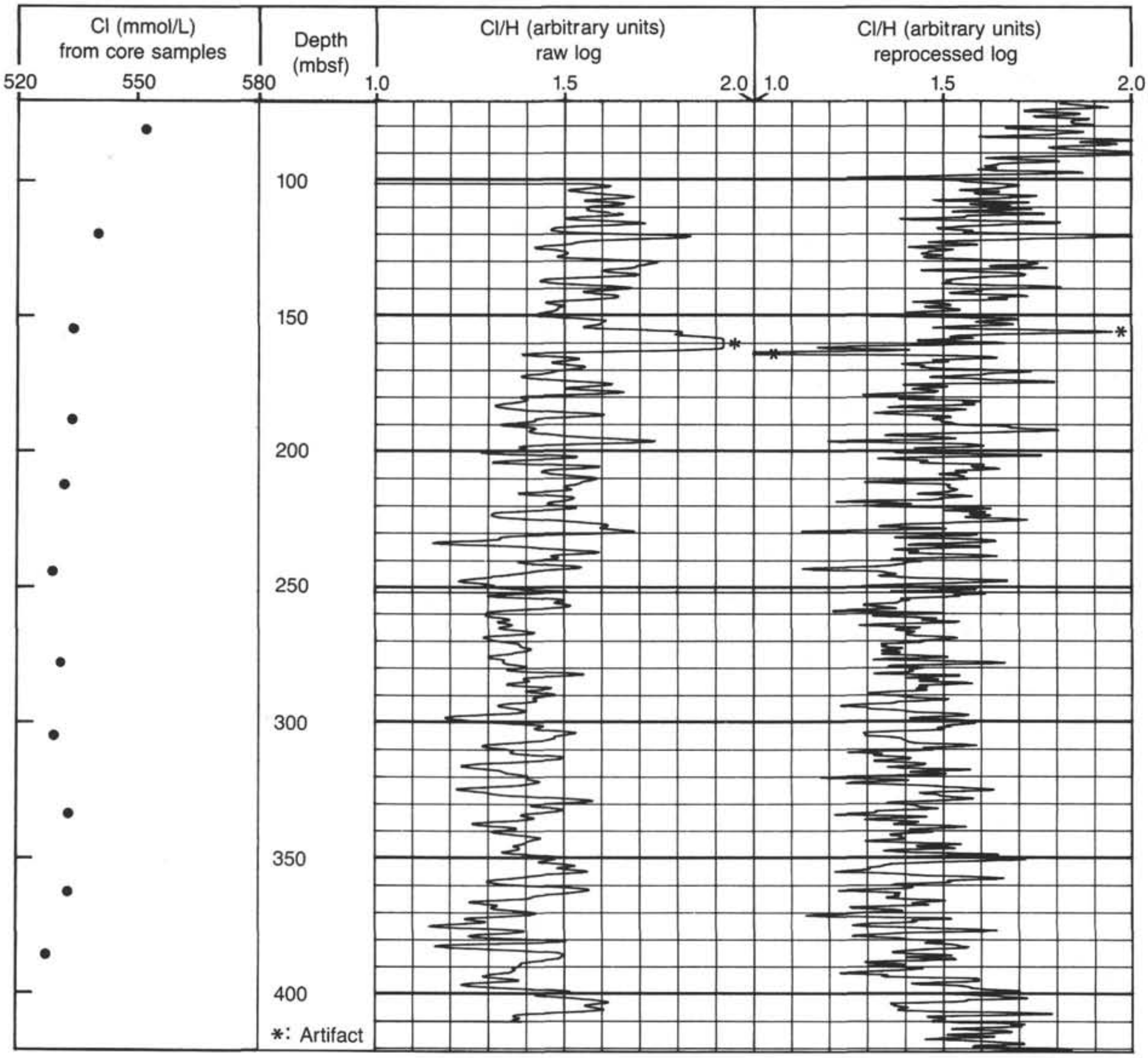

Figure 47. Comparison of chloride concentrations of interstitial water samples with logs of the relative abundance of chlorine to hydrogen. The log at left is reprocessed and the log at right is the original shipboard log. Asterisks indicate spikes interpreted to be artifacts. Note the low chlorinity zone from 150 to 390 mbsf.

The results of the layer-by-layer correlation allow us to calculate true thickness between the layers that coincide with and are separated by core boundaries (Fig. 53). Occasionally, core tops were expanded by water uptake during drilling. In this case, the apparent thickness of the disturbed sediment layer is observed to be thicker than the original thickness. In some instances, the top part of the core was missing; in this case apparent thickness is observed to be thinner than the original thickness. Fortunately, the two holes were staggered in depth, so that they have different horizons at core boundaries (Table 16).

The original thickness of layers coinciding with core tops or bottoms can be obtained by comparing the thicknesses of correlative layers in the continuous sections of other holes. The calculation of the amount of the difference can be achieved by the differences in the ODP depths of marker layers between holes ("723B - 723A ODP" in Table 16). Table 17 gives the differences between the depth (mbsf) calculated by the ODP CORELOG data and the corrected depth (mbsf) calculated by the layer-by-layer correlation method. This method can be applied for the cored sediments, which keep their original thickness within the cored interval. Because cored sediments at Site 723 do not keep their original thickness due to gas expansion below 35 mbsf, we cannot provide either the corrected depth or the precise thicknesses between the marker layers below the gas expansion horizon.

SUMMARY AND CONCLUSIONS

Site 723 is located in the northwest Arabian Sea on the continental margin of Oman and corresponds to the central drilling target of a depth transect of sites across the Oman margin. The transect brackets water depths ranging from 300 to 1500 m that correspond to the vertical extent of a pronounced mid-water oxygen-minimum zone. Site 723 is located in the center of a slope basin formed by a narrow halfgraben in what is presumed to be ophiolitic basement. Biogenic material produced by coastal upwelling and eolian detritus are deposited here at high rates (on average 175 m/m.y.). The sediments were expected to record

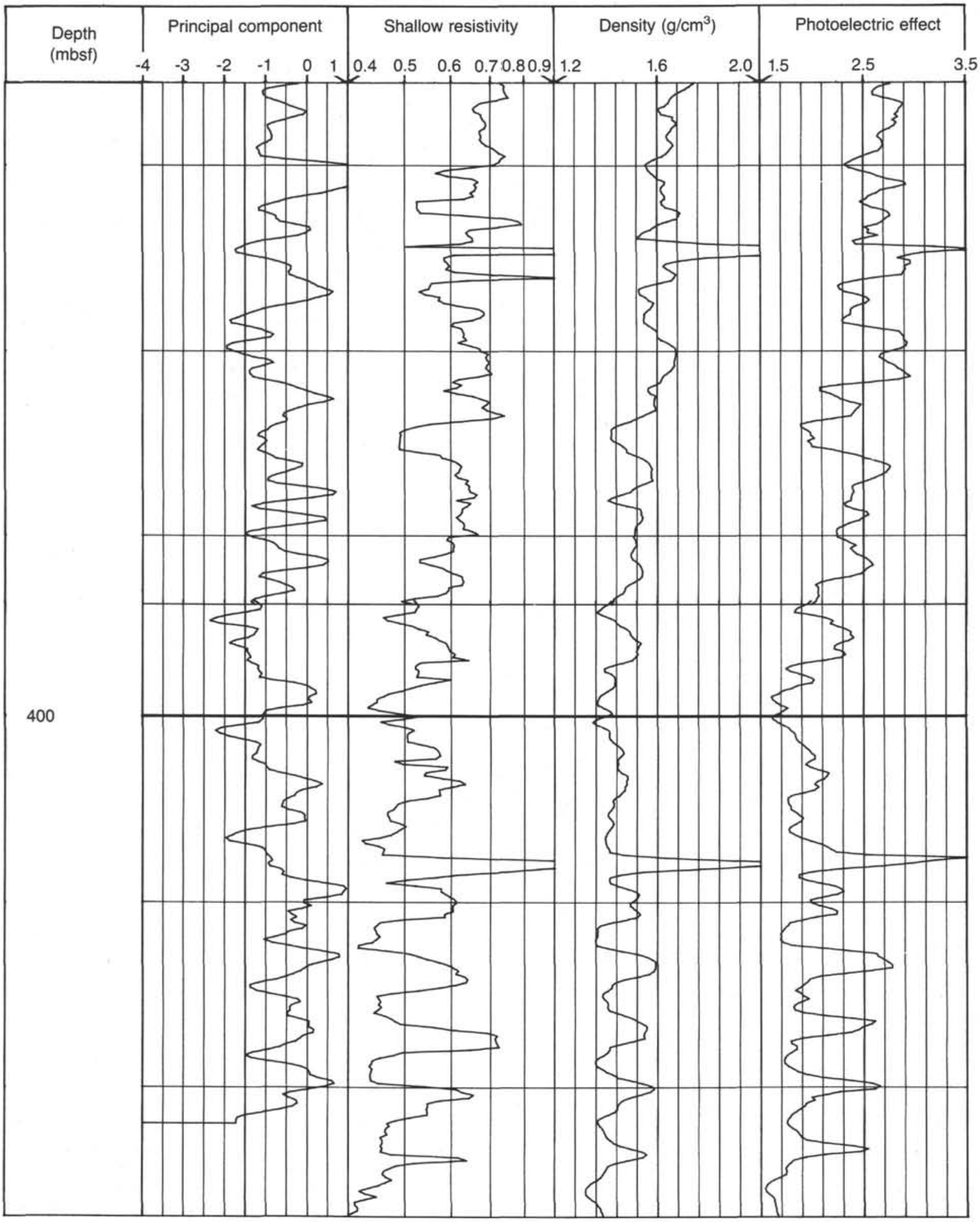

Figure 48. Four logs of the bottom portion of Site 723. The left log is the first principal component of the raw elemental counts from the gamma spectroscopy tool; deflections to the right correspond to high silicon and iron and low calcium.

changes in sedimentation and oceanographic/atmospheric circulation in considerable detail due to impeded benthic activity. The intention of Site 723 was to sample these continuous and expanded sections of upper Neogene to Holocene sediments.

Some of the major findings at Site 723 are summarized in Figure 54 and include the identification of:

1. Laminated, opal-rich facies of late Pliocene and early Pleistocene age. The laminations are interpreted to indicate a lack of bioturbation.
2. Dolomite stringers within the hemipelagic sequence.
3. High accumulation rates (175 m/m.y.) with detrital calcite as an important component.

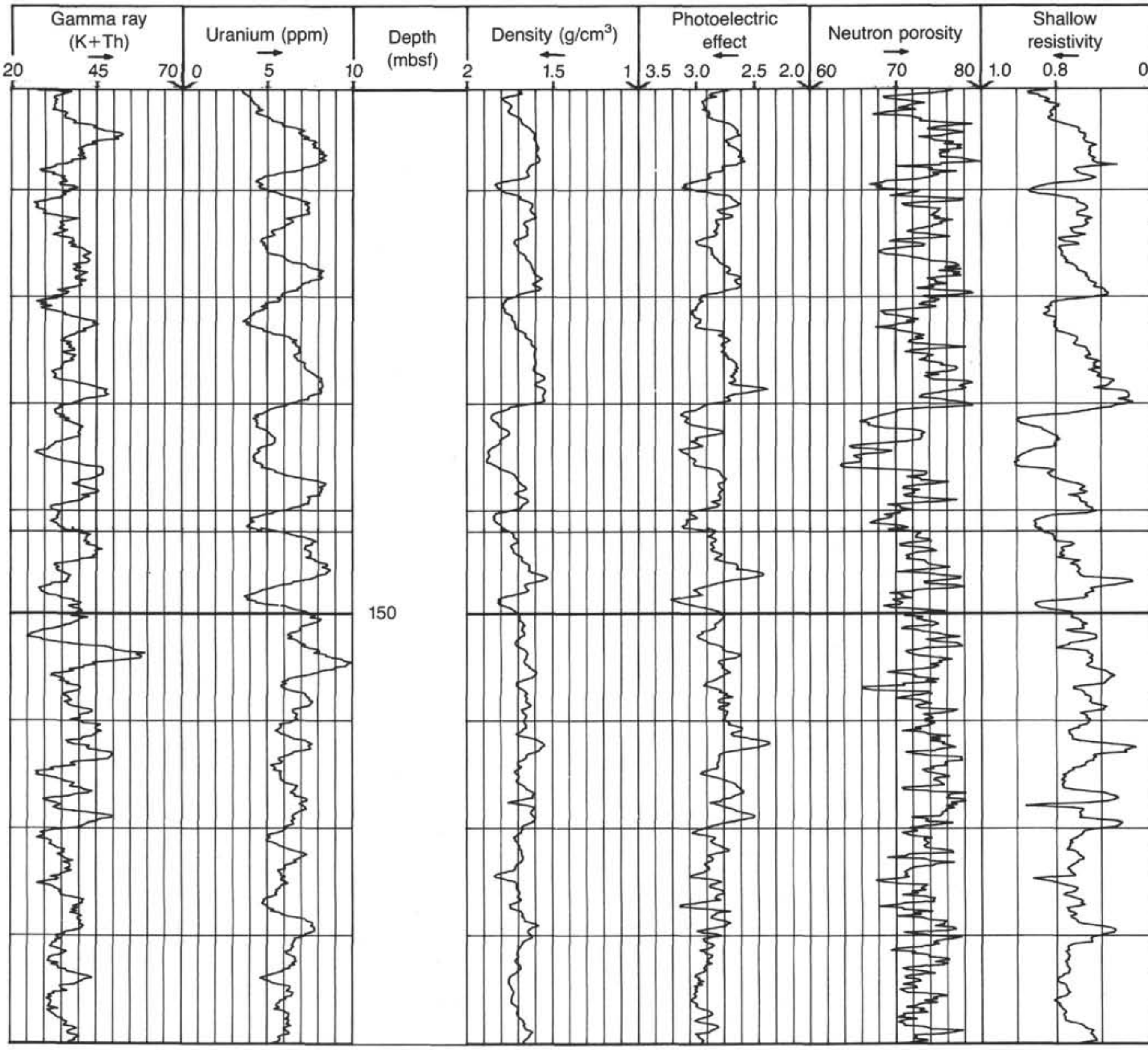

Figure 49. Expanded version of Figure 45, focusing on the top portion of the openhole interval. Note that physical properties logs at right are controlled by a component rich in uranium, not by clay content (gamma-ray log).

4. High accumulation rates of marine organic carbon, especially in the upper Pliocene and lower Pleistocene.
5. Rapid and complete sulfate depletion by 50 mbsf but increasing sulfate farther downsection and a continuous alkalinity increase from surface values of 10 mmol/L to values of about 100 mmol/L at 380 mbsf.
6. An increase in chloride in pore waters near the base of the core.
7. Abundant methane with traces of ethane and propane indicating thermogenic cracking at depth.
8. Distinctive variations of magnetic susceptibility and physical properties that define specific periodicities that can be correlated to the Owen Ridge.

The section penetrated at Site 723 ranges from upper Pliocene (NN18) to the Pleistocene and Holocene. Age control was achieved mainly from calcareous nannoplankton and paleomagnetic horizons. Only one lithologic unit was recognized at Site 723, but it has three distinctive facies.

A nannofossil ooze facies (I), which constitutes more than 99% of the section at Site 723, is green to olive green, foraminifer-bearing, marly, nannofossil ooze and calcareous clayey silt. The calcium carbonate and organic carbon contents of this facies vary between 40% and 70% and 1% and 7%, respectively. Planktonic foraminifer species indicate that monsoonal upwelling was persistent throughout the recovered section. During this interval, nannofossil diversity is low and opal is rare to absent in this facies (Fig. 54). Accumulation rates of carbonate and noncarbonate are consistently high, ranging from 5 to 15 g/cm²/k.y. (Fig. 24), but they are greatest in the upper Pliocene and lower Pleistocene. The rates of accumulation of organic carbon are likewise high, ranging from over 900 mg/cm²/k.y. in the upper Pliocene and lower Pleistocene to an average of about 500 mg/cm²/k.y. in the middle and upper Pleistocene. Both mag-

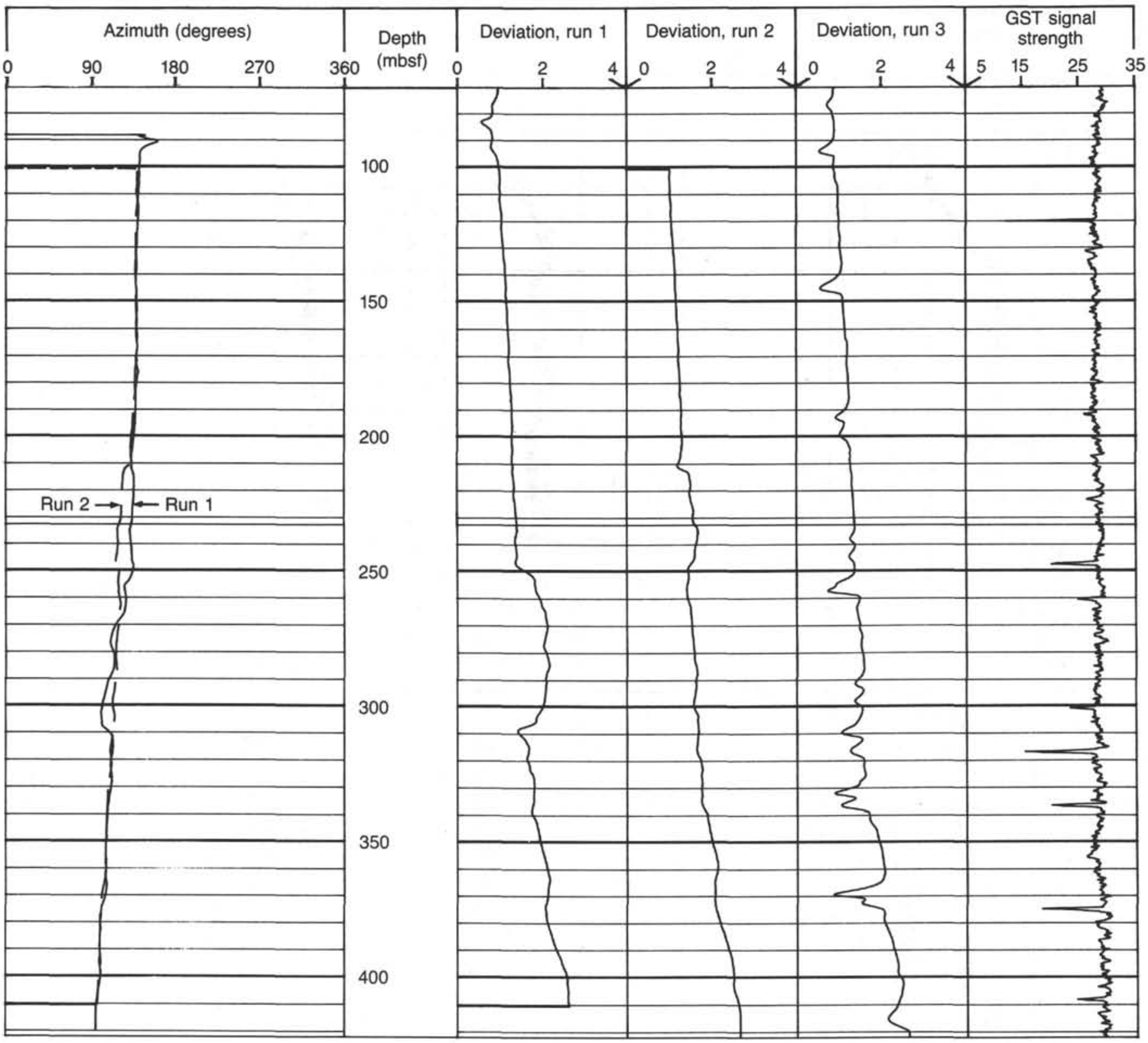

Figure 50. Replicate logs of borehole deviation from vertical and of deviation azimuth, and location of dolomite stringers as indicated by GST signal strength.

netic susceptibility and downhole logs show cyclic variability that probably reflects climate-related changes in the depositional system dominated by upwelling and eolian input. This facies is the hemipelagic background at Site 723, and its rate of accumulation reflects the subsidence of the slope basin as well as the pelagic and terrigenous input.

A dolomite facies (II) consists of occasional cemented beds and stringers of almost pure dolomite that range in color from pale green to olive green. The beds contain foraminifer molds and tests and preserve soft-sediment burrows and primary laminations. Seven dolomite layers, ranging from 5 to 30 cm in thickness, were recovered between 260 and 420 mbsf and two more were identified in the downhole logs. Several of the dolomite layers preserve fine-scale laminations.

A laminated facies (III) consists of beds of parallel laminae which individually are 0.1–1 mm thick. This facies is most frequent in the upper Pliocene, but it is rarely observed in beds exceeding a few centimeters in thickness. Light-colored laminae are accumulations of nannofossils or diatoms and dark-colored layers are organic-rich clayey silt. The occurrence of opal at Site 723 is largely coincident with the laminated facies. The nannofossils in this interval are thought to be indicative of cold water and upwelling. Monospecific assemblages of nannofossils and diatoms in some light laminae suggest that they were produced during blooms of relatively short duration (< 1 yr) and that bioturbation was inhibited, possibly due to complete oxygen depletion in the deeper-water column. High accumulation rates of organic carbon are characteristic of, but not limited to, the laminated facies (Fig. 54). In addition, the laminated facies often occurs in close association with the dolomite facies (Fig. 54).

The chemical composition of the interstitial waters and gas supports the notion that diagenetic cementation of dolomites is related to an unusual hydrologic regime in the subsurface of the slope basin penetrated at Site 723. Alkalinity reached a maxi-

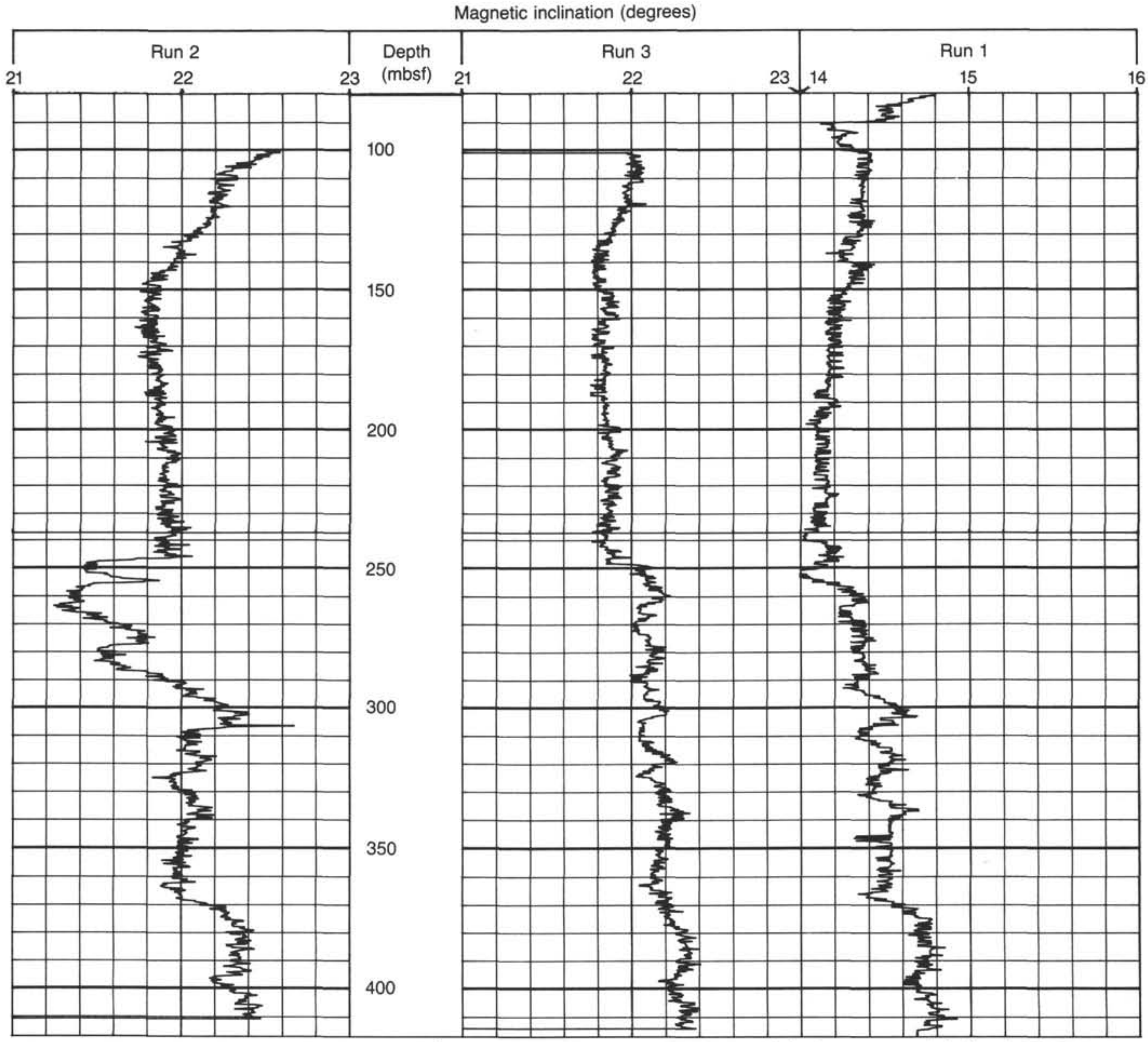

Figure 51. Three replicate logs of inclination of total measured magnetic moment. Note the correlation between runs in inclination character (except for the excursion in downgoing Run #2), indicating detection of sediment magnetization.

mum of >100 mmol/L at total depth (Fig. 54), which appears to be associated with severe degassing (apparently of CO_2) and core expansion, while chlorinity decreased by 30 mmol/L. The reason for the unusually high and persistent increase in alkalinity and for dolomite precipitation below 260 mbsf is a concomitant increase in sulfate below the zone of sulfate depletion (Fig. 54). Profiles of sulfate, chloride, and calcium, as well as magnesium, are attributed to advective flow of fresh water that dissolved gypsum and anhydrite from an evaporitic source. The traces of ethane and propane also indicate that some thermogenic cracking must have occurred within the deeper parts of the margin, possibly below the suspected ophiolite thrusts.

Overall, Site 723 provides a high-resolution record of biotic, chemical, and sedimentologic variations associated with organic-rich sediments deposited under the influence of strong seasonal upwelling and generally low oxygen conditions.

REFERENCES

Arthur, M. A., Srivastava, S., et al., 1987. Site 647. *In* Arthur, M. A., Srivastava, S., et al., *Proc. ODP, Init. Repts.*, 105: College Station, TX (Ocean Drilling Program), 645-907.

Baker, P. A., and Burns, S. J., 1985. Occurrence and formation of dolomite in organic-rich continental margin sediments. *Am. Assoc. Petrol. Geol. Bull.*, 69:1917-1930.

Berggren, W. A., Kent, D. V., and Van Couvering, J. A., 1985. The Neogene: Part 2, Neogene geochronology and chronostratigraphy. *In* Snelling, N. J. (Ed.), *The Chronology of the Geological Record*, Geol. Soc. Mem. (London), 10:211-260.

Canfield, D. E., and Berner, R. A, 1987. Dissolution and pyritization of magnetite in anoxic marine sediments. *Geochem. Cosmochim. Acta*, 51:645-659.

Carlson, R. L., Gangi, A. F., and Snow, K. R., 1986. Empirical reflection travel time versus depth and velocity versus depth functions for the deep-sea sediment column. *J. Geophys. Res.*, 91:8249-8266.

Fertl, H. H., 1979. *Gamma Ray Spectral Data Assists in Complex Formation Evaluation*: Houston (Dresser-Atlas).

Hamilton, E. L., 1976. Variations of density and porosity with depth in deep-sea sediments. *J. Sedimentol. Petrol.*, 46:280–300.

________, 1979. Sound velocity gradients in marine sediments. *J. Acoust. Soc. Am.*, 65:909–922.

Haq, B. U., Hardenbol, J., and Vail, P. R., 1987. Chronology of fluctuating sea levels since the Triassic. *Science*, 235:1156–1167.

Johnson, D. A., and Nigrini, C. A. 1982. Radiolarian biogeography in surface sediments of the eastern Indian Ocean. *Mar. Micropaleontol.*, 7:237–281.

Kolla, V., Kostecki, J. A., Robinson, F., and Biscaye, P. E., 1981. Distribution and origins of clay minerals and quartz in surface sediments of the Arabian Sea. *J. Sedimentol. Petrol.*, 51:563–569.

Martini, E., 1967. Nannoplankton und Umlagerungserscheinungen im Persischen Golf und im nördlichen Arabischen Meer. *Neues Jahrb. Geol. Palaeontol., Monatsh.*, 10:597–607.

Moore, G. W., and Gieskes, J. M., 1980. Interactions between sediment and interstitial water near the Japan Trench, Leg 57, Deep Sea Drilling Project. *In* Scientific Party, *Init. Repts. DSDP*, 56, 57, Pt. 2: Washington (U.S. Govt. Printing Office), 1269–1275.

Nigrini, C. A., 1968. Radiolaria from eastern tropical Pacific sediments. *Micropaleontology*, 14:51–63.

Perch-Nielsen, K., 1984. Cenozoic calcareous nannofossils. *In* Bolli, H., Saunders, J., and Perch-Nielsen, K. (Eds.) *Plankton Stratigraphy*: Cambridge (Cambridge Univ. Press), 427–554.

Sato, T., Takayama, T., Kato, M., Kudo, T., and Kameo, K., in press. Calcareous microfossil biostratigraphy of the uppermost Cenozoic formations distributed in the coast of the Japan Sea. Part 4: Conclusion. *Sekiyu Gijutsu Kyokaishi.*

Shimmield, G. B., and Price, N. B., 1984. Recent dolomite formation in hemipelagic sediments off Baja California, Mexico, *In* Garrison, R. E., Kastner, M., and Zenger, D. H. (Eds.), *Dolomites of the Monterey Formation and Other Organic-Rich Units*, Pacific Section S.E.P.M., 41:5–18.

Suess, E., von Huene, R., et al., 1988. *Proc. ODP, Init. Repts.*, 112: College Station, TX (Ocean Drilling Program).

Takayama, T., 1972. A note on the distribution of *Braarudosphaera bigelowi* (Gran and Braarud) Deflandre in the bottom sediments of Sendai Bay, Japan. *Paleontol. Soc. Japan, Trans. Proc. N. S.*, 87:429–435.

Takayama, T., and Sato, T., 1987. Coccolith biostratigraphy of the North Atlantic Ocean, Deep Sea Drilling Project, Leg 94. *In* Ruddiman, W. E., Kidd, R. B., Thomas, E., et al., *Init. Repts. DSDP*, 94, Pt. 2: Washington (U.S. Govt. Printing Office), 651–702.

Whelan, J. K., Tarafa, M. E., and Hunt, J. M., 1982. Volatile C_1-C_8 organic compounds in macroalgae. *Nature*, 299:50–52.

Whitmarsh, R. B., 1979. The Owen Basin off the southeast margin of Arabia and the evolution of the Owen Fracture Zone. *Geophys. J. R. Astron. Soc.*, 58:441–470.

Wyrtki, K., 1971. *Oceanographic Atlas of the Indian Ocean Expedition:* Washington (National Science Foundation).

Ms 117A-110

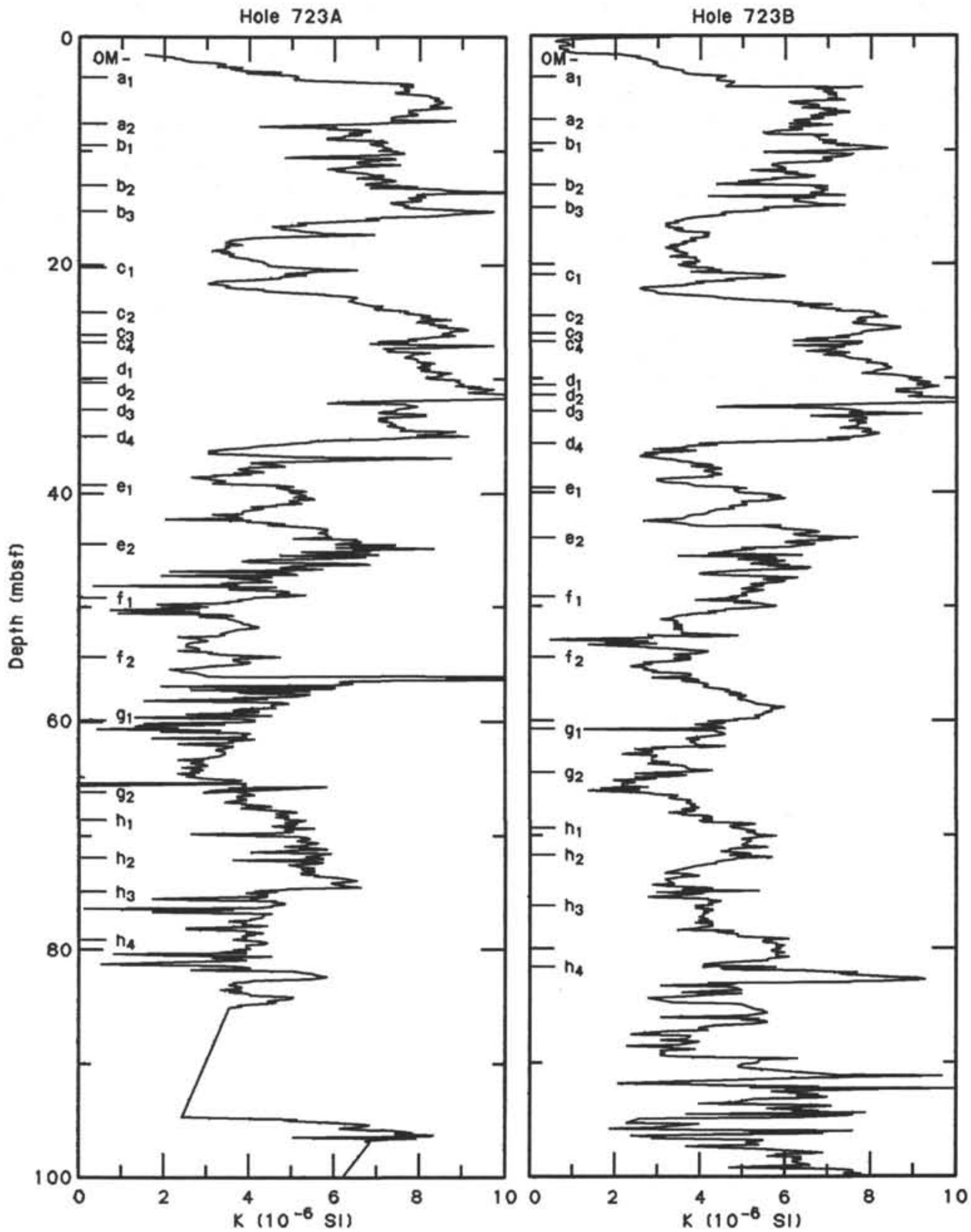

Figure 52. Magnetic susceptibility and positions of marker layers at Holes 723A and 723B.

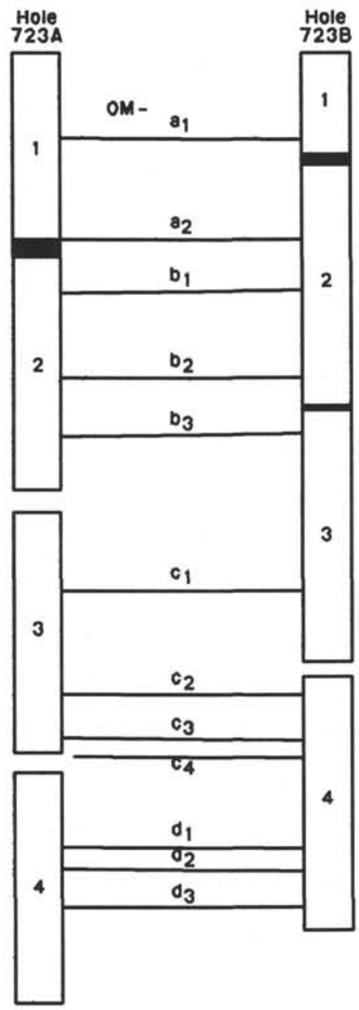

Figure 53. Correlation of Holes 723A and 723B based on marker layers.

Table 16. Stratigraphic depths and descriptions of the marker layers at Site 723 for layer-by-layer correlation in the Oman margin.

	Hole 723A		Hole 723B			
Layer	Core, sample, interval (cm)	Depth (mbsf)	Core, sample, interval (cm)	Depth (mbsf)	Holes 723B − 723A	Remarks[a]
OM-a_1	1H-3, 20	3.20	1H-3, 35	3.35	0.15	top of white later (10)
a_2	1H-5, 125	7.25	2H-3, 20	7.50	0.25	base of dark layer (10 horizontal)
b_1	2H-2, 55	9.85	2H-4, 65	9.45	−0.40	central band of 3 very black bands (30)
b_2	2H-4, 90	13.20	2H-6, 110	12.90	−0.30	base of dark band in dark layer overlying light layer
b_3	2H-6, 10	15.40	3H-1, 95	14.95	−0.45	very black layer in dark zone (5–10 semi-horizontal)
c_1	3H-3, 10	20.60	3H-5, 110	21.10	0.50	very black layer (20 horizontal mottled)
c_2	3H-5, 110	24.60	4H-1, 85	24.45	−0.15	dark layer in basal part of white layer; top of centimeter-scale lamination
c_3	3H-6, 130	26.30	4H-2, 100	26.10	−0.20	laminated top light band in dark interval
c_4	3H-7, 45	26.95	4H-3, 15	26.75	−0.20	dark band overlying light layer
c_5	—	—	4H-3, 100	27.60	—	lower dark thin band (50 mm) of 3 bands in light layer (present in Hole 723B only; upper band noted as OM-c_4)
d_1	4H-2, 135	29.95	4H-5, 70	30.30	0.35	dark band overlying light layer (20–30)
d_2	4H-3, 70	30.80	4H-6, 10	31.20	0.40	dark layer overlying light layer with sharp contact
d_3	4H-4, 65	32.25	4H-7, 5	32.65	0.40	basal boundary of dark layer (10 semihorizontal)
d_4	4H-6, 45	35.05	5H-2, 50	35.30	0.25	very black band in middle part of dark layer
e_1	5H-2, 90	39.20	5H-5, 20	39.50	0.30	white layer overlain by dark layer (10)
e_2	5H-6, 35	44.65	6H-1, 90	43.80	−0.85	dark band in lower part of light layer (20 vertical)
e_3	—	—	6H-3, 150	47.40	—	dark band in dark layer overlying on light layer (present in Hole 723B only)
f_1	6H-2, 115	49.05	6H-5, 120	50.10	1.05	dark band in dark layer (20–30 vertical)
f_2	6H-6, 70	54.60	7H-2, 15	54.25	−0.35	base of black layer overlying light interval (horizontal 10)
g_1	7H-3, 75	59.85	7H-6, 30	60.40	0.55	dark band in dark layer
g_2	7H-8, 5	66.65	8H-2, 60	64.40	−2.25	center of black layer (20–30 vertical)
h_1	8H-2, 80	68.10	8H-5, 90	69.20	1.10	top of white layer (20 semivertical)
h_2	8H-5, 30	72.10	9H-1, 20	72.10	0	base of dark band in light interval
h_3	8H-6, 140	74.70	9H-3, 135	76.25	1.55	boundary between dark layer and light layer (30 vertical)
h_4	9H-3, 35	78.75	9H-7, 95	81.85	3.10	light band in dark layer

[a] Description of bioturbation and size of layer (in mm) appear in parentheses.

Table 17. Correlated sub-bottom depth of core-top for stratigraphic sub-bottom depth calculation.

	Hole 723A				Hole 723B		
Core	ODP top depth (mbsf)	Difference	Corrected top depth (mbsf)	Core	ODP top depth (mbsf)	Difference	Corrected top depth (mbsf)
1H	0	0	0	1H	0	0	0
2H	7.8	−0.6	7.2	2H	4.3	−0.3	4.0
3H	17.5	0.9	17.8	3H	14.0	0.1	13.8
4H	27.1	0.5	27.9	4H	23.6	0.7	24.1

Note: ODP top depth = sub-bottom depth of core top calculated by the ODP CORELOG data; Difference = the difference between the depth calculated by the ODP CORELOG data and the depth calculated by the layer-by-layer correlation method; Corrected top depth = sub-bottom depth of core top calculated by the layer-by-layer correlation method.

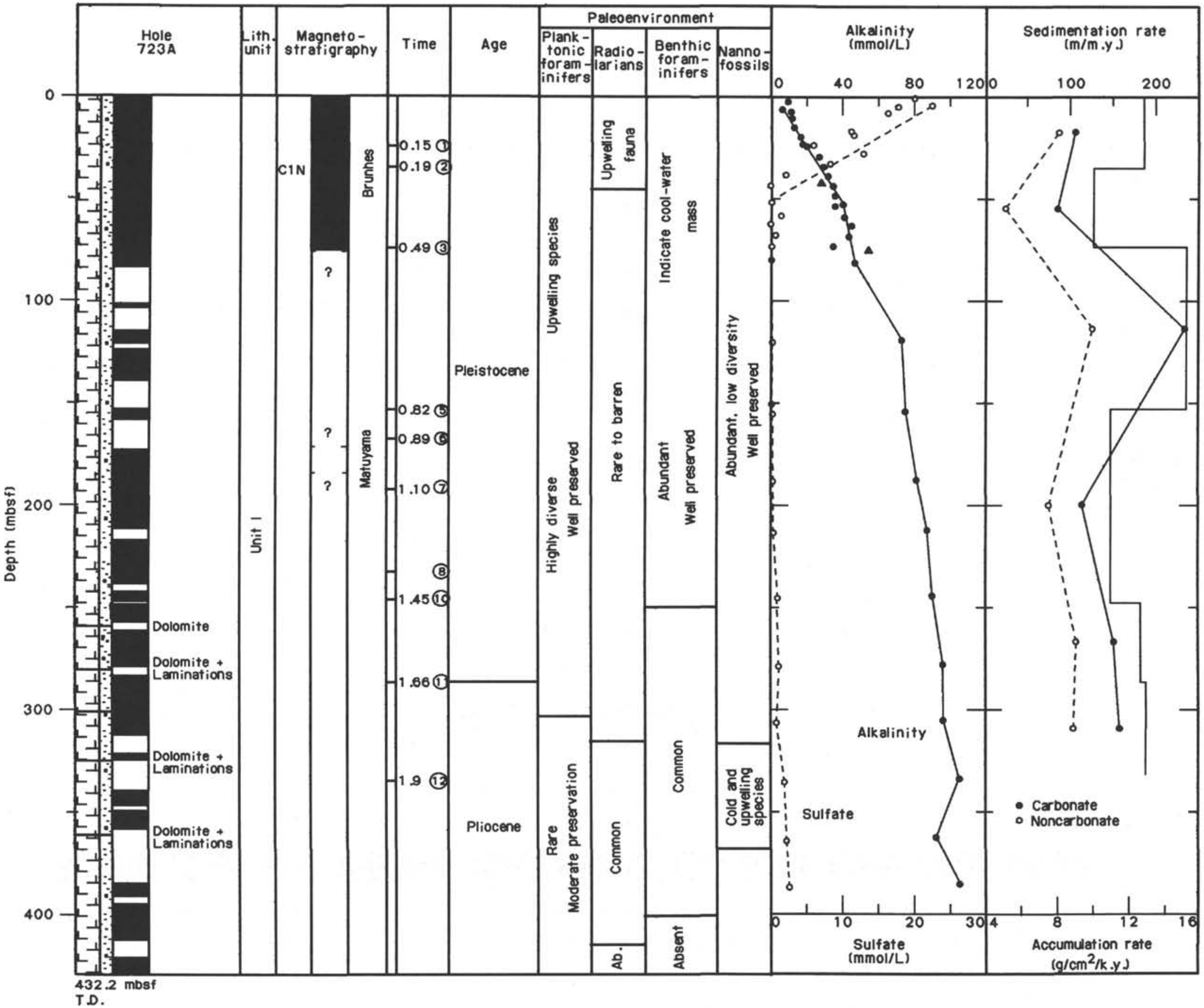

Figure 54. Summary chart outlining preliminary shipboard findings at Site 723. Numbers in circles under "Time" correspond to nannofossil datum levels (see "Biostratigraphy" section, this volume).

Summary Log for Hole 723B

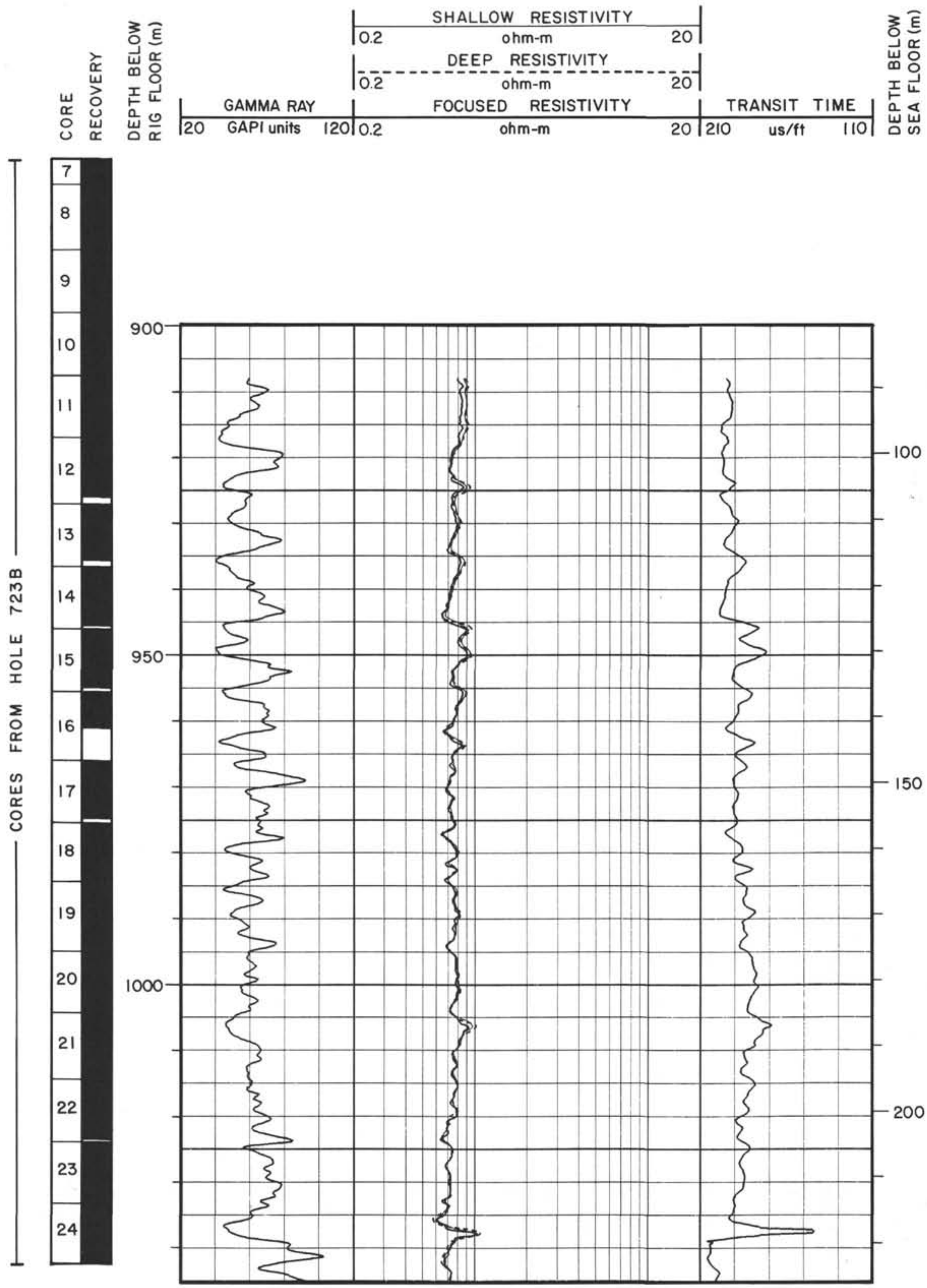

Summary Log for Hole 723B (continued)

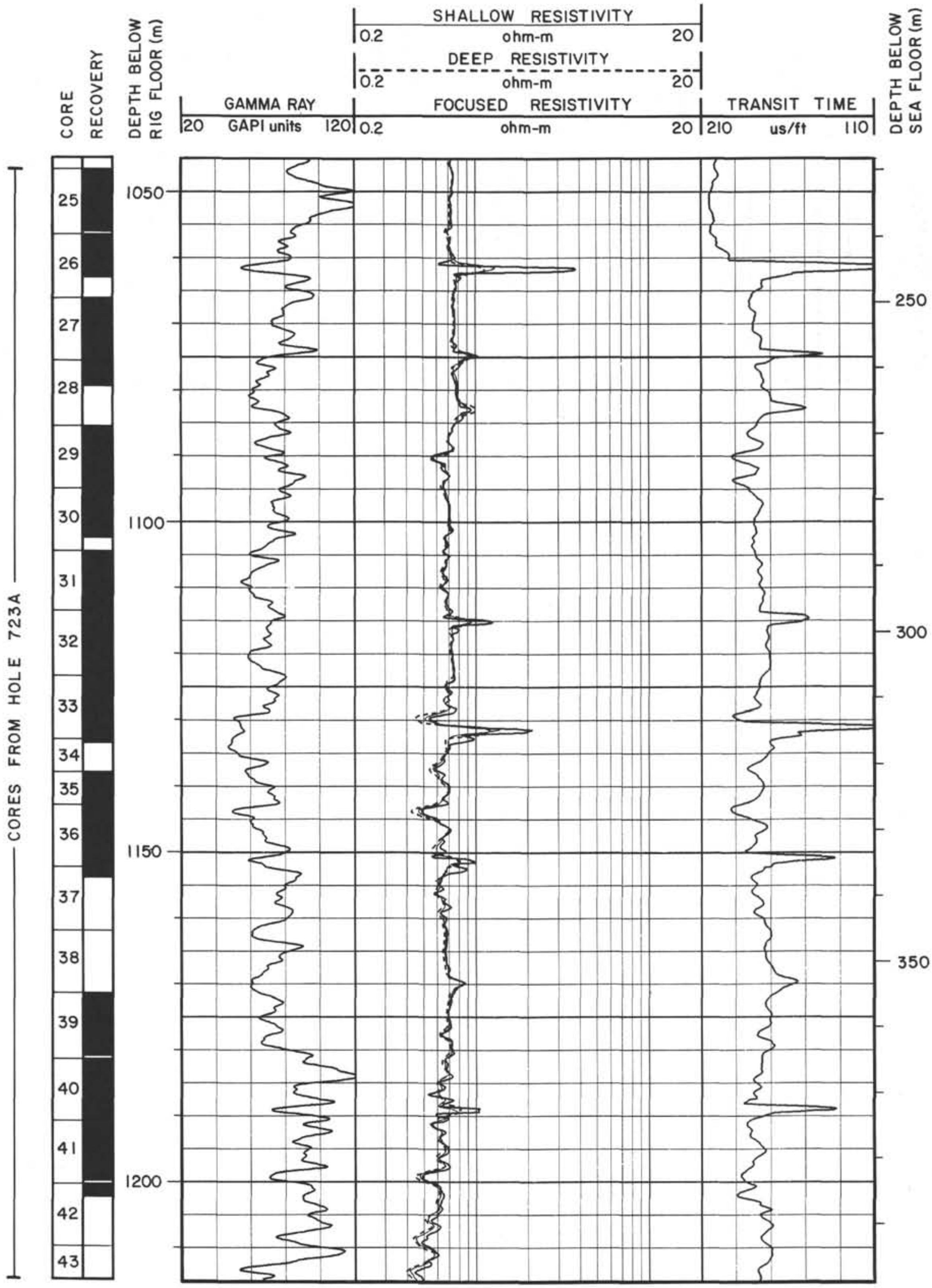

Summary Log for Hole 723B (continued)

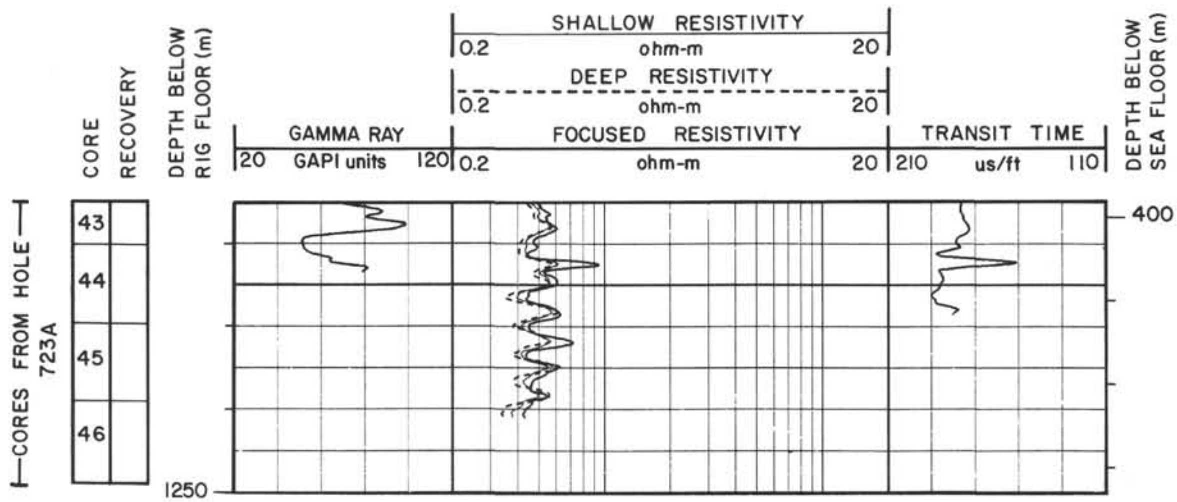

Summary Log for Hole 723B (continued)

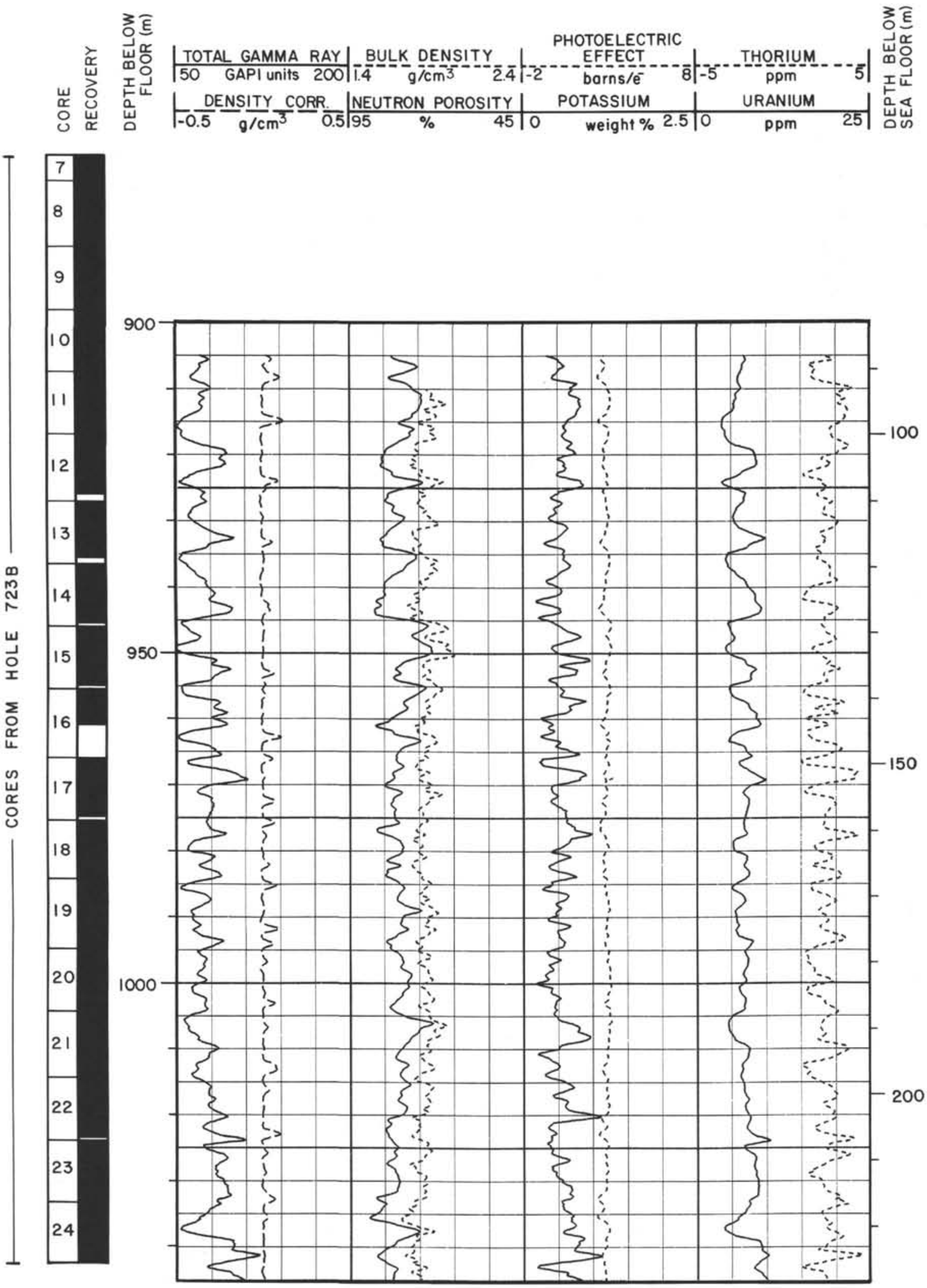

Summary Log for Hole 723B (continued)

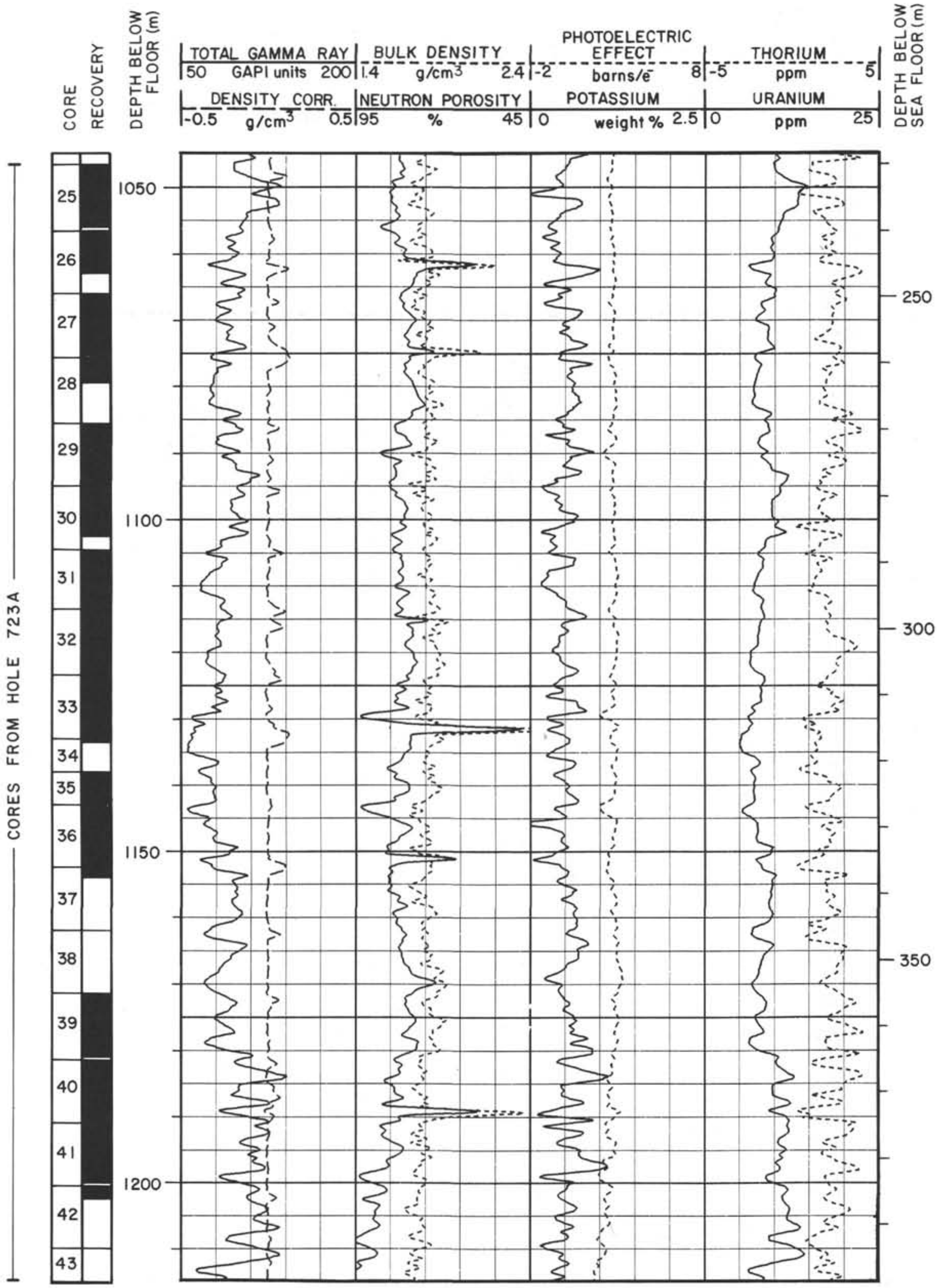

Summary Log for Hole 723B (continued)

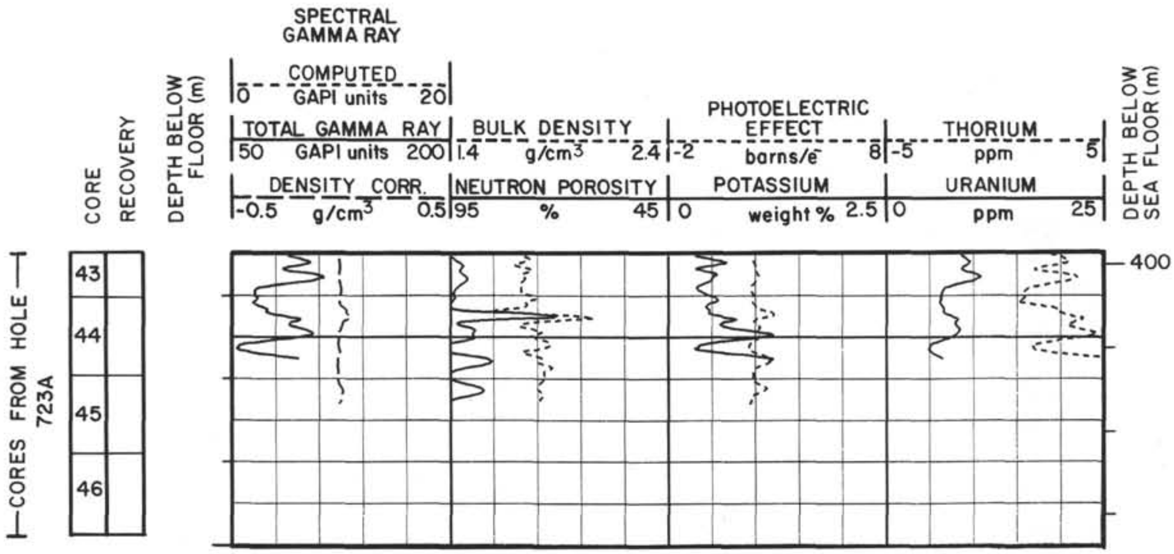

Summary Log for Hole 723B (continued)

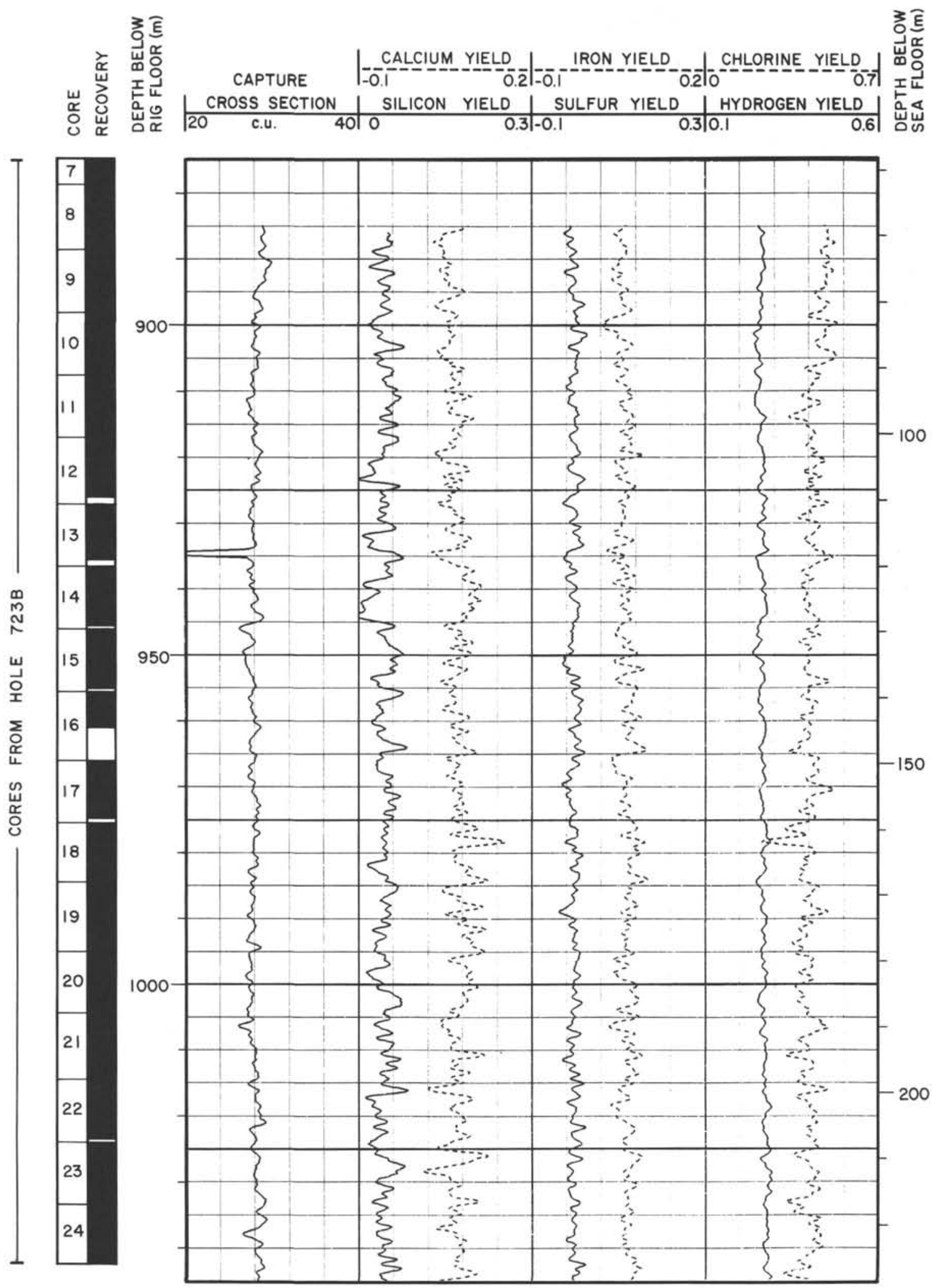

Summary Log for Hole 723B (continued)

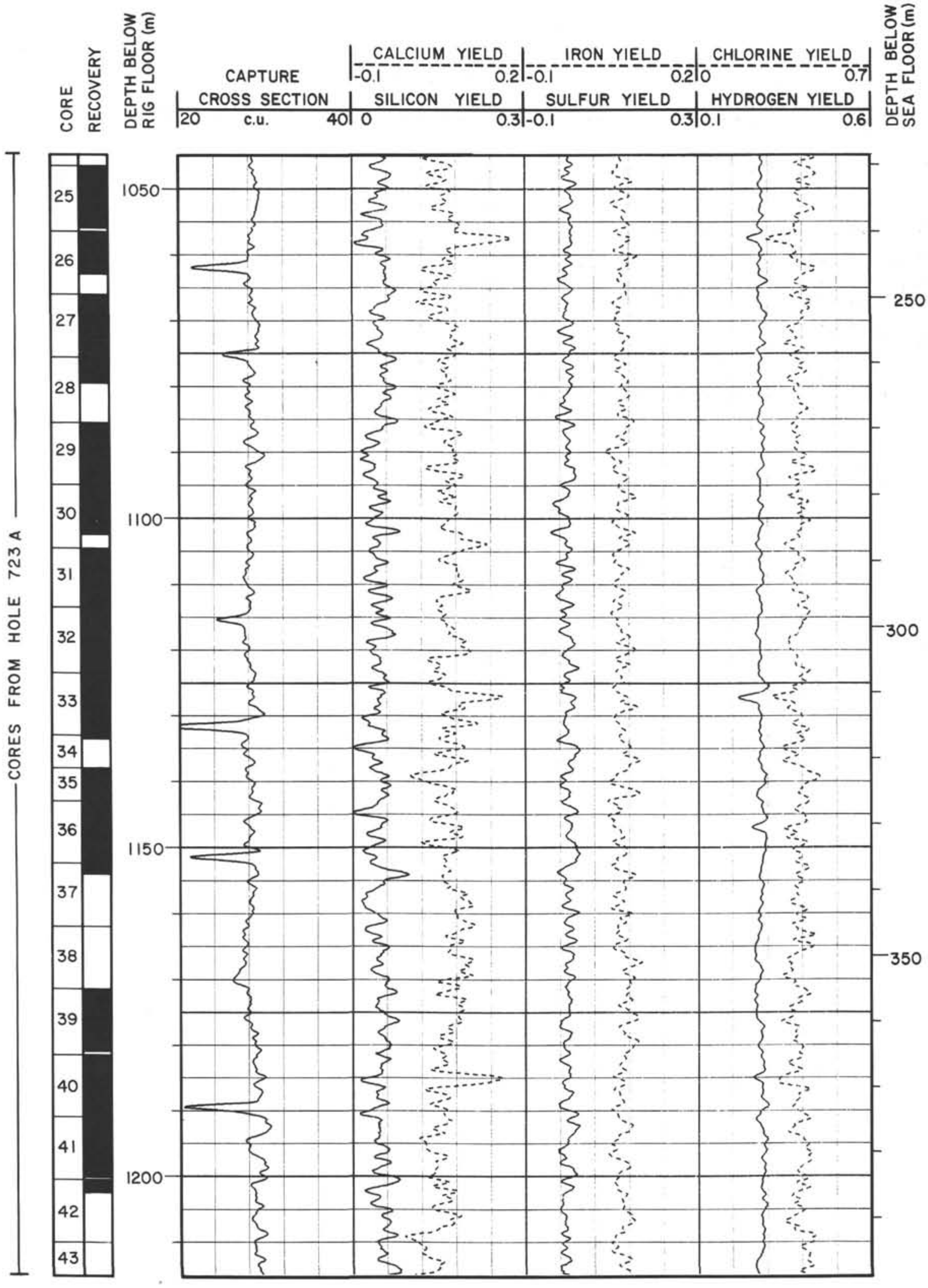

Summary Log for Hole 723B (continued)